Towards a novel platform for imaging molecules in an optical lattice

ANDREW DAVID INNES

How to cite:

INNES, ANDREW DAVID (2023) Towards a novel platform for imaging molecules in an optical lattice. Doctoral thesis, Durham University.

Towards a novel platform for imaging molecules in an optical lattice

Andrew David Innes

Abstract

This thesis reports on the development of a new apparatus which will be used to produce rovibrational ground state molecules with the goal of imaging them in an optical lattice. These types of experiments are often referred to as quantum gas microscopes.

The two molecules which we wish to study are RbCs and KCs. RbCs has been already studied substantially at Durham but not in an apparatus as advanced as the one discussed in this thesis. RbCs and other ground state diatomic molecules may be formed in the rovibrational ground state by using a magnetoassociation on an interspecies Feshbach resonance followed by stimulated Raman adiabatic passage (STIRAP). In our new apparatus we plan to repeat this in an optical lattice positioned directly above an objective with a high numerical aperture which will have the capability to resolve single lattice sites. Loading molecules into an optical lattice will allow access to dipolar physics associated with the intrinsic electric dipole moment of the molecule. This will grant us the capability to perform experiments, such as quantum simulation, that can yield a deeper understanding of the quantum nature of matter confined in lattices. In addition we show work towards KCs molecules, of which ground state molecules are yet to be formed. This molecule has a dipole moment of 1.92 D and a stable fermionic isotope which makes it a promising candidate for our studies in addition to RbCs.

A new vacuum chamber apparatus is constructed. A pair of 2-dimensional magneto-optical traps (2D-MOTs), one for Cs and the other for K/Rb, provides a flux of atoms to the centre of our main vacuum chamber. Here the atoms are collected in a 3D-MOT. The 3D-MOT can accumulate 10^8 Cs atoms, 10^9 Rb atoms and 10^8 K atoms. The laser setups for our MOTs are also presented in this thesis. We laser cool Rb, Cs and K on their respective

D_2 transitions. There is a particular focus on the optimisation process of K. We have managed to cool a sample of 10^8 K atoms to 42(2) µK and obtain a simultaneous MOT of both K and Cs. We have potential plans to further cool K on the D_1 line. To achieve this we need some means of high quality frequency stabilisation so a study on the modulation transfer spectroscopy of K and a comparison against the associated theory is also presented in this thesis.

Using a moving optical standing wave the atoms are transported to the science cell. They will subsequently undergo various cooling stages until the phase space density is sufficiently high for magnetoassociation. This has been achieved with Rb and Cs but not yet for K and Cs. They will then be loaded into an optical lattice and associated into molecules.

STIRAP requires lasers frequency stabilised to less than a kHz. The STIRAP setup is also described in detail in this thesis. We lock two lasers of wavelength 895 nm and 1359 nm to an ultra low expansion cavity and demonstrate proof of concept of how such a setup can serve the dual purpose of both STIRAP for KCs molecules and for exciting Cs atoms to Rydberg states using the Cs D_1 transition.

Towards a novel platform for imaging molecules in an optical lattice

Andrew David Innes

A thesis submitted in partial fulfilment
of the requirements for the degree of
Doctor of Philosophy

Department of Physics
Durham University

November 2023

Contents

List of Figures

Figure Page

List of Tables

Acknowledgements

Undoubtedly, this PhD project has been the most difficult challenge of my life thus far and there are a fair number of people to whom I owe thanks for the help along the way.

Firstly, I would like to thank my supervisor Prof. Simon Cornish. Simon has an incredibly keen eye for detail and can always seem to come up with solutions to even the most technically challenging problems.

This work would not have been possible if it were not for the immense effort and contribution from the postdocs. Sarah Bromley, who has shown amazing commitment to the project and put up with a lot of annoying questions from myself, Philip Gregory, who aided us with his expertise in molecules, Lewis McArd, who knew everything there was to know about vacuum chambers and electronics, and Alex Alampounti, who would occasionally stay in the lab with me to near midnight aiding me with the frustrating process of aligning the potassium cooling lasers.

I would also like to thank my fellow PhD lab mates. Namely Mew, Jonathan, Alex and Adarsh. They always kept the lab alive with their conversation and interesting choices in lab music. At this point it would be criminal not to acknowledge Adarsh's rather unconventional sense of humour. Thanks also to Stefan and Dan. Stefan joined the Cornish group at the same time as myself but worked on the tweezer project. He was always willing to offer a helping hand when needed both in the lab and outside. Dan provided a lot of support in getting the STIRAP lasers locked to the cavity.

I have to acknowledge the wider support of the members of QLM. They have all been excellent in providing a welcoming community and there would often be a good showing at the Friday seminars to wind down the week.

Finally, I would like to show my gratitude to my family who have all shown incredible support through the course of this project. In particular: my sister, Danielle, my gran, Greta, my mum, Lorraine and my dad, David. I would not have been able to get through this without them.

Declaration

I confirm that no part of the material offered has previously been submitted by myself for a degree in this or any other University. Where material has been generated through joint work, the work of others has been indicated.

Andrew David Innes

Durham, November 2023

Chapter 1

Introduction

1.1 Background

The field of atomic, molecular and optical physics has came a long way since Rutherford discovered the nuclear nature of atoms in 1909. One could argue the modern incarnation of atomic, molecular and optical (AMO) physics probably started around 1975 with the discovery of laser cooling of the atom [1].

Since this hallmark discovery, the ability to use optics and lasers to cool atoms to sub-microkelvin temperatures [2, 3], trap the atom [4–6] and exercise precise control of the quantum behaviour of the atom has proven pivotal at furthering our understanding of atomic physics. Several such crucial breakthroughs include the realisation of quantum degenerate gasses [7–10], trapping of atoms in optical lattices for simulation of many body systems [11–13] and the advent of ultracold rovibrational ground state molecules [14].

In 2009 Bakr *et al.* [13] published work on a new invention in the field: a quantum gas microscope. This device is an experimental tool for directly imaging fluorescence from a quantum degenerate gas loaded into an optical lattice with single site and single atom resolution. It has proven to be a promising tool for future explorations of quantum simulation [15, 16]. This thesis reports progress towards the construction of a quantum gas microscope with capability of imaging both KCs and RbCs molecules.

1.2 Molecules

1.2.1 Why Molecules

As mentioned, a powerful motivation for loading particles into an optical lattice and imaging them is for quantum simulation. For instance, ^{87}Rb atoms in an optical lattice would normally behave in accordance with the Bose-Hubbard model. Likewise, ^{40}K atoms would obey the Fermi-Hubbard model. Being able to create and probe customisable lattices will greatly reinforce our understanding of analogous solid state systems which are also subject to the Hubbard model or even related models such as the Heisenberg model [17–20].

Neutral atoms, whilst good at tunnelling between sites, are quite poor at interacting with each other between sites, owing to lack of any long range interactions. This means that long range interaction terms in an XXZ Hamiltonian for an optical lattice loaded with neutral atoms are effectively zero and therefore do not offer a complete picture of what might be a solid-state simulated lattice [14].

A particle with an intrinsic dipole moment can circumvent this issue as it can offer a long range interaction, via an electric or magnetic field allowing the atoms to talk to each other between sites. An example of such particles are neutral atoms with a strong magnetic moment such as Cr [21, 22], Er and Dy [23, 24] which have magnetic dipole moments of 6 µ, 7 µ and 10 µ Bohr magnetons respectively. Magnetic atoms have the advantage of longevity but are disadvantaged in that the long range interaction strength is typically weaker than that usually achieved for other particle types.

Another alternative is Rydberg atoms [25]. These are at the opposite extreme from magnetic atoms in that they have typically very large electric dipole moments, sometimes on the order of 1000 Debye. They do however suffer from very short lifetimes. With that in mind, Rydberg atoms do still have sufficiently long enough lifetimes to perform quantum simulation experiments in the microscope but longer lifetimes can allow us to study the systems evolution over a greater period.

Polar molecules offer an interesting middle ground between these two extremes. Molecules give us greater lifetimes than Rydberg atoms with larger dipole moments than magnetic atoms: roughly on the order of 0.5 Debye to 5 Debye. For reference, the electric dipole moment is of the order of 10^4 greater than the magnetic dipole moment [26].

Finally, another advantage of molecules is the easily controllable energy level structure. Dimers typically have one rotational and vibrational degree of freedom. When near the ground state of the molecule the energy levels associated with the vibrational degrees of freedom will typically follow the rules of a well behaved harmonic oscillator whereas the rotational levels will be anharmonic.

1.2.2 Forming Rovibrational Ground State Molecules

The creation of an ultracold sample of ground state molecules are broadly divided into two methods: the direct method and the indirect method. Briefly, the direct method starts with a vapour of the molecule already formed. The molecule is trapped with a ‘molecular MOT’ and subsequently laser cooled with sub-Doppler forces originating from photons near resonance with transitions in the molecular structure. Molecules used in direct cooling are CaF [27], SrF [28] and YO [29].

The method that will be applied in our experiment is the indirect method. For a diatomic molecule both atomic species are initially cooled to a high phase-space density and then associated, either by magnetoassociation (on a Feshbach resonance) or photoassociation. Molecules that have undergone magnetoassociation typically lie on a weakly bound state and are subsequently transferred to the rovibrational ground state with stimulated Raman adiabatic passage [14]. Bialkali ground state polar molecules formed with this method include RbCs [30–32], KRb [14], NaCs [33], NaRb [34], NaK [35] and LiCs [36].

1.2.3 RbCs

The experiment has initially been designed for the RbCs molecule. It seemed the most obvious choice since the vast majority of research with polar molecules in our group has been done with RbCs molecules. This means we already have a considerable amount of experience to fall back on and the work associated with optimising the molecule formation process (magnetoassociation fields and STIRAP frequencies) has already been done. In addition, the individual laser cooling of Rb and Cs is generally more straightforward in comparison with other species.

RbCs has an intrinsic dipole moment of 1.26 D [32]. The splitting between the rotational energy levels near the rovibrational ground state, the rovibrational constant, is $B_0 = 0.49$ GHz [37]. It is chemically stable so that the reaction that would cause RbCs to decay into a pair of bialkali mononuclear dimers is endothermic [38].

A major disadvantage of RbCs is that the formation of these molecules requires utilising Feshbach resonances in magnetic fields where Rb and Cs are not miscible due to their scattering properties in the BEC phase. As such, RbCs Feshbach molecules can only be formed in the thermal state where the phase space density is reduced, limiting the efficiency of RbCs molecule formation [38, 39].

1.2.4 KCs

At the time of writing KCs rovibrational ground state molecules have yet to be realised, however there are some advantages to pursuing KCs in addition to RbCs. The KCs molecule has a predicted intrinsic dipole moment of 1.91 D [40] meaning that its interaction strengths are greater than that of RbCs. Additionally, it has a rotational constant of $B_0 = 0.93$ GHz [41].

Further, K has three stable isotopes, namely: ^{39}K, ^{40}K and ^{41}K. An apparatus with the capability to exploit the ^{40}K isotope will also allow access to fermionic molecules as well as bosonic.

For ^{41}KCs there are predicted to exist regions in its Zeeman landscape where Feshbach resonances are accessible in the miscible BEC phase [42] allowing for association at even greater phase-space densities than RbCs. Like RbCs it is also chemically stable.

1.3 Quantum Gas Microscopes

1.3.1 Optical Lattices

When three perpendicular standing wave beams are overlapped they create a 3D optical lattice in the region of overlap. If the beams are perpendicular the interference creates a periodic standing wave electric field in all three directions of propagation. The optical dipole force will attract particles subject to the force to either the nodal or anti-nodal points of this field (depending on whether the polarisability is negative or positive at the dipole laser wavelength) [43, 44].

This configuration can be modelled by a periodic potential similar to that shown in Fig. 1.1. Atoms are drawn to the potential minima where, at sufficiently low temperatures, they will act as if in a harmonic trap. The intensity of the beams can be used to tune the lattice depth which in turn adjusts the rate of tunnelling. For BECs this can lead to some interesting effects such as a phase transition from a superfluid to a Mott insulator [45–47].

Typical dipole traps are used at 1064 nm which is far red detuned from the D_2 transitions of the alkali atoms. This in turn gives us a nearest neighbour lattice spacing of 532 nm for a cubic lattice. As mentioned, unless we have a particle which exhibits a strong long range dipole-dipole interaction, then we will not realise the full Hamiltonian necessary for simulating real metallic lattices.

1.3.2 Imaging Atoms in an Optical Lattice

The quantum gas microscope was first realised by the Greiner group in 2009 for Rb [13]. Since then, many quantum gas microscopes have been constructed for various atomic species including ^{174}Yb [48, 49], ^{6}Li [50, 51], ^{7}Li [52], ^{40}K [53, 54] and Cs[55]. More recently a microscope has been demonstrated for ^{23}Na^{87}Rb Feshbach and ground state molecules [56].

At the heart of a quantum gas microscope are two components. The loaded optical lattice and a high numerical aperture (NA) objective. The high NA

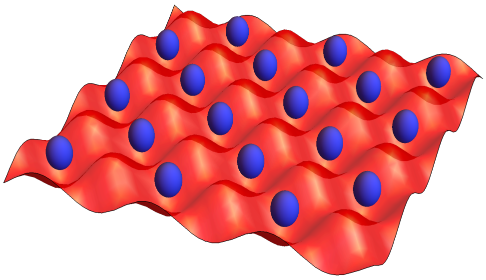

Figure 1.1: Sketch illustrating atoms in an optical lattice potential. The red surface is the lattice potential and the blue spheres represent particles which are drawn to the minima of the potential by the optical dipole force.

value was initially achieved by bringing a large radius, short focal length lens close to the lattice but more complex designs with multiple lenses have since been constructed.

When the atoms are loaded, imaging is performed by shining cooling light in a molasses configuration onto the lattice. The molasses light, being near resonance, will act to cool the atoms and prevent excitation in their lattice site. In addition the atoms will scatter the molasses light, causing fluorescence. Photons collected by the objective are gathered and imaged on a CCD camera to reveal the single site resolution of the lattice.

Sites with no atoms will be dark whereas sites with one atom will appear to fluoresce. For multiple atoms, light assisted collisions will remove pairs of atoms. If there is an even number atoms on the site then all atoms are paired and removed from the site leaving no atoms to fluoresce, hence giving a dark site. If there is an odd number of atoms then there will be one unpaired atom which will remain in the lattice and allow that particular site to fluoresce. Ideally, a rate of one atom per site would therefore be optimal. This can be achieved by centering the superfluid sample on the optical lattice and ramping up the trap depth to turn this sample into a Mott insulator [57]. The density of the superfluid would determine the number of atoms per site.

1.3.3 Molecular Quantum Gas Microscopes

Optical lattices with molecules have been achieved [31, 58]. In the case of a molecular quantum gas microscope, some additional capabilities are required to an atomic quantum gas microscope.

For one, we wish to exploit the long range dipole-dipole interactions of the molecule so we need some electrodes near the lattice to produce an electric field. However, glass is dielectric and therefore nearby glass must be kept at a distance of a few cm away from the lattice to avoid deforming the electric field. This includes optics associated with the viewport (the cell) and the objective.

The molecule is broken into its constituent atoms and the atoms can be imaged directly. This requires reversing the STIRAP and Feshbach resonance processes and in fact plays to our advantage. Any quantum simulation experiment that happens between loading the lattice and imaging means the molecules will not be in the initially prepared ground state but often distributed amongst two states. Imaging after dissociation offers a mechanism to extract the rotational level of the molecule since the STIRAP beams will only interact with molecules in their rovibrational ground state [59]. So, the ground state molecules may be imaged first. The remaining molecules can then be transferred to the ground state and imaged second. A laser at a different wavelength to the lattice may be needed to create an additional force to separate the Rb from the Cs atoms to prevent atoms being immediately lost due to light assisted collisions. Bi-alkali molecules can still be detected with fluorescence imaging but it is also quite difficult to image bi-alkali molecules directly in a microscope due to the lack of cycling transitions so using this splitting method also gives us a more efficient means of probing the final state and imaging the molecules, indirectly at least.

1.4 Thesis Outline

This thesis is outlined as follows.

In chapter 2 a review of the relevant physics is given. This will incorporate a section on the rigid rotor model of dimer molecules, a section on the XXZ model and the conditions it imposes on our electric fields and finally a look at our electrode system and possible upgrades for our electrodes in the future.

In chapter 3 we outline the newly constructed vacuum apparatus for this experiment. Our vacuum chamber is comprised of four main parts: Rb/K 2D-MOT, Cs 2D-MOT, the main chamber and the science cell. We discuss the 2D-MOTs and the main chamber in detail and the science cell in summary.

In chapter 4 we summarise our work on spectroscopy of K, specifically modulation transfer spectroscopy on the D_1 lines of K. We compare the results obtained from an MTS signal predicted from theory to a signal obtained from experiment. The study is carried out for four different polarisation configurations and we discuss the results and how well the experiment agrees with theory.

In chapter 5 we will review the optimisation of the MOT and Doppler cooling processes for ^{41}K. In our new vacuum chamber we manage to cool a sample of ^{41}K to 48 µK with an atom number of 10^8. We also do a brief study on polarising our sample of K for a magnetic trap.

In chapter 6 we offer a brief summary of the cooling systems for our other species, Rb and Cs, and demonstrate a three species MOT.

In chapter 7 we summarise the frequency stabilisation of the STIRAP lasers and also give an overview for some spectroscopy experiments carried out on Cs which will be useful should we wish to pursue Cs Rydberg atoms in the future.

In chapter 8 we offer a conclusion and outlook for the experiment.

1.5 List of Publications

The contents of chapter 4, as well as additional material summarising the theory of the study in chapter 4, are covered in parts of a paper which is in a pre-print stage:

[60] A. D. Innes, P. Majumder, H. R. Noh, and S. L. Cornish, arXiv preprint arXiv:2310.11327 (2023).

Further papers related to this work include:

[61] A. J. Matthies, J. M. Mortlock, L. A. McArd, A. P. Raghuram, A. D. Innes, P. D. Gregory, S. L. Bromley, and S. L. Cornish, arXiv preprint arXiv:2307.13382 (2023)

and

[62] A. Ratkata, P. D. Gregory, A. D. Innes, A. J. Matthies, L. A. McArd, J. M. Mortlock, M. S. Safronova, S. L. Bromley, and S. L. Cornish, Phys. Rev. A 104, 052813 (2021).

Chapter 2

Interacting Molecules in an Electric Field

2.1 Introduction

In this chapter we will address the theoretical motivations for studying molecules in an optical lattice. At the heart of the discussion are the long range interactions present within the lattice and how such a system's behaviour depends on an electric field. Broadly speaking this chapter will be divided into four main sections. In section 2.2 we will look at the rigid rotor model for a diatomic molecule in a DC electric field which will give us a basic insight into the quantum structure of a diatomic molecule and how it interacts with external fields. This model does not include the molecule's hyperfine structure but it is sufficient for our purposes. In section 2.3 we will look at how the molecules interact with each other in a lattice giving way to the XXZ model. In section 2.4 we will seek to model the behaviour of interacting molecules in our lattice with the addition of an external field. The will give us some of the requirements our apparatus must satisfy for experiments of this nature to be successful. Finally, in section 2.5 we will discuss some electric geometries, both the one used in our experiment and a proposed upgrade.

2.2 Rigid Rotor Model

2.2.1 The Molecular Hamiltonian

The Hamiltonian for the a diatomic molecule can consist of various terms.

$$H = H_{\mathrm{rot}} + H_{\nu} + H_{\mathrm{ext}} + H_{\mathrm{elec}} : \tag{2.1}$$

H_{rot} accounts for the rotational energy of the Hamiltonian, H_{ν} is a term regarding the vibrational motion of the molecule, H_{ext} is the part of the Hamiltonian which describes the molecule's interaction with an external electric field and finally H_{elec} describes the interaction of the electrons with each other and the nuclei.

The wavefunction describing the system in an external field can be split into a nuclear part $\psi(R)$ (with R being the internuclear separation) and an electronic part $\phi(\boldsymbol{r}, R)$ where $\boldsymbol{r}$ is a vector describing the position of the electrons. Consequently, the Schrodinger equation of the system is:

$$H\Psi(\boldsymbol{r}, R) = E_i\Psi(\boldsymbol{r}, R), \tag{2.2}$$

with:

$$\Psi(\boldsymbol{r}, R) = \psi(R)\phi(\boldsymbol{r}, R), \tag{2.3}$$

and E_i is the eigenenergy of the ith state. Since the wavefunction is separable we can discuss the nuclear and electronic parts independently and for this chapter we will largely focus on the nuclear part. Broadly speaking, the nuclear part of the diatomic molecule wavefunction can be described by two quantum numbers: a vibrational number, ν which accounts for the oscillations in the internuclear separation and a rotational number N which accounts for the rotary motion of the nuclear pair.

2.2.2 Vibrational Quantum Number

Labelling our two nuclei as A and B, the vibrational part of the Hamiltonian can be written as:

$$H_\nu = -\frac{\hbar^2}{2m_A}\nabla_A^2 - \frac{\hbar^2}{2m_B}\nabla_B^2 + V_\nu(R), \tag{2.4}$$

where m_A and m_B are the masses of the two nuclei and V_ν is the internuclear potential, see [63] for more details. This Hamiltonian may be written in the centre of mass frame as:

$$H_\nu = \frac{-\hbar^2}{2\mu}\nabla^2 + V_\nu(R), \tag{2.5}$$

where μ is the reduced mass of the system:

$$\mu = \frac{m_A m_B}{m_A + m_B}. \tag{2.6}$$

If we consider vibrations only along only one dimension, the internuclear axis, then the Laplacian operator can be simplified such that it depends on R only:

$$\left(\frac{-\hbar^2}{2\mu}\frac{\partial^2}{\partial R^2} + V_\nu(R)\right)\psi_\nu(R) = E_\nu\psi_\nu(R). \tag{2.7}$$

The molecular potential has a minimum at some equilibrium point R_0. If we assume that vibrations are small around this point we can Taylor expand $V_\nu(R)$ around that point:

$$V_\nu(R) = V_\nu(R_0) + \frac{B_e}{2}(R - R_0)^2 + ..., \tag{2.8}$$

and if we neglect the higher order terms then we are left with the Hamiltonian of the quantum harmonic oscillator. We can therefore deduce that the vibrational energy levels are given by:

$$E_\nu = \hbar\sqrt{\frac{B_e}{\mu}}\left(\frac{1}{2} + \nu\right), \tag{2.9}$$

with ν being the quantum number associated with the vibrational level.

2.2.3 Rotational Quantum Number

For the purposes of our experiment we are more interested in the rotational quantum number than the vibrational quantum number. The rotational number provides a wealth of energy levels that are reachable from each other with the use of microwaves. The dipole transition element between two rotational states gives us a means to access the long range interactions [64]. Since the molecules are initially in the rovibrational ground state we can set $\nu = 0$ and discard the vibrational parts of the molecular Hamiltonian, leaving us with just the rotational part. This can be modelled as a simple rigid rotor. The rigid rotor has kinetic energy [65]:

$$T = \frac{1}{2I_x}(L_x^2 + L_y^2) + \frac{1}{2I_z}L_z^2 = \frac{1}{2I_x}L^2 + \left(\frac{1}{2I_z} - \frac{1}{2I_x}\right)L_z^2. \tag{2.10}$$

Here L_i is the rotational angular momentum and I_i is the moment of inertia along axis i. The internuclear axis is taken to be z.

In this work we only consider molecules in a Σ potential in which there is no contribution to the total angular momentum from the electrons. In these potentials $L_z = 0$. The moment of inertia along the x axis is given by: $I_x = \mu R^2$. We can define the rotational constant $B_0 = \frac{\hbar^2}{2I_x}$. There is no potential energy for rotation so the Hamiltonian for the rotational part is purely kinetic:

$$H_{\text{rot}} = \frac{B_0}{\hbar}L^2. \tag{2.11}$$

For low lying energy levels, $N < 4$, the rotational eigenenergies are approximated by:

$$E_{\text{rot}} = B_0 N(N+1), \tag{2.12}$$

where N is the rotational quantum number. In spherical coordinates, the wavefunctions of this Hamiltonian are similar to the angular part of the hydrogen atom:

$$\psi_{\text{rot}}(\theta, \phi) = Y_{N,M_N} = C_L e^{-iM_N\phi} P_N^{M_N}(\cos\theta), \tag{2.13}$$

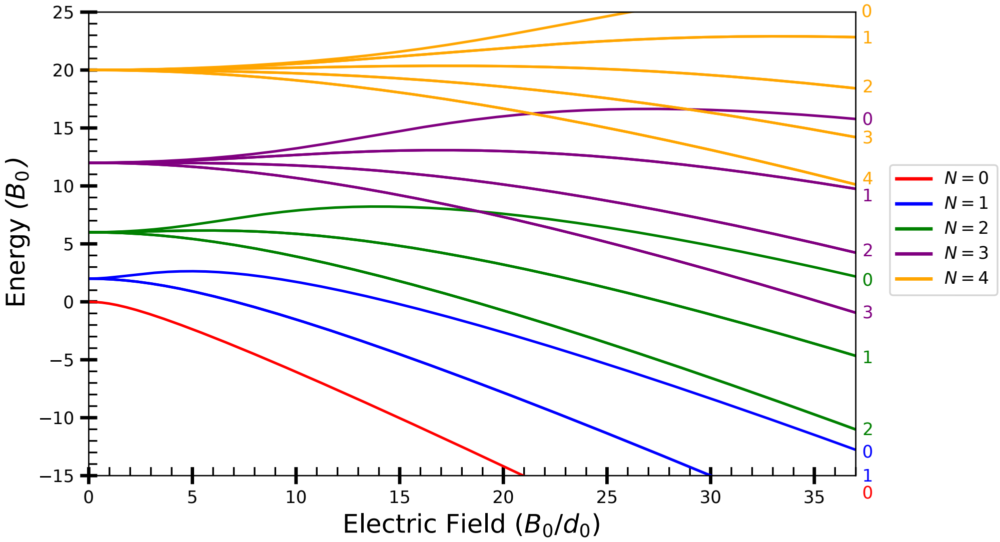

Figure 2.1: Calculated DC stark shift in rotational states of a diatomic molecule. The diagram shows the evolution of the eigenenergies in the rigid rotor model as a function of electric field. The colours correspond to different values of N, and each branch of N to different M_N. The M_n values are shown where that state crosses the vertical right axis, except for $|4, 0\rangle$, $|1, 1\rangle$ and $|0, 0\rangle$ which are indicated by the values at the top and bottom of the right axis. The units are in values of B_0 and d_0, constants unique to each molecule. As such the diagram is generalised to all bi-alkali molecules.

with C_L being the normalisation constant, $P_M^{M_N}$ the associated Legendre polynomial, θ the polar angle and ϕ the azimuthal angle. M_N is the projection of the rotational angular momentum onto the internuclear axis.

2.2.4 Behaviour in Electric Fields

The response of the rotational energy levels to the presence of an electric field can be understood by considering the external field term in the molecular Hamiltonian:

$$H_{\text{ext}} = H_{\text{DC}} = -\mathbf{E} \cdot \mathbf{d}. \tag{2.14}$$

$\mathbf{E}$ is the electric field vector and $\mathbf{d}$ is the molecule's dipole moment which is parallel to the direction of the internuclear axis.

At this particular juncture we require the transition dipole operator $\hat{d}_p$ whose matrix elements are given by:

$$\langle N, M_N | \hat{d}_p | N', M'_N \rangle = \\ d_0\sqrt{(2N+1)(2N'+1)}(-1)^{M_N} \begin{pmatrix} N & 1 & N' \\ -M_N & \Delta M_N & M'_N \end{pmatrix} \begin{pmatrix} N & 1 & N' \\ 0 & 0 & 0, \end{pmatrix} \tag{2.15}$$

where the terms in brackets are the Wigner-3j symbols and d_0 is the strength of the permanent dipole moment in the molecule's frame of reference [66]. For simplicity we will take the electric field to be along the fixed z axis, that is: parallel to the internuclear axis. In this situation we can reduce $\mathbf{E} \cdot \mathbf{d}$ to $E\hat{d}^z_p$ where E is the magnitude of the electric field and $\hat{d}_p = \hat{d}^z_p$ but with $M'_N = M_N$. The matrix elements in Eq. 2.14 then become:

$$\langle N, M_N | \mathbf{E} \cdot \mathbf{d} | N', M'_N \rangle = E \langle N, M_N | d^z_p | N', M'_N \rangle \\ = Ed_0\sqrt{(2N+1)(2N'+1)}(-1)^{M_N} \begin{pmatrix} N & 1 & N' \\ -M_N & 0 & M_N \end{pmatrix} \begin{pmatrix} N & 1 & N' \\ 0 & 0 & 0 \end{pmatrix}. \tag{2.16}$$

The full Hamiltonian of the molecule in the electric field is then the sum of the rotational and stark shift terms:

$$H = \sum_{N,M_N} \sum_{N',M'_N} B_0 N(N+1)\delta_{N,N'}\delta_{M_N,M'_N} \\ - Ed_0\sqrt{(2N+1)(2N'+1)}(-1)^{M_N} \begin{pmatrix} N & 1 & N' \\ -M_N & 0 & M_N \end{pmatrix} \begin{pmatrix} N & 1 & N' \\ 0 & 0 & 0 \end{pmatrix}. \tag{2.17}$$

Diagonalising this will yield the eigenenergies as a function of electric field. The stark map for $N = 0$ to $N = 5$ is shown in Fig. 2.1. The electric field mixes the eigenstates. We can write the wavefunctions of these modified eigenstates as a linear combination of the zero field rotational states:

$$\tilde{\psi}_{\tilde{N},M_N} = \sum_{N,M_N} c_{N,M_N}\psi_{N,M_N}, \tag{2.18}$$

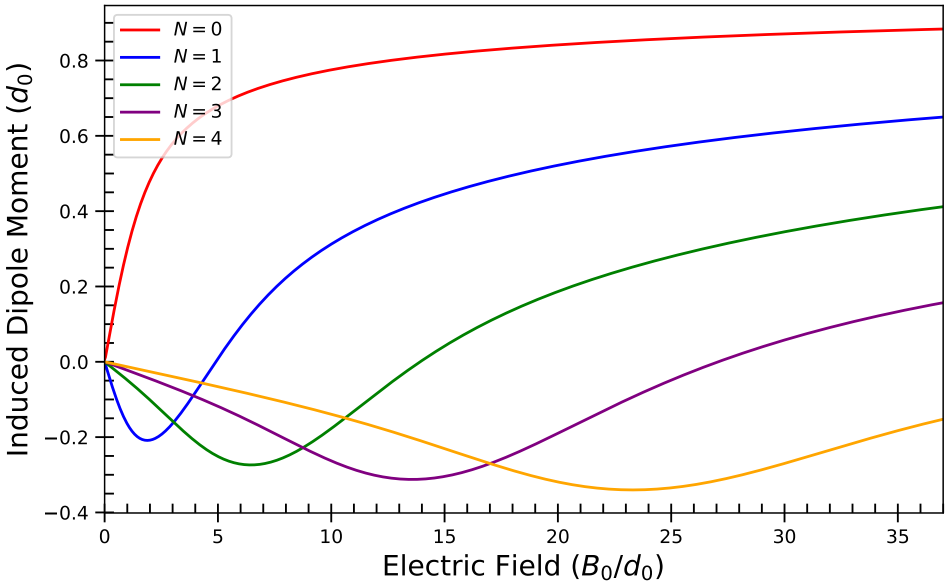

Figure 2.2: Laboratory frame electric dipole moments along z as a function of the external electric field magnitude for $M_N = 0, N = 0 - 4$. The graph shows the calculated induced dipole moments using Eq. 2.19. At low electric fields all except the $N = 0$ state have an inital dip followed by a sharp rise eventually tailing off at higher electric fields. The maximum induced dipole moment in the laboratory frame is just over 80% of the permanent dipole moment.

where c_{N,M_N} is the coefficient associated with the eigenergy ψ_{N,M_N} which are yielded by the eigenvectors of Eq. 2.17. The new quantum number $\tilde{N}$ is understood to be the quantum number associated with the state such that if the electric field is adiabatically ramped to zero will give the state associated with number N.

2.2.5 Induced Dipole Moments

We now have the tools necessary to calculate the induced dipole moments in the lab frame of reference. In the absence of an external field this dipole moment is zero in the lab frame of reference because of rotational symmetry. If we are concerned only with the induced dipole moment along the direction of the electric field (along the z axis) then it is possible to calculate for a state $\left|\tilde{N}, M_N\right\rangle$ simply with:

$$d_{z,\tilde{N},M_N} = \frac{d\epsilon_{\tilde{N},M_N}}{dE}, \tag{2.19}$$

where ϵ_i is the ith eigenenergy. These have been plotted in Fig. 2.2.

2.3 XXZ Model

2.3.1 Interacting Dipoles in an Optical Lattice

The principal reason for studying particles with a dipole moment is to exploit the long range dipole-dipole interaction and study how these particles interact with each other across the lattice. Several experiments have been proposed for interacting molecules in a lattice ranging from applications such as, but not limited to, spin exchange resonance [64] , quantum magnetism [17] and superfluid tunability [67]. One such experiment that our apparatus will allow us to realise will be the imaging of the propagation of states, pseudospins mapped to the molecule's rotational states, throughout an optical lattice via the dipole interaction [64, 68]. The derivation in this section can be found in [66].

2.3.2 Dipole-dipole Potential

Before we can understand these interactions however we must first establish the Hamiltonian which will describe the behaviour of our many-body system which will occupy the optical lattice. The potential of the dipole field between a pair of molecules is given classically by:

$$V_{ij} = \frac{1}{4\pi\varepsilon_0}\frac{\boldsymbol{\mu_i}\cdot\boldsymbol{\mu_j} - 3(\boldsymbol{\mu_i}\cdot\boldsymbol{r})(\boldsymbol{\mu_j}\cdot\boldsymbol{r})}{r_{ij}^3}, \tag{2.20}$$

where $\boldsymbol{\mu_i}$ is the classical dipole moment of the molecule on the ith lattice site, $\boldsymbol{r}$ is the position vector between the two molecules and r_{ij} is the distance between the two molecules [64]. We assume the two interacting molecules are pinned to sites on an optical lattice such that $\boldsymbol{r}$ is constant. For simplicity we will take the ith molecule to be sitting at the origin and the jth molecule at position $\boldsymbol{r} = (x, y, z)$.

The quantum form of 2.20 is:

$$V_{ij} = -\frac{\sqrt{6}}{r_{ij}^3} \sum_{q=-2}^{2} (-1)^q C_q^k(\theta, \phi) T_q^2(\mathbf{d}_i, \mathbf{d}_j), \tag{2.21}$$

where:

$$C_q^k = \sqrt{\frac{4\pi}{2k+1}} Y_{kq}(\theta, \phi), \tag{2.22}$$

and T is a tensor operator defined by:

$$T_{\pm 2}^2 = \hat{d_i^{\pm}} \hat{d_j^{\pm}}, \tag{2.23}$$

$$T_{\pm 1}^2 = \frac{\hat{d_i^0} \hat{d_j^{\pm}} + \hat{d_i^{\pm}} \hat{d_j^0}}{\sqrt{2}}, \tag{2.24}$$

and

$$T_0^2 = \frac{\hat{d_i^+} \hat{d_j^-} + \hat{d_i^-} \hat{d_j^+} + 2\hat{d_i^0} \hat{d_j^0}}{\sqrt{6}}, \tag{2.25}$$

where the operator $\hat{d_i^{\pm,0}}$ is the matrix element of the dipole operator as defined in Eq. 2.15 and the superscripts refer to the value of ΔM_N.

Here we will briefly outline how to obtain Eq. 2.21 from Eq. 2.20. We can treat the dipole operator as a ladder operator which allows us to map the operators onto spatial dipole operators:

$$\hat{d_i^{\pm}} = \frac{\hat{d_i^x} \pm i\hat{d_i^y}}{\sqrt{2}}, \tag{2.26}$$

$$\hat{d_i^0} = \hat{d_i^z}. \tag{2.27}$$

We only need $q = 0, \pm 1, \pm 2$ and so the associated expressions for C_q^2 are:

$$C_{\pm 2}^2 = \frac{\sqrt{6}}{4} \sin^2 \theta e^{\pm 2i\phi}, \tag{2.28}$$

$$C^2_{\pm 1} = \frac{\sqrt{6}}{2} \sin\theta \cos\theta e^{\pm i\phi}, \tag{2.29}$$

and

$$C^2_{\pm 0} = \frac{1}{2}\left(3\cos^2\theta - 1\right). \tag{2.30}$$

We can substitute these expressions into Eq. 2.21 which will give us:

$$\begin{aligned} V_{ij} = -\frac{\sqrt{6}}{4}\Bigg(\frac{\sqrt{6}}{4}\sin^2\theta(e^{+2i\phi}\hat{d}_i^+\hat{d}_j^+ + e^{-2i\phi}\hat{d}_i^-\hat{d}_j^-) + \frac{\sin\theta\cos\theta}{2\sqrt{2}}(e^{+i\phi}(\hat{d}_i^0\hat{d}_j^- + \hat{d}_i^-\hat{d}_j^0) \\ + e^{-i\phi}(\hat{d}_i^0\hat{d}_j^+ + \hat{d}_i^+\hat{d}_j^0)) + \frac{3\cos^2\theta - 1}{12}(\hat{d}_i^+\hat{d}_j^- + \hat{d}_i^-\hat{d}_j^+ + 2\hat{d}_i^0\hat{d}_j^0)\Bigg). \end{aligned} \tag{2.31}$$

Now using Eq. 2.26 and Eq. 2.27 we can simplify Eq. 2.31 to:

$$\begin{aligned} V_{ij} = -\frac{-6}{r^3}\Bigg(\frac{1}{4}\sin^2\theta((\hat{d}_i^x\hat{d}_j^y - \hat{d}_i^y\hat{d}_j^x)\cos(2\phi) + (\hat{d}_i^x\hat{d}_j^y + \hat{d}_j^x\hat{d}_i^y\sin(2\phi))) \\ \frac{\sin\theta\cos\theta}{2}((\hat{d}_i^z\hat{d}_j^x + \hat{d}_i^x\hat{d}_j^z)\cos\phi + (\hat{d}_i^z\hat{d}_j^y + \hat{d}_i^y\hat{d}_j^z)\sin\phi) \\ \frac{3\cos^2\theta - 1}{12}(2\hat{d}_i^z\hat{d}_j^z - \hat{d}_i^x\hat{d}_j^x - \hat{d}_i^y\hat{d}_j^y)\Bigg). \end{aligned} \tag{2.32}$$

We can use the trigonometric identities: $\sin\phi = \frac{y}{\sqrt{x^2+y^2}}$ $\cos\phi = \frac{x}{\sqrt{x^2+y^2}}$, $\sin(2\phi) = \frac{2xy}{x^2+y^2}$ and $\cos(2\phi) = \frac{x^2-y^2}{x^2+y^2}$ to obtain

$$\begin{aligned} V_{ij} = \frac{1}{r^3}(d_i^x d_j^x + d_i^y d_j^y + d_i^z d_j^z) - \frac{3}{r^5}(d_i^x d_j^x x^2 + d_i^y d_j^y y^2 + d_i^z d_j^z z^2 \\ xy(d_i^y d_j^x + d_i^x d_j^y) + xz(d_i^z d_j^x + d_i^x d_j^z) + yz(d_i^z d_j^y + d_i^y d_j^z)). \end{aligned} \tag{2.33}$$

This simplifies to

$$V_{ij} = \frac{\boldsymbol{\mu_i} \cdot \boldsymbol{\mu_j}}{r^3} - 3\frac{(\boldsymbol{\mu_i} \cdot \boldsymbol{r})(\boldsymbol{\mu_j} \cdot \boldsymbol{r})}{r^3}, \tag{2.34}$$

which gives us the equivalency to Eq. 2.21. For this chapter we will only consider the $q = 0$ terms in Eq. 2.21 as these are the only terms that conserve energy [69]. The $q = 0$ term is:

$$V_{ij} = \frac{1 - 3\cos^2\theta_{ij}}{r_{ij}^3}\left(\hat{d}_i^0\hat{d}_j^0 + \frac{\hat{d}_i^+\hat{d}_j^- + \hat{d}_i^-\hat{d}_j^+}{2}\right). \tag{2.35}$$

This term will come in useful in the next part of the Hamiltonian derivation.

2.3.3 XXZ Hamiltonian

It is important to consider which energy levels of our rotational structure we will map the pseudospins in our lattice to. Conventionally we choose $|\downarrow\rangle = \left|\tilde{N} = \tilde{0}, M_N = 0\right\rangle$ and $|\uparrow\rangle = \left|\tilde{N} = \tilde{1}, M_N = 0\right\rangle$ or $|\uparrow\rangle = \left|\tilde{N} = \tilde{1}, M_N = \pm 1\right\rangle$ [59]. For the purposes of keeping this derivation simple we will limit ourselves to: $|\uparrow\rangle = \left|\tilde{1}, 0\right\rangle$. The next step is to derive the relevant dipole operator matrix elements for this system which we shall denote as:

$$\hat{d}_\downarrow = \left\langle\tilde{0}, 0\right| \hat{d}^z \left|\tilde{0}, 0\right\rangle, \tag{2.36}$$

$$\hat{d}_\uparrow = \left\langle\tilde{1}, 0\right| \hat{d}^z \left|\tilde{1}, 0\right\rangle, \tag{2.37}$$

and

$$\hat{d}_{\uparrow\downarrow} = \left\langle\tilde{1}, 0\right| \hat{d}^z \left|\tilde{0}, 0\right\rangle. \tag{2.38}$$

First we must establish expressions for $\hat{d}_\downarrow$ and $\hat{d}_{\downarrow\uparrow}$. Recall from Eq. 2.18 we can express this state like

$$\left|\tilde{0}, 0\right\rangle = \sum_N c_N \left|N, 0\right\rangle, \tag{2.39}$$

so it follows that:

$$\hat{d}_\downarrow = \left\langle\tilde{0}, 0\right| \hat{d}^z \left|\tilde{0}, 0\right\rangle = \sum_{N'} c_N'^* \left\langle N', 0\right| \hat{d}^z \sum_N c_N \left|N, 0\right\rangle = \sum_{N'}\sum_N c_N'^* c_N \left\langle N', 0\right| \hat{d}^z \left|N, 0\right\rangle. \tag{2.40}$$

From Eq. 2.15 we get:

$$\langle N,0|\,\hat{d}^z\,|N',0\rangle = \\ d_0\sqrt{(2N+1)(2N'+1)}\begin{pmatrix} N & 1 & N' \\ 0 & 0 & 0 \end{pmatrix}\begin{pmatrix} N & 1 & N' \\ 0 & 0 & 0 \end{pmatrix}. \tag{2.41}$$

The 3j symbol expands:

$$\begin{pmatrix} N & 1 & N' \\ 0 & 0 & 0 \end{pmatrix} = \\ (-1)^N \delta_{N,N'+1}\sqrt{\frac{N}{(2N+1)(2N'+1)}} + (-1)^{N'}\delta_{N,N'-1}\sqrt{\frac{N'}{(2N+1)(2N'+1)}}. \tag{2.42}$$

As a result of the delta terms in Eq. 2.42 which arise from the limitations imposed by the 3j symbol, this turns Eq. 2.40 into:

$$\hat{d}_\downarrow = \sum_N c^*_{N+1} c_N \langle N+1,0|\,\hat{d}^z\,|N,0\rangle\,. \tag{2.43}$$

Now, evaluating this expression with Eq. 2.15 we arrive at the expression:

$$\hat{d}_\downarrow = 2d_0 \sum_N c^*_{N+1} c_N \frac{N+1}{\sqrt{(2N+1)(2N+3)}}. \tag{2.44}$$

Likewise, we can produce a similar analysis for $\hat{d}_{\uparrow\downarrow} = \langle\tilde{1},0|\,\hat{d}^z\,|\tilde{0},0\rangle$. By setting:

$$|\tilde{1},0\rangle = \sum_N b_N |N,0\rangle\,, \tag{2.45}$$

and

$$|\tilde{0},0\rangle = \sum_N a_N |N,0\rangle\,. \tag{2.46}$$

We obtain the expression

$$\hat{d}_{\uparrow\downarrow} = d_0 \sum_N (a_{N+1} b^*_N + a^*_N b_{N+1}) \frac{N+1}{\sqrt{(2N+1)(2N+3)}}. \tag{2.47}$$

We are now armed with the equations needed to construct our lattice Hamiltonian. The Hamiltonian can be found using:

$$H = \sum_{a,b} \langle a| V_{ij} |b\rangle |a\rangle \langle b|. \tag{2.48}$$

Here the wavefunctions $|a\rangle$ and $|b\rangle$ are the coupled states of our two molecules in their two level system: $|{\downarrow_i}{\downarrow_j}\rangle$,$|{\uparrow_i}{\downarrow_j}\rangle$,$|{\downarrow_i}{\uparrow_j}\rangle$ and $|{\uparrow_i}{\uparrow_j}\rangle$ where the arrows represent the state of the respective molecule.

Consider the case where $|a\rangle = |b\rangle = |{\downarrow_i}{\downarrow_j}\rangle$. Substituting this into the first term of Eq. 2.48 we get:

$$\langle {\downarrow_i}{\downarrow_j}| V_{ij} |{\downarrow_i}{\downarrow_j}\rangle |{\downarrow_i}{\downarrow_j}\rangle \langle {\downarrow_i}{\downarrow_j}| \,. \tag{2.49}$$

To evaluate this we will return to Eq. 2.35, put here for convenience:

$$V_{ij} = \frac{1-3\cos^2\theta_{ij}}{r_{ij}^3}\left(\hat{d}_i^0\hat{d}_j^0 + \frac{\hat{d}_i^+\hat{d}_j^- + \hat{d}_i^-\hat{d}_j^+}{2}\right). \tag{2.50}$$

We can ignore the $\hat{d}^{\pm}$ terms since we are only focusing on the $M_N = 0$ states for now. Eq. 2.49 then becomes:

$$\begin{aligned}
&\langle {\downarrow_i}{\downarrow_j}| V_{ij} |{\downarrow_i}{\downarrow_j}\rangle |{\downarrow_i}{\downarrow_j}\rangle \langle {\downarrow_i}{\downarrow_j}| = \\
&\qquad \frac{1-3\cos^2\theta_{ij}}{r_{ij}^3} \langle {\downarrow_i}{\downarrow_j}| \hat{d}_i^0\hat{d}_j^0 |{\downarrow_i}{\downarrow_j}\rangle |{\downarrow_i}{\downarrow_j}\rangle \langle {\downarrow_i}{\downarrow_j}| = \\
&\qquad \frac{1-3\cos^2\theta_{ij}}{r_{ij}^3} \langle {\downarrow_i}| \hat{d}_i^0 |{\downarrow_i}\rangle \langle {\downarrow_j}| \hat{d}_j^0 |{\downarrow_j}\rangle |{\downarrow_i}{\downarrow_j}\rangle \langle {\downarrow_i}{\downarrow_j}| \,.
\end{aligned} \tag{2.51}$$

From Eq. 2.27 $\hat{d}_i^0 = \hat{d}_i^z$ and from definition Eq. 2.36, $\hat{d}_\downarrow = |{\downarrow}\rangle \hat{d}^z \langle {\downarrow}|$, this expression evaluates to:

$$\langle {\downarrow_i}{\downarrow_j}| V_{ij} |{\downarrow_i}{\downarrow_j}\rangle |{\downarrow_i}{\downarrow_j}\rangle \langle {\downarrow_i}{\downarrow_j}| = \frac{1-3\cos^2\theta_{ij}}{r_{ij}^3}\hat{d}_\downarrow^2 |{\downarrow_i}{\downarrow_j}\rangle \langle {\downarrow_i}{\downarrow_j}| \,. \tag{2.52}$$

This gives us the first matrix element for the Hamiltonian, the others are evaluated like so:

$$\begin{aligned}
&\langle\downarrow_i\uparrow_j| V_{ij} |\uparrow_i\downarrow_j\rangle |\downarrow_i\uparrow_j\rangle \langle\uparrow_i\downarrow_j| = \\
&\qquad \frac{1-3\cos^2\theta_{ij}}{r_{ij}^3} \langle\downarrow_i\uparrow_j| \hat{d}_i^0\hat{d}_j^0 |\uparrow_i\downarrow_j\rangle |\downarrow_i\uparrow_j\rangle \langle\uparrow_i\downarrow_j| = \\
&\qquad\qquad \frac{1-3\cos^2\theta_{ij}}{r_{ij}^3}\hat{d}^2_{\uparrow\downarrow} |\downarrow_i\uparrow_j\rangle \langle\uparrow_i\downarrow_j|,
\end{aligned} \tag{2.53}$$

$$\begin{aligned}
&\langle\downarrow_i\uparrow_j| V_{ij} |\downarrow_i\uparrow_j\rangle |\downarrow_i\uparrow_j\rangle \langle\downarrow_i\uparrow_j| = \\
&\qquad \frac{1-3\cos^2\theta_{ij}}{r_{ij}^3} \langle\downarrow_i\uparrow_j| \hat{d}_i^0\hat{d}_j^0 |\downarrow_i\uparrow_j\rangle |\downarrow_i\uparrow_j\rangle \langle\downarrow_i\uparrow_j| = \\
&\qquad\qquad \frac{1-3\cos^2\theta_{ij}}{r_{ij}^3}\hat{d}_\downarrow\hat{d}_\uparrow |\downarrow_i\uparrow_j\rangle \langle\downarrow_i\uparrow_j|,
\end{aligned} \tag{2.54}$$

and

$$\langle\uparrow_i\uparrow_j| V_{ij} |\uparrow_i\uparrow_j\rangle |\uparrow_i\uparrow_j\rangle \langle\uparrow_i\uparrow_j| = \frac{1-3\cos^2\theta_{ij}}{r_{ij}^3}\hat{d}^2_\uparrow |\uparrow_i\uparrow_j\rangle \langle\uparrow_i\uparrow_j|. \tag{2.55}$$

Substitution of these into Eq. 2.48 gives us:

$$H = \frac{1-3\cos^2\theta_{ij}}{r_{ij}^3}\begin{pmatrix} \hat{d_\downarrow}^2 & 0 & 0 & 0 \\ 0 & \hat{d}_\downarrow\hat{d}_\uparrow & \hat{d_{\downarrow\uparrow}}^2 & 0 \\ 0 & \hat{d_{\downarrow\uparrow}}^2 & \hat{d}_\downarrow\hat{d}_\uparrow & 0 \\ 0 & 0 & 0 & \hat{d_\uparrow}^2 \end{pmatrix}. \tag{2.56}$$

We will now define three new spin-1/2 operators. These are defined as:

$$\hat{S}_i^z = \frac{1}{2}(|\uparrow_i\rangle\langle\uparrow_i| - |\downarrow_i\rangle\langle\downarrow_i|), \tag{2.57}$$

$$\hat{S_i^+} = |\uparrow_i\rangle\langle\downarrow_i|, \tag{2.58}$$

and

$$\hat{S_i^-} = (\hat{S_i^+})^\dagger. \tag{2.59}$$

With these operators we can write Eq. 2.56 as:

$$H = \frac{1 - 3\cos^2\theta_{ij}}{r_{ij}^3}\left(\frac{J_\perp}{2}(\hat{S_i^+}\hat{S_j^-} + \text{h.c.}) + J_z\hat{S}_i^z\hat{S}_j^z + W(I_i\hat{S}_j^z + \hat{S}_i^z I_j) + VI_iI_j\right). \tag{2.60}$$

Here:

$$J_\perp = 2\hat{d_{\uparrow\downarrow}}^2, \tag{2.61}$$

$$J_z = (\hat{d}_\uparrow - \hat{d}_\downarrow)^2, \tag{2.62}$$

$$W = \frac{\hat{d_\uparrow}^2 - \hat{d_\downarrow}^2}{2}, \tag{2.63}$$

$$V = \frac{(\hat{d}_\uparrow + \hat{d}_\downarrow)^2}{4}, \tag{2.64}$$

and I_i is the identity matrix associated with site i. Finally we can replace the identity matrices with the number density of the molecules on that site, $I_i \to n_i$ which is equal to 1 if occupied and 0 otherwise. With this we can sum over all sites where $i \neq j$,

$$H = \frac{1}{2}\frac{1 - 3\cos^2\theta_{ij}}{r_{ij}^3}\sum_{i\neq j}\left(\frac{J_\perp}{2}(\hat{S_i^+}\hat{S_j^-} + \text{h.c.}) + J_z\hat{S}_i^z\hat{S}_j^z + W(n_i\hat{S}_j^z + \hat{S}_i^z n_j) + Vn_in_j\right). \tag{2.65}$$

The factor of 1/2 ensures we do not count twice. The physical origin of the Ising term, or J_z, comes from the fact that a pair of dipoles in the parallel configuration differ in energy from the dipole pairs in anti-parallel configuration. The $J_\perp$ term arises from the spin flipping between neighbours, allowing interacting sites to swap their spins. The W term accounts for the density-spin interaction and V for the density-density interaction. These values are constants in the unit filling for a lattice and deep lattice sites respectively. Being constants, these last two terms can be ignored which leaves us with an effective Hamiltonian of:

$$H = \frac{1}{2}\frac{1 - 3\cos^2\theta_{ij}}{r_{ij}^3}\sum_{i\neq j}\left(\frac{J_\perp}{2}(\hat{S_i^+}\hat{S_j^-} + \text{h.c.}) + J_z\hat{S}_i^z\hat{S}_j^z\right). \tag{2.66}$$

	Minimum $\frac{J_z}{J_\perp}$	Maximum $\frac{J_z}{J_\perp}$	$J_z = J_\perp$
Field Strength ($\frac{B_0}{d_0}$)	0	5.213	1.700
$\frac{J_z}{J_0}$	0	2.794	1.000
$J_z(d_0^2)$	0	0.434	0.413
$J_\perp(d_0^2)$	0.666	0.155	0.413

Table 2.1: Table showing key values pertaining to Fig. 2.3. These are generalised for bialkali molecules for the $\left|\tilde{0},0\right\rangle$ to $\left|\tilde{1},0\right\rangle$ transition. These values will help us define a reasonable parameter space for our electric field in terms of d_0 and B_0 for the different molecules we can find the specific values.

One can show it is possible to arrive at the same result for $\left|\tilde{0},0\right\rangle \rightarrow \left|\tilde{1},1\right\rangle$ with the exception that $J_\perp = -\hat{d_{\uparrow\downarrow}}^2$.

2.3.4 Interaction Dependence on Electric Fields

Having arrived at the Eq. 2.66 it is intuitive to ask where the electric field comes into play. We note that $J_\perp$ and J_z both depend on the dipole operators. The expectation values of the dipole operators and indeed any value $\langle s_i|\,\hat{d}_p\,|s_j\rangle$ depend on the electric field. It is important to understand how we can use this to tune the interaction strengths and the impact it will have on the Hamiltonian.

Figure 2.3 shows the generalised values of J_z and $J_\perp$ as a function of electric field for a diatomic molecule. The behaviour of the system is governed by the ratio of $J_z/J_\perp$. The useful parameter space is therefore defined by the points where $J_z/J_\perp$ is minimum and maximum. The ratio is shown by the broken green line in Fig. 2.3. Key values for this graph are shown on table 2.1. A list of some exemplar bi-alkali molecules as well as on the homogeneity requirement of the electric fields are discussed later in the chapter.

2.4 Requirements on Electric Fields

For the quantum simulation experiments that we are aiming to do in our apparatus it is essential that the spin exchange interaction stays on resonance between lattice sites.

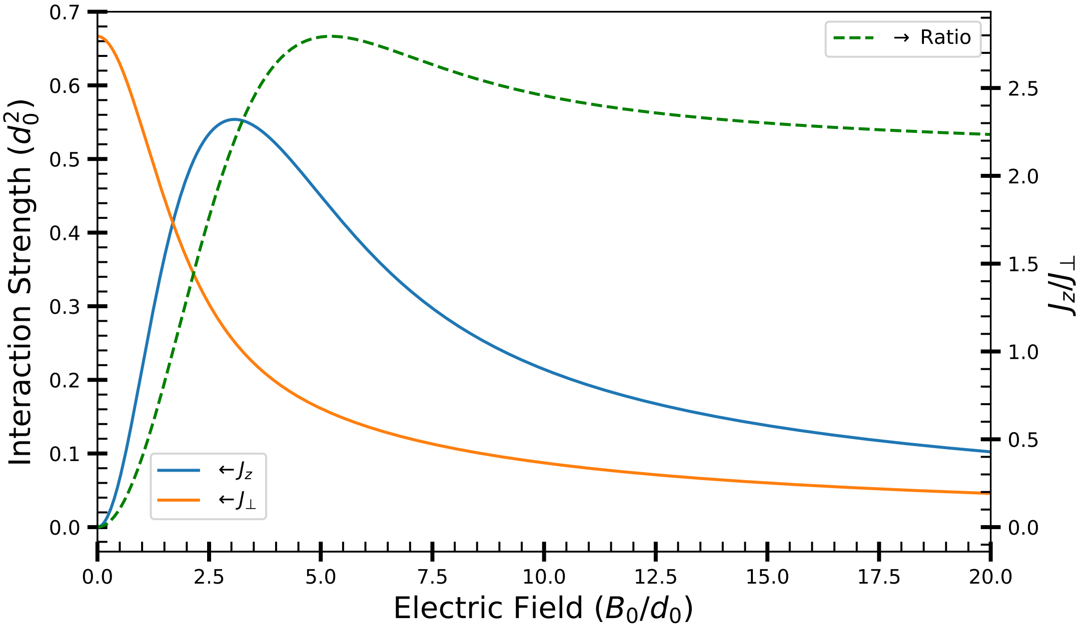

Figure 2.3: Interaction strengths J_z and $J_\perp$ on the left axis for $|0,0\rangle$ and the $|1,0\rangle$ transition. Ratio of J_z to $J_\perp$ on the right axis. Arrows in legend boxes indicate which axis the line belongs to. $J_\perp$ starts off at $d_0^2/3$ and tails off as the electric field is increased. J_z reaches a maximum and drops off again as the field is increased. The green dashed line shows the ratio of J_z to $J_\perp$ and will be used for determining the range of electric fields needed to tune the lattice. Values for specific points are outlined on table 2.1.

2.4.1 Field Gradient

The interaction energy between neighbouring sites must be less than the change in transition energy between those sites (which can result as a fallout of not having a perfectly homogeneous field). This condition can be summarised as

$$h\ df(E) < J_\perp(E), \tag{2.67}$$

where *df* is the *change* in transition frequency between the neighbouring sites [70]. This condition sets precisely what field homogeneity (gradient and curvature of the electric field) is required. We can extract the gradient by a simple application of the chain rule:

$$\frac{df}{dx} = \frac{\partial f}{\partial E}\frac{dE}{dx} \implies \frac{dE}{dx} = \frac{df}{dx} \div \frac{\partial f}{\partial E}. \tag{2.68}$$

	Minimum $\frac{J_z}{J_\perp}$	Maximum $\frac{J_z}{J_\perp}$	$J_z = J_\perp$
Field Strength ($\frac{B_0}{d_0}$)	0	5.213	1.700
$J_\perp(E)/\frac{\partial f}{\partial E}(d_0)$	0	0.023	0.064

Table 2.2: Key fields and values of $J_\perp/\frac{\partial f}{\partial E}$ The field strengths are at the minimum and maximum values of the ratio in Fig. 2.3. The values from the second column are extracted from Fig. 2.5.

From Eq. 2.67 we can see that the maximum allowable gradient is set by $J_\perp$. As such we can set $J_\perp = hdf$. If the lattice spacing (and hence the distance between nearest neighbours) is r then:

$$\frac{df}{dx} \approx \frac{J_\perp(E)}{r}. \tag{2.69}$$

We also note that we can obtain $\frac{\partial f}{\partial E}$ from Fig. 2.1. This is just the derivative of the difference between the two eigenenergies we are mapping the pseudospins to:

$$\frac{\partial f}{\partial E} = \frac{d}{dE}(\epsilon_{|1,0\rangle} - \epsilon_{|0,0\rangle}). \tag{2.70}$$

Substitution into Eq. 2.68 gives:

$$\frac{dE}{dx} = \frac{J_\perp(E)}{r\frac{\partial f}{\partial E}}. \tag{2.71}$$

$\frac{\partial f}{\partial E}$ is plotted in Fig. 2.4 and $J_\perp(E)/\frac{\partial f}{\partial E}$ is plotted in Fig. 2.5. Table 2.2 shows the values of $J_\perp(E)/\frac{\partial f}{\partial E}$ at the key fields pointed out on table 2.1.

It is also important to bear in mind that the graphs printed in Fig. 2.3 - 2.5 use a coefficient in front of the XXZ Hamiltonian of $A = 1\,\mathrm{kg\,s^{-4}\,A^2}$. We have that:

$$A = \frac{1 - 3\cos^2\theta}{4\pi\epsilon_0 r^3}. \tag{2.72}$$

In our case the field is in the lattice plane and will point parallel with one of the lattice vectors. θ is the angle joining the intermolecular vector to the electric field vector. The field will be parallel to the vector joining neighbouring

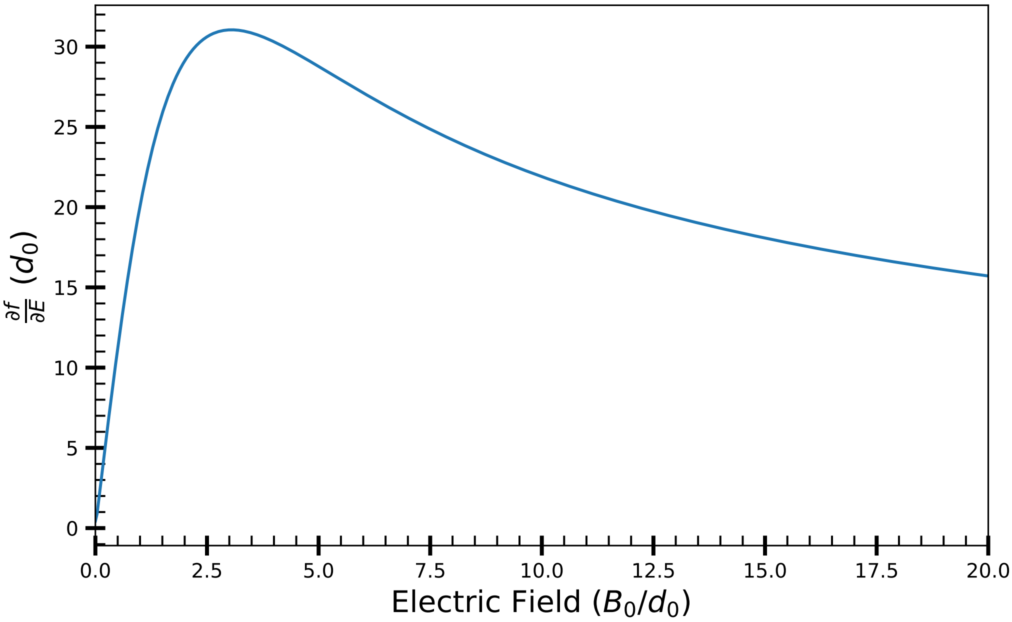

Figure 2.4: Partial derivative of transition frequency between $|1,0\rangle$ and $|0,0\rangle$ as a function of electric field. This will be used as part of Eq. 2.71 to obtain the requirement on the field's gradient. Initially there is a large peak since (from Fig. 2.1) the two levels can clearly be seen moving away from each other in the low field but begin to become parallel in the high field regime hence the line on this plot will begin to tail off.

lattice sites along x but perpendicular to the vector joining lattice sites along y. It is the vector along y that will produce the smaller $J_\perp$ values and therefore this will be the direction limiting our homogeneity. As such we will take $\theta = \frac{\pi}{2}$. It is important to note in this scenario the angle varies depending on which neighbour it is interacting with but for now we will stick with the first nearest neighbour. With $r = 532$ nm, substitution into Eq. 2.72 with the extra quotient of r from 2.71 will yield $A/r = 1.122 \times 10^{35}\,\mathrm{kg\,s^{-4}\,A^2\,m^{-1}}$. We will define a constant $D = 3.3356 \times 10^{-30}\,\mathrm{C\,m}$ which is the number of Debye in SI units. From this we can do a unit conversion: $A/r = 374260\ \mathrm{D^{-1}\,kg\,s^{-4}\,A^2\,C}$ (the unit conversion allows us to use Debye as opposed to SI units). From now on we should consider $J_\perp, J_z \to AJ_\perp, AJ_z$.

Although it may seem as though we have gone to substantial effort to calculate these numbers, we now have a nice expression from which can infer the needed field strengths and associated gradient if we have the permanent dipole moment of the molecule and the rotational constant. The maximum needed field we will need to go to cover the useful ranges of $\frac{J_z}{J_\perp}$ is:

$$E = 5.213\frac{B_0}{d_0}. \tag{2.73}$$

where $\frac{B_0}{d_0}$ is interpreted as the molecule's critical field in $\mathrm{kV\,cm^{-1}}$. Using 2.71 we can arrive at the expression for the maximum allowable gradient at the E-field where $J_z/J_\perp$ is max:

$$\frac{dE}{dx} = 20.48\frac{d_0}{D}, \tag{2.74}$$

which will return units of $\mathrm{V\,cm^{-2}}$. The associated coupling strengths are given by:

$$\frac{J_\perp}{h} = \frac{0.155}{h}Ad_0^2 = 155.4\frac{d_0^2}{D^2}, \tag{2.75}$$

and

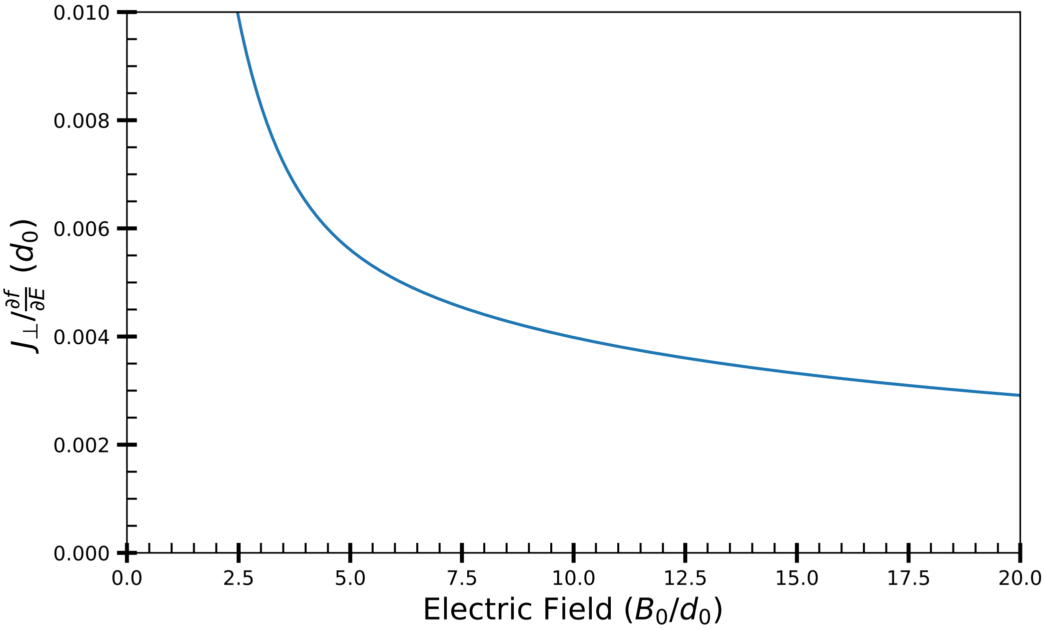

Figure 2.5: Ratio of $J_\perp$ to the derivative of transition energy. This gives us an idea of how sensitive the transition frequency is to the electric field and compares with $J_\perp$.

$$\frac{J_z}{h} = \frac{0.434}{h} A d_0^2 = 435.0 \frac{d_0^2}{D^2}. \tag{2.76}$$

These will return a unit of Hz.

2.4.2 Electric Field Curvature

There is one more value that we will need to calculate and that is the curvature of the electric field. It is possible to approximate the curvature at a small point in space using:

$$\alpha = \frac{1}{x_S} \frac{dE}{dx}. \tag{2.77}$$

where x_S is twice the length of the lattice. We assume we will have a 20×20 lattice and so the length of the lattice is 10.64 µm. Substituting Eq. 2.74 into Eq. 2.77 we obtain a curvature that can be approximated with:

$$\alpha = 192.5 \frac{d_0}{D}. \tag{2.78}$$

which will return a value in units of $\mathrm{kV\,cm^{-3}}$.

2.4.3 Comparison of different molecules.

Armed with these equations we can easily compare a variety of molecules for which we have the values for the rotational constant B_0 and the permanent dipole moment d_0 to determine the fields needed for an experiment involving spin exchange of the nearest neighbours. A comparison is shown on table 2.3. It is of course noticeable that the lighter molecules have smaller rotational constants. As such these molecules will require larger fields to tune through the full range of interaction strengths. This is immediately obvious when comparing the required field strengths for LiK and RbCs and is also advantageous for us since our apparatus is working with the two most massive bialkali molecules (excluding Fr). However, the further apart the two elements are on the periodic table the larger their dipole moment will be. For example, LiCs has the largest dipole moment of 5.53D due to the large asymmetry of charges between the constituent atoms. This has the advantage of having a much more forgiving field gradient and a substantially larger long range interaction strength (since this scales as d_0^2).

Molecule	d_0 (D)	B_0 (GHz)	Critical Field (kV cm^{-1})
LiNa	0.463(2) [71]	11.4 [41]	48.9(2)
LiK	3.45(10) [71]	7.8 [41]	4.49(13)
LiRb	4.00(10) [71]	6.6 [41]	3.28(8)
LiCs	5.52 [40]	5.8 [41]	2.1
NaK	2.76(6) [71]	2.8217297(10) [72]	2.03(4)
NaRb	3.10(30) [71]	2.0896628(4) [73]	1.34(13)
NaCs	4.75(20) [71]	1.78 [41]	0.75(3)
KRb	0.574(17) [74]	1.113950(5) [75]	3.86(11)
KCs	1.906 [40]	0.93 [41]	0.97
RbCs	1.17(6) [31]	0.490173994(4) [37]	0.83(4)

Table 2.3: Comparison of permanent dipole moment, rotational constant and critical field for various bi-alkali molecules. The leftmost column indicates the the molecule, the second is the value of the permanent dipole moment of that particular column and the last column is the critical field.

Molecule	Field at max $J_z/J_\perp$ (kV cm^{-1})	Maximum Allowed Field Gradient (V cm^{-2})	Maximum Allowed Curvature (kV cm^{-3})	$J_\perp$ (Hz)	J_z (Hz)
LiNa	254.9(1.0)	9.48(4)	89.1(4)	33.3(3)	93.3(8)
LiK	23.4(7)	71(2)	644(19)	1850(100)	5200(300)
LiRb	17.1(4)	82(2)	770(19)	2490(120)	700(300)
LiCs	10.9	113	1060	4740	13300
NaK	10.6(2)	56.5(1.2)	531(12)	1180(50)	3310(140)
NaRb	7.0(7)	63(6)	600(60)	1500(300)	4200(800)
NaCs	3.91(16)	97(4)	910(40)	3500(300)	9800(800)
KRb	20.1(6)	11.8(4)	111(3)	51(3)	143(8)
KCs	5.05	39.0	366	564	1580
RbCs	4.33(16)	24.0(1.2)	225(12)	210(20)	590(60)

Table 2.4: Comparison of calculated properties for studying molecules in an optical lattice. The first column is the field at maximum $J_z/J_\perp$ and as such gives the range of electric fields we should work over. The second column gives the maximum gradient at the specified field. If our gradient exceeds this then the spin exchange will be off resonance. The third column gives the maximum allowable curvature and the final two columns give the values of J at the specified field.

2.4.4 Other Transitions

In addition to the $|0,0\rangle \rightarrow |1,0\rangle$ we can consider other transitions as well. Here we consider the transition: $|0,0\rangle \rightarrow |1,1\rangle$. Figure 2.6 shows the interaction strength for the transition $|0,0\rangle \rightarrow |1,1\rangle$. The maximum ratio for this occurs at a field of 3.09 B_0/d_0. However, it only reaches a max ratio of 0.34 and the two J values never cross. Therefore, it offers considerably less tunability than the $|0,0\rangle \rightarrow |1,0\rangle$ transition. Obviously greater jumps, (i.e $|0,0\rangle \rightarrow |2,0\rangle$) are forbidden by selection rules but higher rotational values may be of interest in the far future should we ever wish to study a three level system.

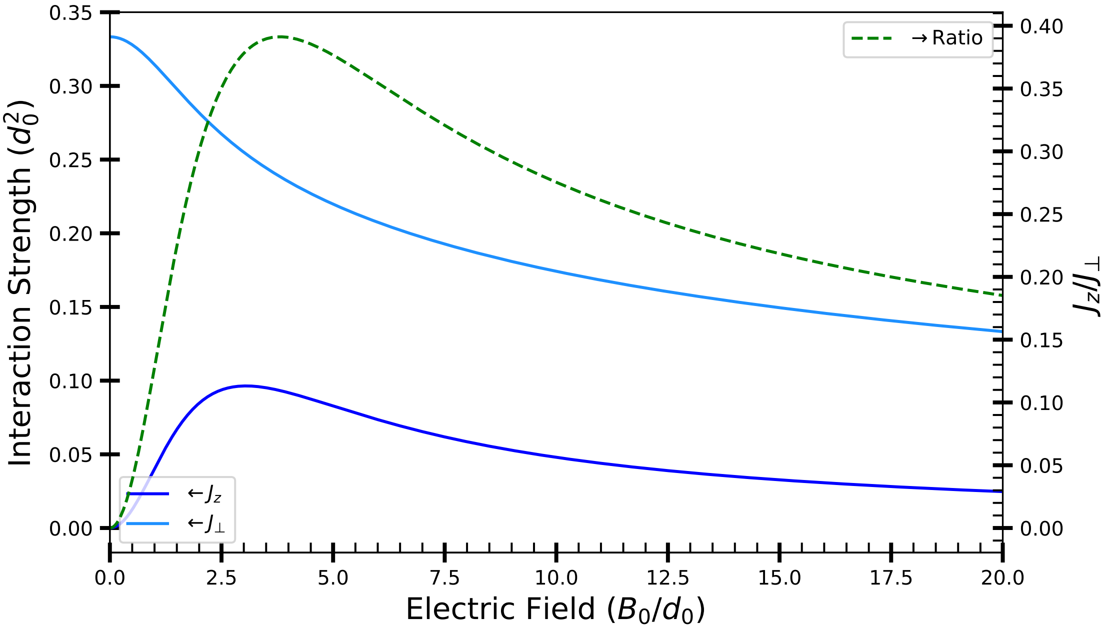

Figure 2.6: Interaction strengths J_z and $J_\perp$ on the left axis for $|0,0\rangle$ and $|1,1\rangle$ transition. Ratio of J_z to $J_\perp$ on the right axis. The blue lines indicate the strengths J_z and $J_\perp$. The green dashed line indicates the ratio $J_z/J_\perp$. In this instance there appears to be no crossing and the two strengths appear to stay far away from each other. The maximum ratio reached is just under 0.35 which would overall make this system more difficult to tune.

2.5 Modelling the Electrode Design

2.5.1 The Current System: Four electrode design

Our current electrode design is based on a four electrode model as shown in Fig. 2.7. The electrodes are made from tungsten and are 2.00 mm in diameter. Tungsten was chosen because it has several advantages. Namely: A high work function which is necessary to reach the electric fields required for our experiment, the material itself is hard which reduces susceptibility to vibrations and gravitational sag, is not sensitive to magnetic fields and has a low coefficient of thermal expansion. There is a vertical separation of 5.57 mm and a horizontal separation of 9.60 mm. The ratio of separation, 1.72, is specifically chosen to minimise the curvature. Analytical solutions to a 2D model shows that the optimal ratio for minimising the curvature of the field is approximately 1.7 [68]. However, this can only minimise the curvature of an electric field pointing along the longer direction of the electrode configuration, it cannot minimise the curvature of a field pointing in the shorter direction. This poses a disadvantage in that it means we cannot rotate the field to vertical. The optical lattice is expected to sit approximately 28 mm from the edge of the four electrode arrangement.

We simulate the electric fields in COMSOL. A surface boundary condition is applied to each electrode. In this simulation specifically the left pair of electrodes have a potential of 2.5 kV and the right pair have a potential of -2.5 kV. A boundary condition of 0 V at infinity is also applied. COMSOL then uses finite element analysis to numerically solve the associated electrostatic equations. The solutions are shown in Fig. 2.8.

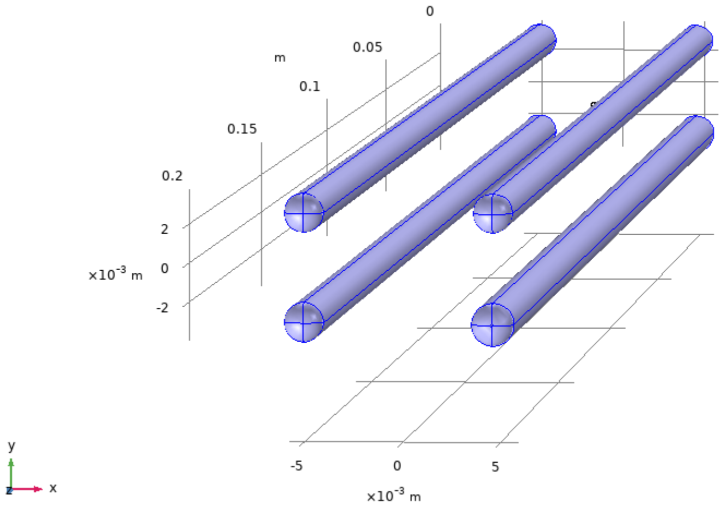

Figure 2.7: Four electrode system. The electrodes are cylindrical with a diameter of 2.00 mm. Each electrode has a hemispherical end of the same diameter. The horizontal separation of the electrodes is 9.60mm and the vertical separation is 5.57 mm. The length of the electrodes are 203mm The molecules are anticipated to sit approximately 28 mm from the edge of the electrode arrangement.

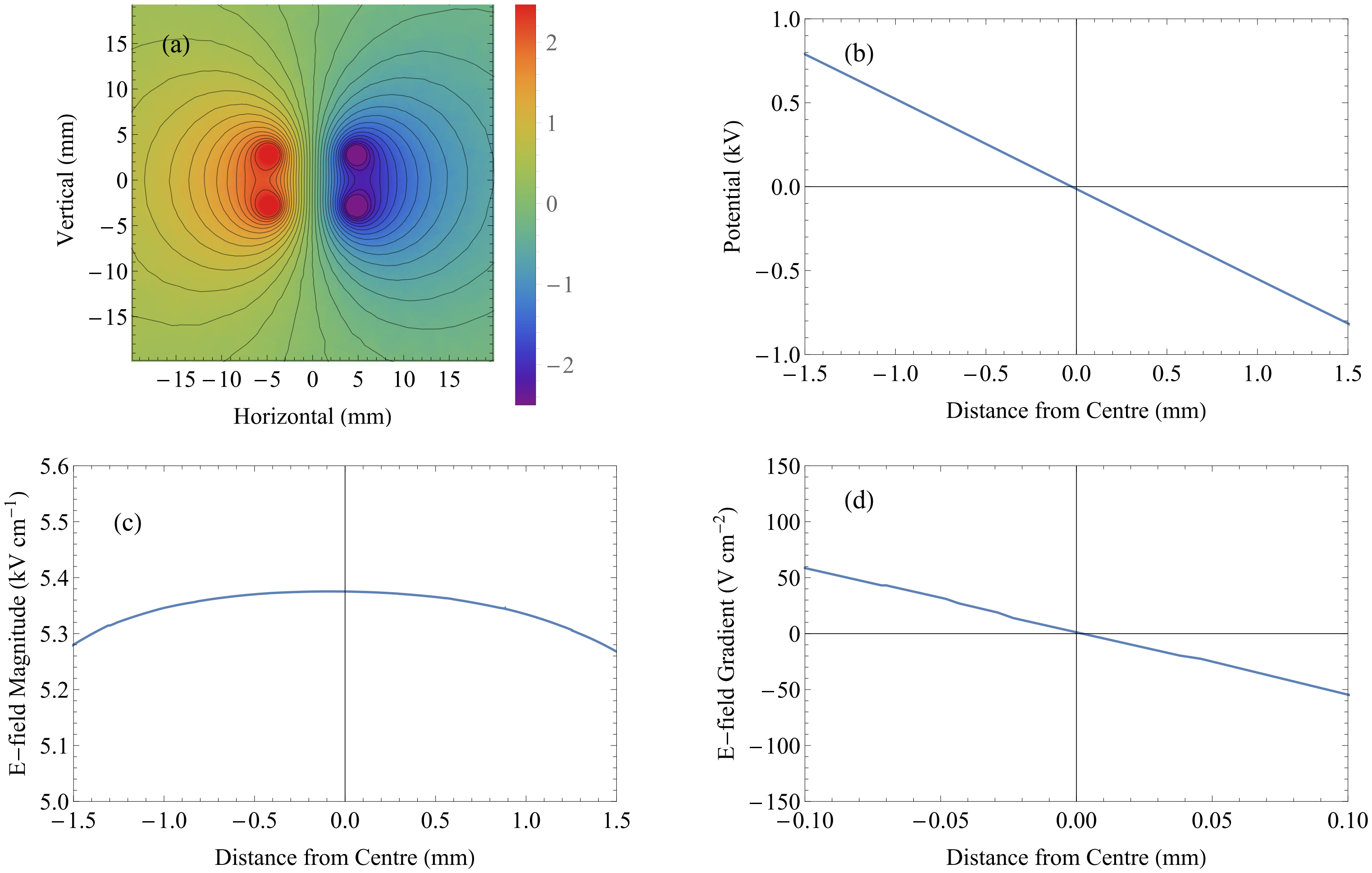

Figure 2.8: 3D COMSOL simulations for the electric field. (a) Density plot of the field's potential, the potential is in kV. (b) Electric potential along horizontal axis in plane of molecules. (c) Electric field magnitude in horizontal axis along plane of molecules. (d) Electric field gradient in horizontal axis along plane of molecules. Note the 'bumps' in some of the results are as a result of machine precision. Further smoothing could be done if simulated on a computer with greater specifications.

At the centre of the arrangement, where we expect the optical lattice to sit, the electric field in the horizontal direction is 5.37 kV cm^{-1}. The vertical component is 0 kV cm^{-1} due to the symmetry and there will be a negligible component along the axes of the rods.

The electric field gradient does not exceed the established maximum gradient of 39 V cm^{-2} in either direction in the lattice plane for at least 60 µm meaning that the entire lattice should be covered and offering some tolerance on the positioning. The electric field's curvature is estimated by the model to be -0.55 kV cm^{-3} which is substantially smaller than the established limit for KCs at 366.9 kV cm^{-3} so it can be treated as effectively negligible. Indeed this is unsurprising since the electrode ratios are specifically chosen to reduce the field curvature as far as possible. However, this is only one dimension and we cannot apply a zero curvature field in the vertical direction.

2.5.2 Upgrades for versatile fields

If we wish to rotate the field into the vertical direction then we must be more creative with the electrode arrangement. One configuration we may wish to upgrade to is the eight electrode configuration. There are no immediate plans to upgrade the science cell, however we may wish to implement changes to our vacuum chamber at some point in the future. Here, an eight electrode model is considered.

We define the horizontal length of a four electrode rectangular configuration as l_x and the length in the vertical direction as l_y. If the electrodes satisfy the ratio $l_x/l_y = 1.7$ then the curvature at the centre is cancelled to 0 for a horizontal field. Likewise, if $l_y/l_x = 1.7$ then the curvature along a vertical field will also be cancelled. If we have two systems of four electrodes, each in a rectangular formation, then if one set of electrodes has the condition $l_x/l_y > 1.7$ and the second set of electrodes satisfies the condition $l_y/l_x > 1.7$ then it is possible to use the configuration to cancel the curvature for a field in any direction [68].

The eight electrode model considered is illustrated in Fig. 2.9. This electrode model can be considered as two rectangular models. The inner four electrodes (inner and outer will refer to positioning along the vertical axis)

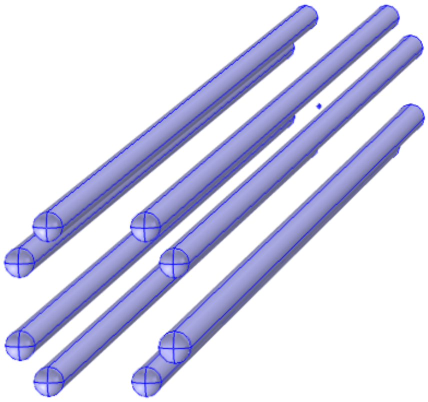

Figure 2.9: Eight electrode system. The inner set of electrodes (along the vertical direction) have a horizontal separation of 10.4 mm and a vertical separation of 5.57 mm. The outer set of four electrodes along the vertical direction have the same separation only oriented at 90°and concentric with the other set of electrodes.

have a horizontal separation of 10.4 mm and a vertical separation of 5.57 mm. Likewise, this outer four electrodes have a horizontal separation of 5.57 mm and a vertical separation of 10.4 mm which ensures the ratios are such that the conditions necessary to cancel the curvatures at the centre in any direction are satisfied.

To demonstrate this model we consider the case where the inner electrodes are fixed and the outer electrodes are varied. The inner left electrodes sit at 2.8 kV and the inner right electrodes at -2.8 kV. The magnitude of the outer electrodes are varied between 0.8 kV and 1.7 kV with the left electrodes being positive and the right electrodes being negative.The results of the model are shown in Fig. 2.10.

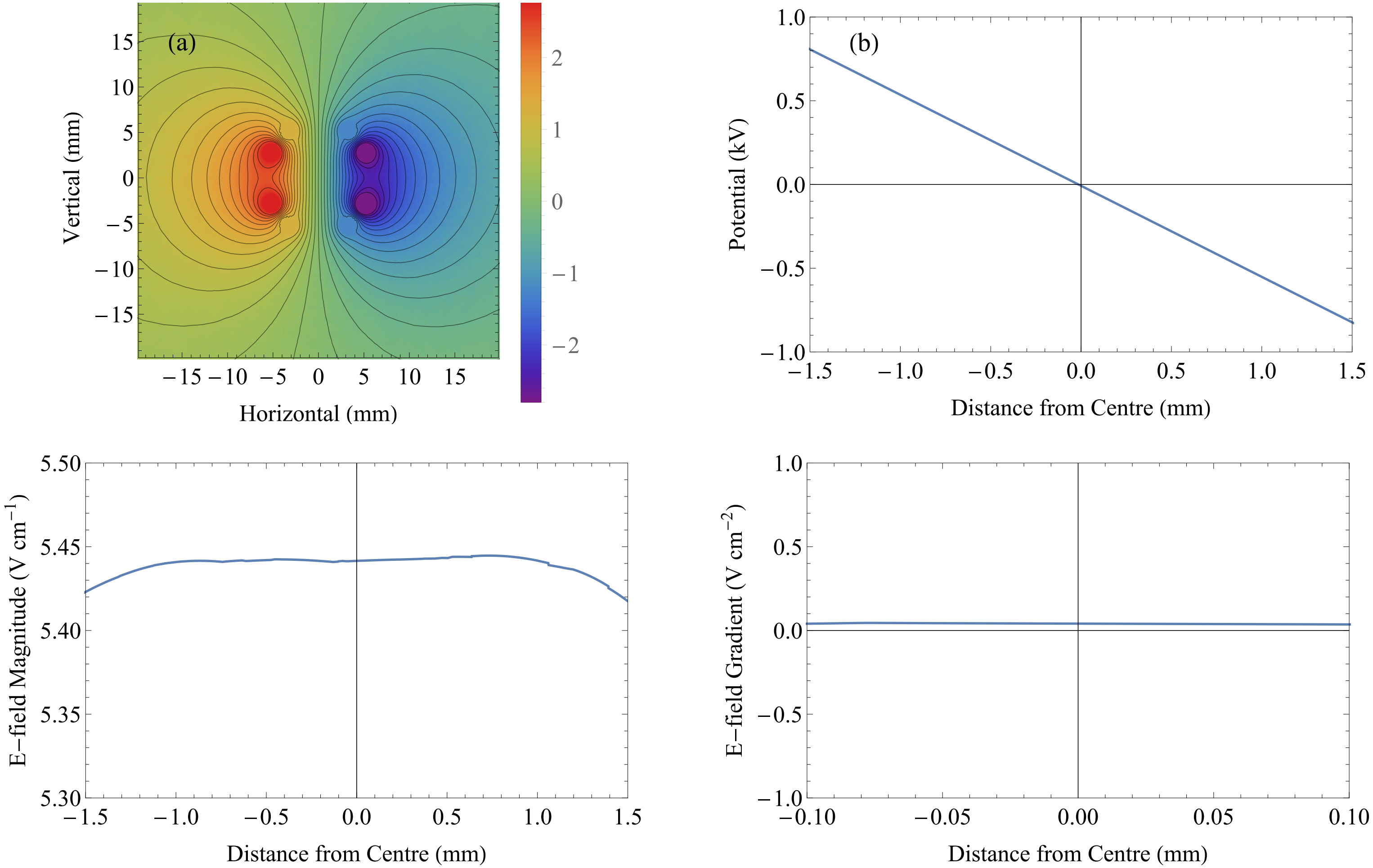

Figure 2.10: 3D COMSOL simulations for the electric field. (a) Density plot of the field's potential, the potential is in kV. For the density plot outer electrodes are at a potential of 1.25 kV. (b) Electric potential along horizontal axis in plane of molecules. (c) Electric field magnitude in horizontal axis along plane of molecules. (d) Electric field gradient in horizontal axis along plane of molecules. Note the 'bumps' in some of the results are as a result of machine precision. Further smoothing could be done if simulated on a computer with greater specifications.

The curvature crosses 0 kV cm^{-3} at an outer electrode potential of approximately 1.25 kV. We see from Fig. 2.10 that the electric field is very flat at this voltage. In addition, the gradient of the field has improved by an order of magnitude.

Since the electrode configuration is symmetric through a rotation of 90°then flipping the field into the vertical configuration should also be quite trivial. The improved results for the gradient and curvature also offer far better tolerance when positioning our lattice with our optical transport.

It would seem that an eight electrode model may be well worth pursuing in the future. Another configuration that has been considered is a four electrode model with capacitor plates that would generate a field along the horizontal or vertical for gradient and curvature correction [68, 70, 76]. This has the advantage of providing near parallel field lines over a wide area. But there are two distinct disadvantages. First, unless 4 plates are installed, the configuration will only work in one direction. Second, a hole in the plate is necessary for optical access. This hole will positioned directly in the axis of the optical lattice which may result in unwanted deformities in the field.

Chapter 3

The Vacuum Chamber

3.1 Introduction

This chapter will offer an overview of our vacuum chamber setup. Figure 3.1 shows an inventor drawing of the vacuum chamber. The vacuum chamber was designed before my PhD began and has been constructed throughout the course of this PhD as part of a team effort. The entire vacuum chamber was baked towards the start of my PhD in early 2019. Various extensions have been added including a magnetic trap in the main chamber for K which we will discuss later in this chapter.

The chapter will first give a broad overview of the chamber and its different parts. Then the 2D-MOT, main chamber and the science cell will be each summarised in more detail.

3.2 Vacuum Chamber Overview

3.2.1 Vacuum Chamber Parts

Figure 3.2 shows the vacuum chamber from the top down view. From this viewpoint the vacuum chamber can be divided into four regions. The $2D^+$-MOTs: one for Cs and one for K and Rb. Our alkali dispensers distribute a thermal vapour of the atomic species into the $2D^+$-MOT glass cell. The

2D$^+$-MOT gathers the atoms into a thin atomic beam where they are directed towards the main chamber. Near the centre of the main chamber three pairs of near resonant beams overlap to create a 3D-MOT. Here is where the bulk of the cooling process for both species occurs including: molasses, degenerate Raman sideband cooling and evaporative cooling. When the atoms are sufficiently cooled optical transport is used to move the atoms to the science cell. In the science cell, atoms will be associated into molecules. Additional molasses beams and lattice beams act to create the optical lattice to trap and image the atoms. The microscope objective is located directly underneath the science cell.

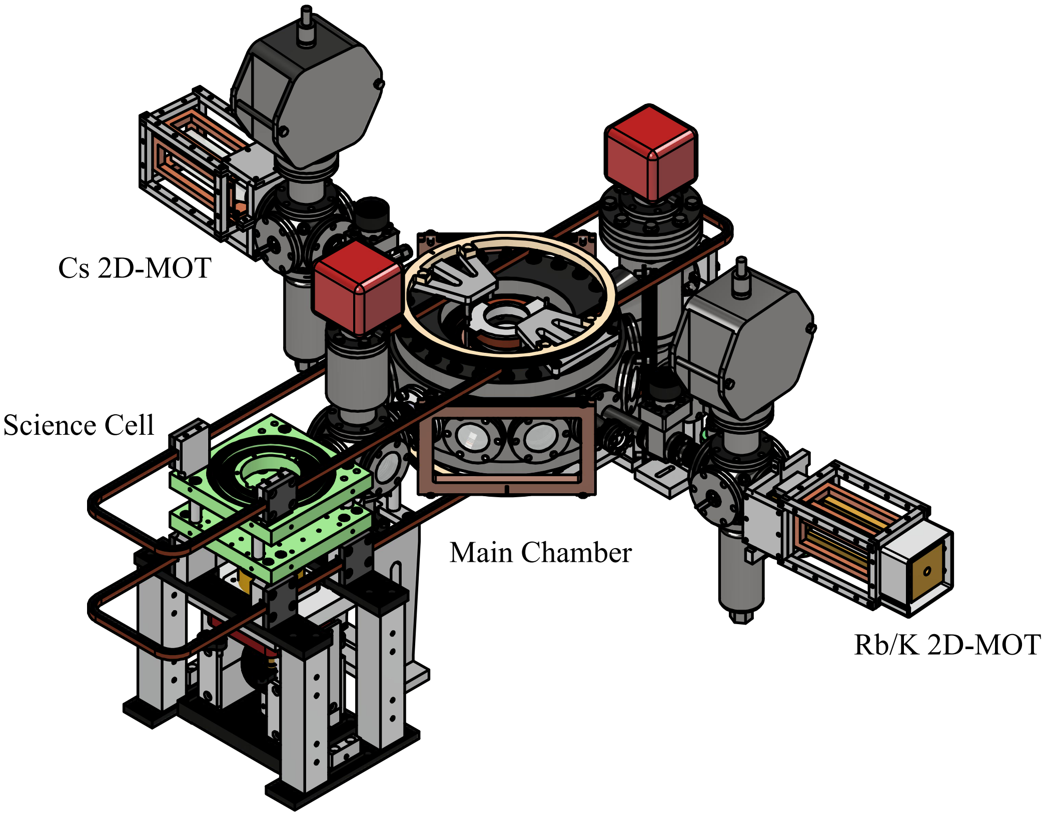

Figure 3.1: Inventor drawing of the full vacuum chamber.

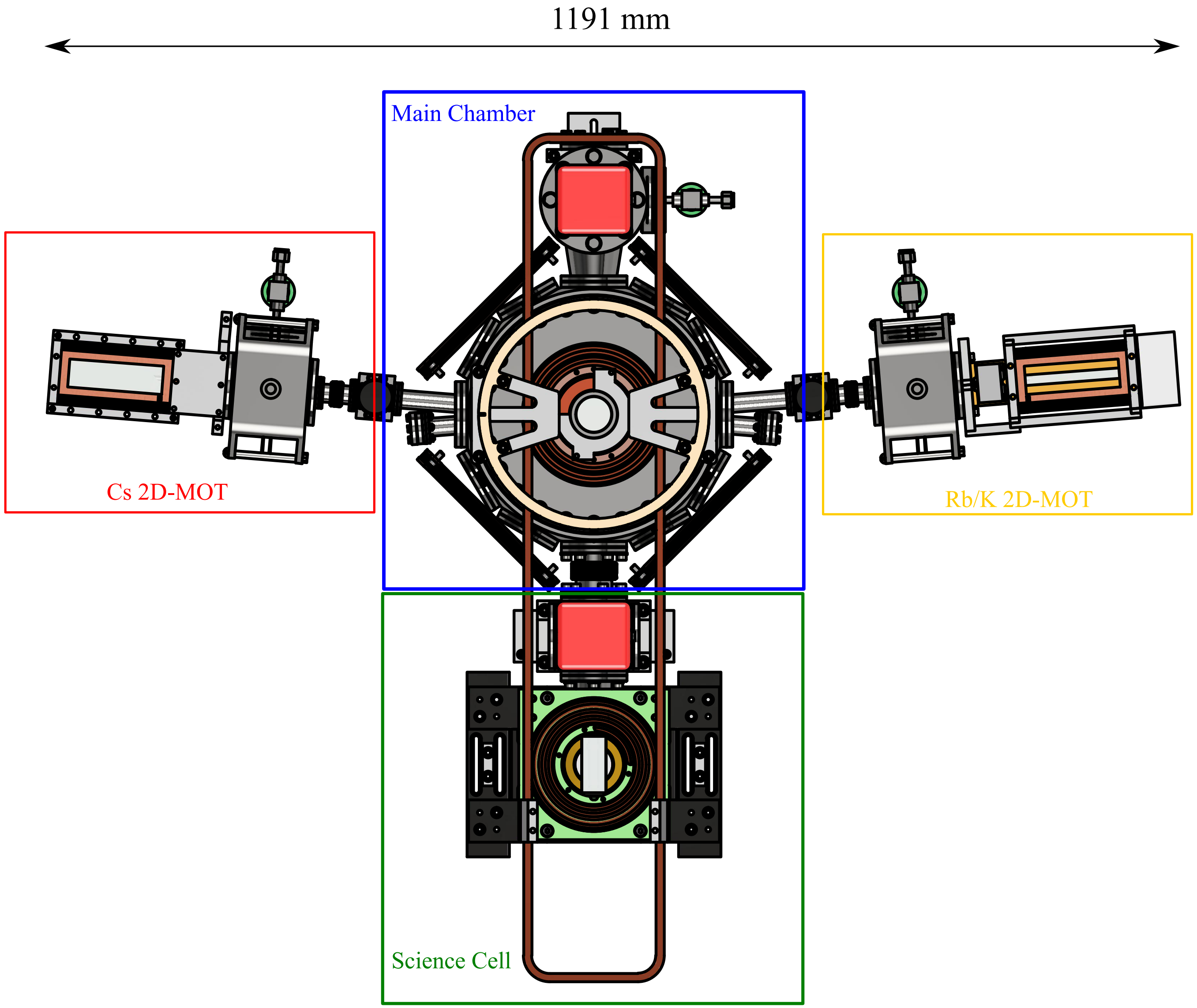

Figure 3.2: Vacuum chamber layout from the top down view. Different parts of the chamber have been highlighted. The red and yellow regions are the Cs and the Rb/K 2D-MOTs respectively. These are connected by differential pumping tubes to the main chamber in the centre highlighted by the blue square. The final part, highlighted by the green square, is our science cell. A large pair of rectangular coils cover the centre of the main chamber and the centre of the science cell. These are the racetrack coils.

3.2.2 Vacuum Chamber Laser Layout

Figure 3.3 shows the laser setup around the main chamber. The main chamber consists of eight large viewports around the side and two recessed viewports along the vertical and directly over the centre of the chamber. In addition, there are two smaller viewports on the side of the chamber, next to the access for the 2D-MOT, for fluorescence imaging. Two opposite positions for a view port are occupied by an ion pump apparatus. One of these ion pumps has a viewport on the side facing away from the chamber. The other is connected to the science cell. These also allow access to the chamber for our science cell lattice and transport beams.

There are three pairs of MOT beams which are prepared on another optics table. Each pair has one Cs beam and Rb/K. Rb and K are overlapped since they share the same fibre from the main table. Each of the these beams are retroreflected at the opposite side of the chamber for a molasses configuration.

The reservoir laser has a wavelength of 1064 nm. The reservoir beam is in a bow tie configuration to ensure atom a high number density is maintained in the centre of the chamber. Part of this reservoir is split off and sent to the science cell. There are two dimple traps which both load from the reservoir. These are used to both trap and cool the atom sample optically with evaporation.

There is a single beam for polarising K atoms in the main chamber. In the vertical the polariser beam is used for degenerate Raman sideband cooling (DRSC) of Rb and Cs. A probe beam is passed through the chamber for absorption imaging.

A transport beam moves a cooled sample of atoms from the main chamber to the science cell using a standing wave [77]. The science cell also features a low resolution imaging beam which shares a CCD camera with the absorption imaging of the main chamber. Three 1064 nm beams form an optical lattice at the centre of the science cell and three imaging beams form an optical molasses for high resolution imaging. The vertical beams here are retroreflected by the microscope objective.

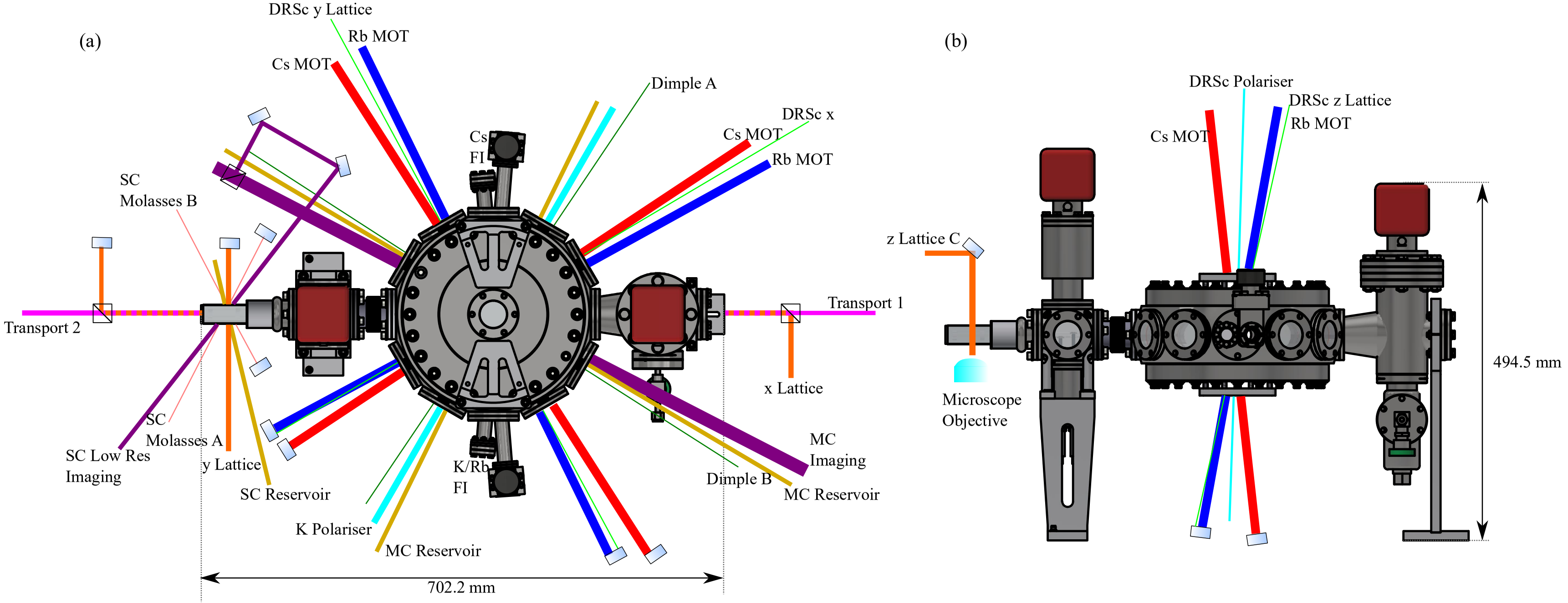

Figure 3.3: Laser layout for main chamber. (a) shows the horizontal beams and (b) shows the vertical beams. The purpose of the beam is indicated by the label next to it. Beams travel away from the label. Some beams are retroreflected as indicated by mirrors (these are the 3D-MOT beams on the main chamber, the science cell molasses beams, and the science cell lattice beams and the DRSC lattice beams). In addition the DRSC lattice beams and the Rb and Cs MOT beams are passed through a $\lambda/4$ waveplate. A PBS is used indicate beams that overlap or split. The two reservoir beams through the main chamber are in a bow tie configuration. The SC acronym stands for science cell. The FI acronym stands for fluorescence imaging.

3.3 2D-MOT

Figure 3.4 shows a drawing of the Rb/K 2D-MOT cell. The 2D-MOT consists of a glass cell centered on a vertical and horizontal pair of rectangular cols. The cell is connected to a spherical cube [Kimball Model: MCF275-SphCube-C6:1]. This cube houses dispensers, is connected to an up-to-air valve on the bottom section and an ion pump on the top. The remaining two horizontal sides, perpendicular to the 2D-MOT, are used for the electrical feed through for the dispensers. The opposite end of the cube is connected to the main chamber. The cell feeds directly to the main chamber via a differential pumping tube. The bellows allow for slight adjustment of the 2D-MOTs' cell angles to allow us to adjust the trajectory of the atomic beam. There is a valve separating the main chamber from the 2D-MOT which can be opened or closed by hand.

3.3.1 Cell

The 2D-MOT cell is a quartz glass cell manufactured by Precision Glassblowing. The cell is rectangular in shape with a truncated conical section at the open end. It is connected to the spherical cube by an indium seal. The dimensions of the interior dimensions of the rectangle are 25 mm × 25 mm × 97.5 mm. The glass is 2.50 mm thick.

These cells are the high vacuum section of the apparatus. It is connected directly to the main chamber by a stainless steel differential pumping tube. This tube is 168 mm in length and has an interior diameter of 1.00 mm for the first 100 mm closest to the cell. This thin tube allows the high vacuum condition and high alkali metal vapour pressure to be maintained at the 2D-MOT cell side whilst maintaining the ultra-high vacuum condition in the main chamber. The end of the tube facing the 2D-MOT has a polished 45°surface. This can be used for reflecting the push beam for a $2D^{+}$-MOT configuration.

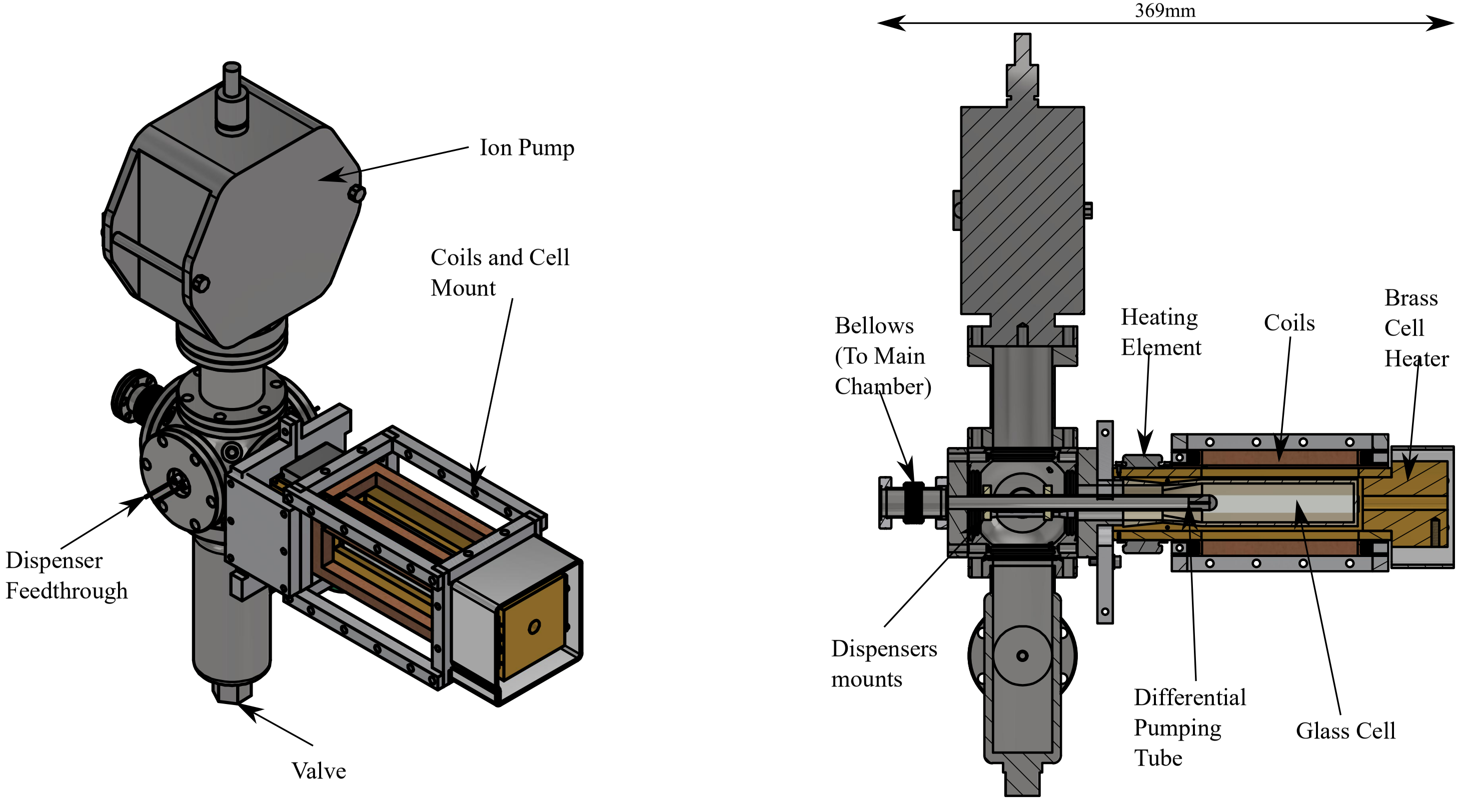

Figure 3.4: Scale drawing of Rb/K 2D MOT. Left is viewed from a 45°angle. The right is a side-on view of from the left of the 2D-MOT (as viewed facing towards the chamber). The cross sectional cut is the plane through the centre of the cell.

3.3.2 Dispensers and Ion Pump

We have four dispensers in operation in our chamber. On the Cs 2D-MOT there are two AlfaVakuo: AS-CsBi25-0100-3F dispensers, and on the Rb/K side we have one AS-RbBi40-0100-3F dispenser and one AS-KBi40-0100-3F dispenser. The dispensers are mounted to the differential pumping tube with macor disks. These are housed inside the spherical cube and electrical access for the dispensers is on the side of the cube. The K dispensers are ran at 1.8 A when K is in operation. The Rb dispensers are run at 2.2 A every time Rb is active in the experiment. The Cs dispensers are run at 1.2 A for 30 minutes every few weeks which sufficiently maintains the Cs vapour pressure.

The ion-pump model used is Agilent model: VacIon 10 L/s. This maintains the high vacuum condition necessary for a 2D-MOT. Unfortunately, we are unaware of the vapour pressure in our 2D-MOT at present. This is because the pressure is typically measured by evaluating the current required to maintain the vacuum condition. We believe our ion pump has been slightly coated by metallic vapour meaning a higher current is needed to maintain the vacuum condition which means the pressure measurement may not be accurate.

3.3.3 K-Heater

Figure 3.5 shows our home built cell heater for the Rb/K 2D-MOT. This is necessary to maintain a high vapour pressure for the K. We find that running the heater for Rb assists with the Rb atom number as well. The heater consists of four brass plates and a thick base. It is designed to cover the 2D-MOT cell with minimal exposure.

The long plates have a length of 173.5 mm. Each plate has a rectangular hole drilled through it for optical access for our 2D-MOT beams. These holes have dimensions of 100 mm × 11.2 mm each. These plates are 6 mm thick. The rear side of the heater has a thick brass base. The base has dimensions of 55 mm × 55 mm × 36 mm. It has a hole of diameter 9 mm for optical access for the push beam. The interior of the brass housing is blackened to direct black-body radiation inwards towards the cell. The fully assembled

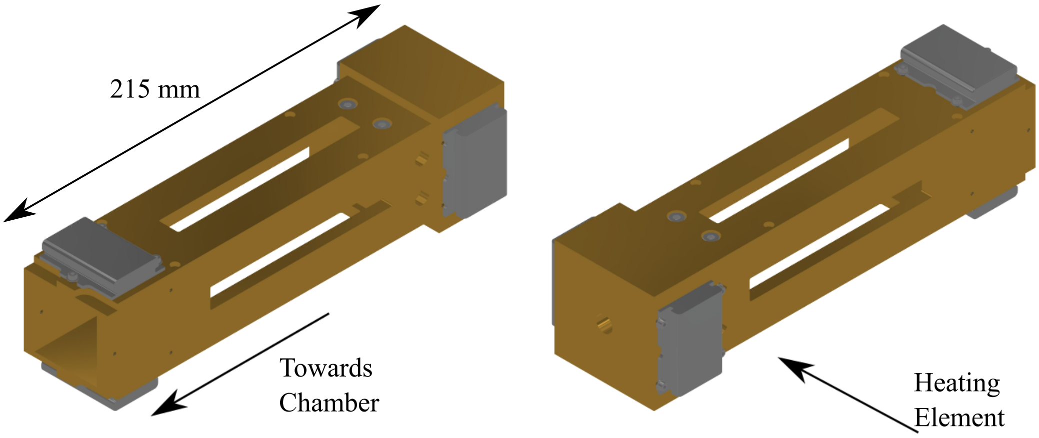

Figure 3.5: Drawing of customised cell heater. Left shows a forward view and right shows the rear view. Direction to chamber is indicated. A single heating element is indicated but there are four total.

heater is designed to slide into the gap between the 2D-MOT coils and the cell.

The brass is heated by four heating elements, two are mounted vertically at the base and two are mounted horizontally at the open end. These are RS models HPG-1/09-40X35-12-30 (90 °C) and HPG-1.5/11-40X35-12-30 (110 °C). The 90 °C region sits at the forward position and the 110 °C site at the base. This allows us to produce a temperature gradient across the cell. This means the pressure will be lower towards the differential pumping tube creating an additional force on the atomic vapour towards the chamber. After the heaters have been on for one hour the temperature stabilises at 80 °C at the base, 52 °C at the open end and 41 °C in the centre. Heating strips are also used to heat the spherical cube.

3.3.4 Coils

The 2D-MOT comprises of two perpendicular pairs of rectangular coils. The coils are shown in Fig. 3.6. The coils are wound from 1 mm diameter copper wire with a thin layer of enamel for insulation. Each rectangular coil is paired with the coil directly opposite it. Each quadrupole coil consists of 6 × 6 windings. The shim forms a 1 × 6 winding layer on top of the quadrupole windings and are in a dipole arrangement with the shims windings opposite.

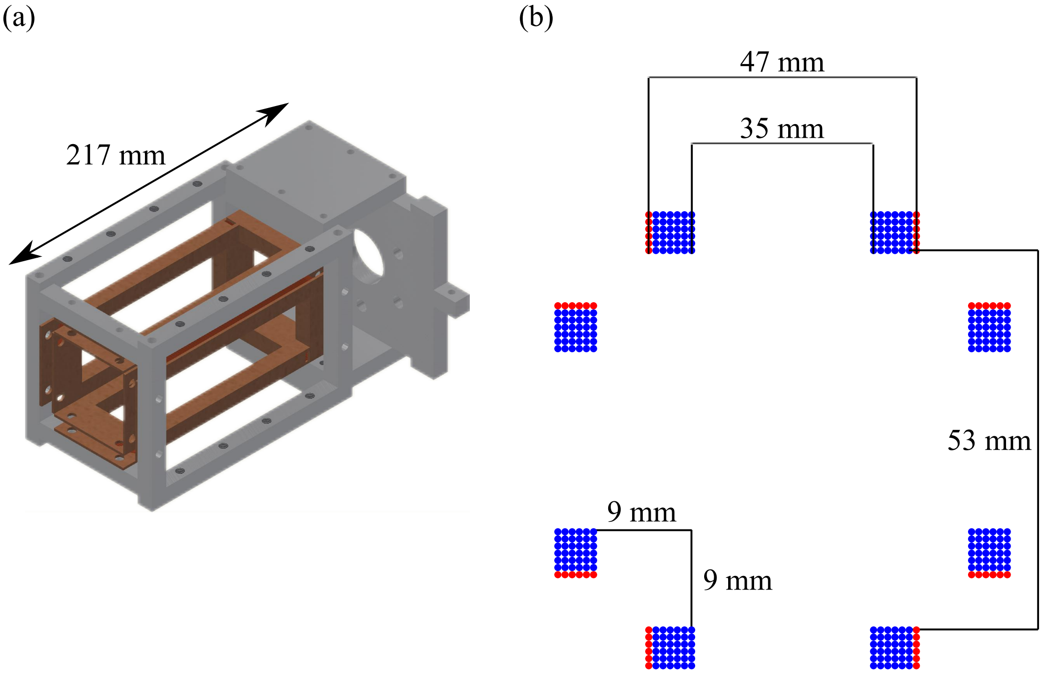

Figure 3.6: (a) Drawing of coils assembly inside mount. (b) Drawing of cross section (along the long direction) of coils with dimensions labelled. Each circle indicates one winding. Blue windings are in the quadrupole arrangement with the winding opposite and red windings are used as shims. Note the length of the long direction of the rectangle is 105 mm on the inner windings and 116 mm on the outer (shim) windings.

For a given quadrupole coil, the shortest width (i.e. the distance between inner most windings) is 35 mm and the greatest width is 45 mm. The shortest length is 105 mm and the longest length is 115 mm. For the shims the widths and lengths are 47 mm and 117 mm respectively. For opposing coils, the separation of the inner most windings is 53 mm and the outermost windings are separated by 63 mm.

Figure 3.7 shows the simulated magnetic for a rectangular pair of coils in our 2D-MOT setup field as a function of position. The horizontal axis corresponds to the axis passing through the centre of a coil with the zero being at the centre of the rectangular pair. The simulation includes the position of each individual winding, as oppose to simply multiplying by the number of windings. The vector is pointing along the direction separating the two coils since the symmetry should cancel all other components along this axis.

The computed gradient of the quadrupole field at the centre is 2.17 G cm^{-1} A^{-1}. Our coils are empirically characterised to have gradients between 2.29 G cm^{-1} A^{-1}

and 2.24 G cm^{-1} A^{-1}. The shim pairs are calibrated to have fields in the range of 0.934 G to 0.916 G at the centre.

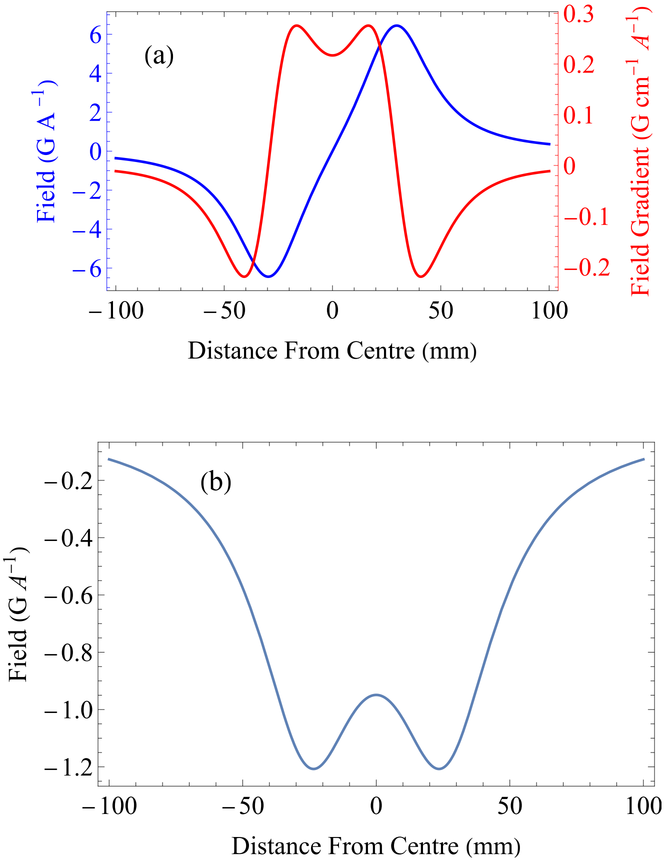

Figure 3.7: Simulated field from 2D-MOT coil rectangular pair. Horizontal axis is along the axis passing through the centre of a coil. The zero of the horizontal axis is at half way between the two coils. (a) Simulated quadrupole field. The blue plot, corresponding to the left vertical axis, gives the field value and the red plot, corresponding to the right axis, shows the field gradient. (b) Simulated shim field.

3.4 Main Chamber

3.4.1 Overview

Figure 3.8 shows the main chamber assembly. The central chamber is manufactured by Kimball [model: MCF1000-Sphdodecagon-H2C12:1] and constructed from stainless steel. Together with the science cell, the main chamber comprises of the ultra-high vacuum parts of our setup. The chamber has 12 sides. Each side has a flange for connecting to other vacuum chamber apparatus. The flanges are numbered in Fig. 3.8. The interior diameter of the chamber (distance between two opposite sides) is 128.70 mm. At the centre of the chamber, where the MOT is captured, the separation between the roof and floor of the chamber is 31.5 mm.

Of the twelve sides, two - sides 3 and 9 - are occupied by the 2D-MOTs. These two flanges are sealed with a custom DN40. Each is split into two smaller openings: one for a half-inch DN16 viewport and another for the 2D-MOT beam access. The DN16 viewport is uncoated and used for the fluorescence imaging.

Side 12, orthogonal to the 2D-MOT axis, is attached to a spherical cube [Kimball Model: MCF275-SphCube-C6:1]. This cube bridges the main chamber to the science cell. The bottom flange of this cube allows the electrical feedthroughs for our science cell electrodes. The top flange is connected to an ion pump [model: NexTorr D 100-5]. Opposite the cube is side 6 which is connected to another ion pump [model: NexTorr Z 200] and the up-to-air valves. The ion pumps are responsible for maintaining the ultra-high vacuum conditions inside our chamber. The exact pressure is unknown since the pressure is low enough so as to not be detectable by the ion pumps' power supplies but we do know the pressure is less than 10^{-10} mbar.

The remaining flanges are all sealed with DN40 1 inch viewports for optical access to the chamber. The top and bottom flanges are sealed with a custom re-entrant flange. The centre has a DN40 1 inch viewport. The main coil assembly, discussed in the next section, rests within the re-entrant section of the flange.

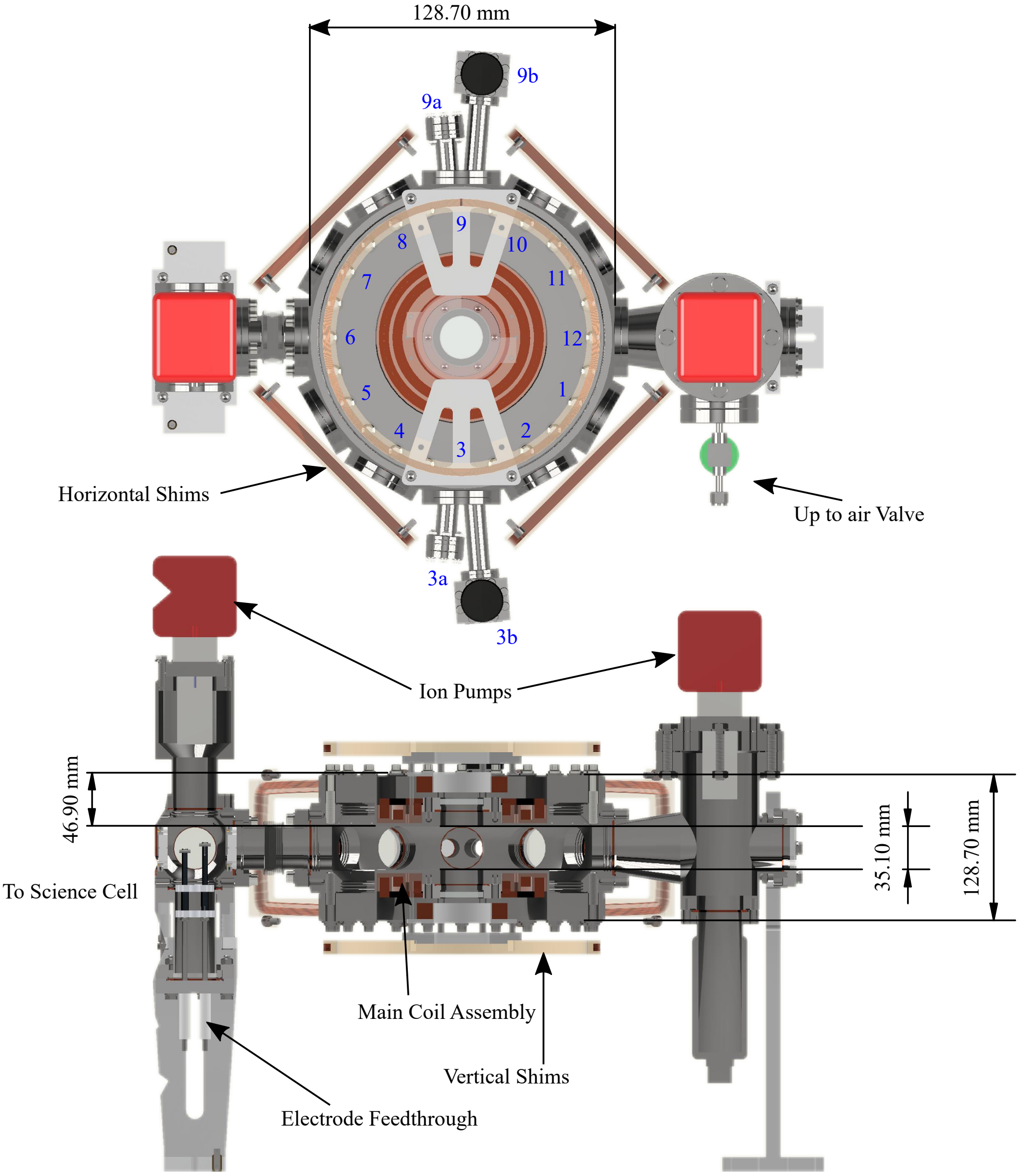

Figure 3.8: Scale drawing of the main chamber arrangement. The top graphic shows the main chamber as viewed from top down. The lower figure is viewed from side on and shows a cross sectional cut. The cut is taken directly across the centre of the chamber facing towards the Cs 2D-MOT. The cut plane includes the optical transport axis. Each side of the chamber is numbered for convenience.

Our viewports are coated with anti-reflective (AR) coating. Most of our viewports are coated with a LaserOptik coating but three are coated with AR coating of unknown origin. We have tested the coating of these viewport with a spectrometer. The transmission of the coatings are shown in Fig. 3.9. Since the LaserOptik coated viewports have proven consistent, only one

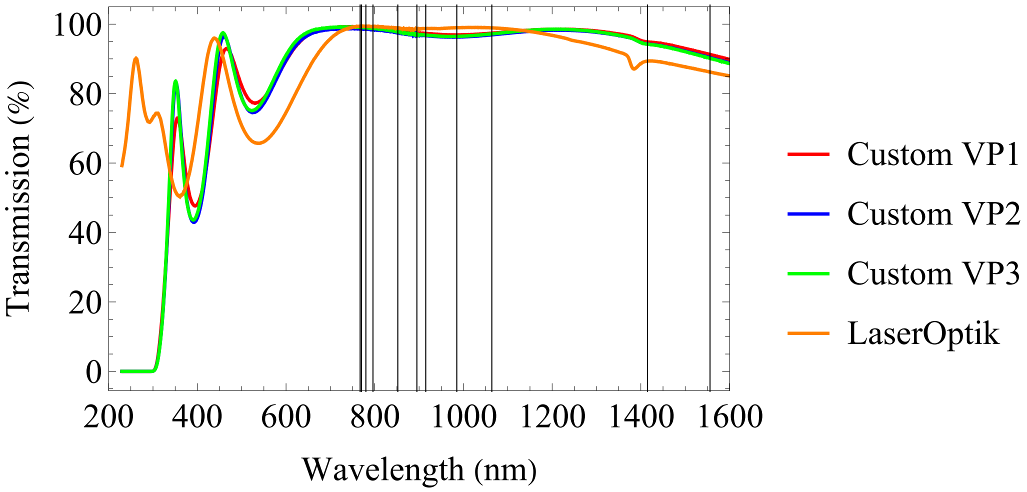

Figure 3.9: Transmission spectrum of viewports, measured with spectrometer. Unknown coatings have been labelled 'Custom VP'. The black lines show where the key wavelengths to be used in the main chamber lie on this graph.

measurement has been shown as an example.

Table 3.1 shows the key wavelengths and the transmission of these wavelengths through our viewport coatings. For all wavelengths that would be used for optical trapping and cooling the transmissions are greater than 97% which is good. The transmissions for the wavelengths that might be used for molecule formation are quite lower but this part of the molecule formation procedure will mainly be performed in the science cell. It is otherwise ideal to know our transmissions if we wish to do molecule formation in the main chamber. Table 3.2 shows which coatings are applied to each viewport.

3.4.2 Main Chamber Coil Assembly

The main chamber coils can be broadly divided into the 'main coil assembly' which consists of the quadrupole coils, bias, jump and magnetic trap coils and the shims which consist of the circular vertical shim coils and two pairs of rectangular coils producing a horizontal shim field.

Figure 3.10 shows the main coil arrangement which rests in the recessed part of the re-entrant flanges. As mentioned: there exist four main sets of coils. The quadrupole, bias and jump coils are glued into a custom homebuilt TUFNOL mount.

Wavelength (nm)	Purpose	Custom Coated VP Transmission Average (%)	LaserOptik Coated VP Transmssion (%)
767	K D_2	99.0	99.4
770	K D_1	99.0	99.4
780	Rb D_2	99.0	99.4
796	Rb D_1	98.8	99.4
852	Cs D_2	97.9	98.8
895	Cs D_1	98.2	98.7
915	KCs Stirap Stokes	97.1	98.8
977	RbCs Stirap Stokes	96.7	99.0
1064	Optical Dipole Traps	97.2	98.9
1415	KCs Stirap Pump	94.7	89.4
1558	RbCs Stirap Pump	91.0	86.2

Table 3.1: Table outlining key wavelengths for the main chamber and their purpose. The transmission of the wavelengths through the various coatings are also listed.

Flange	Coating	Flange	Coating
1	LaserOptik	7	LaserOptik
2	LaserOptik 4	8	Custom VP 4
3a	Uncoated	9a	Uncoated
4	LaserOptik	10	LaserOptik
5	Custom VP5	11	Custom VP 1
Top	LaserOptik	Bottom	LaserOptik

Table 3.2: Viewport coatings. Numbers here reference Fig. 3.8

.

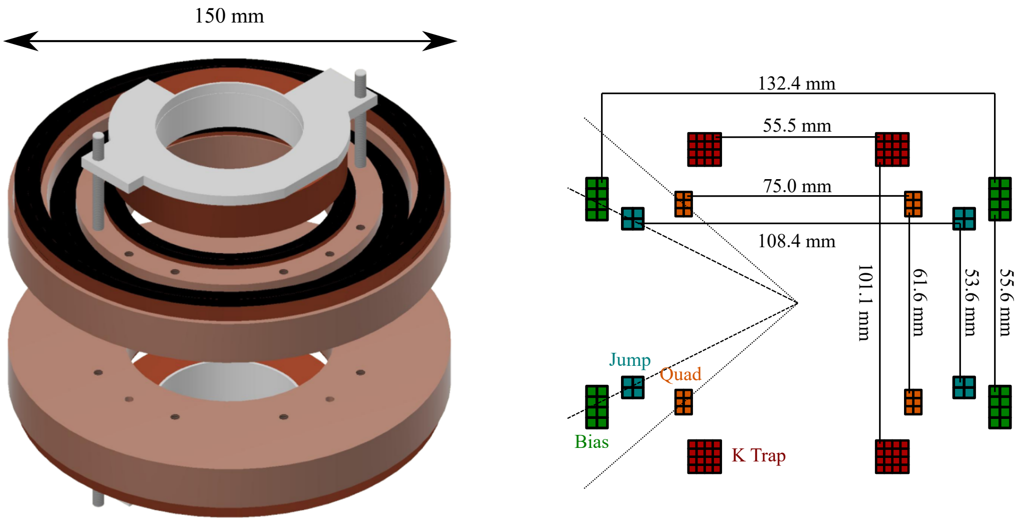

Figure 3.10: Main chamber coil assembly. Left, an inventor drawing of the coil arrangement. Right, a 2D scale drawing of the cross section. Each square represents one coil winding and each colour shows a different coil. From outermost coils to inner most: bias, jump, quad and K trap. Dimensions labelled show the innermost distance between the innermost coils. The cross jump and bias coils are 4.4 mm by 4.4 mm thick and the quadrupole and K trap coils are 3.5 mm by 3.5 mm thick. The diagonal line through the bias and jump coils show where the Helmholtz condition is satisfied and the diagonal line through the quadrupole coil shows where the anti-Helmholtz condition is satisfied.

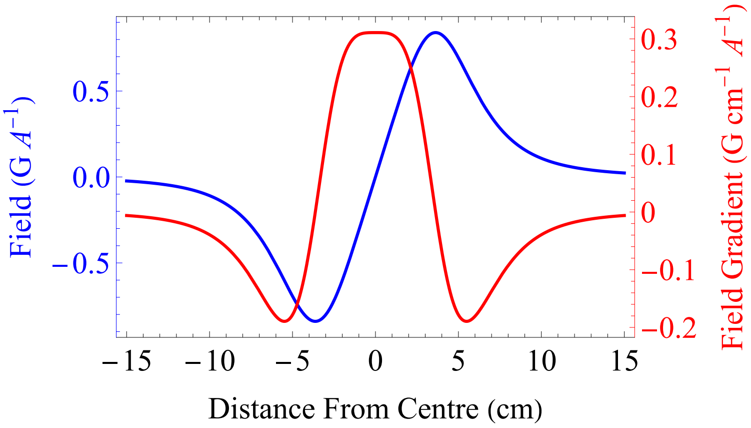

Figure 3.11: Simulated plot of the quadrupole fields (blue, left axis) and the field gradient (red, right axis) through the central axis along the direction of separation.

Quadrupole Coils

The quadrupole coils are in a 2 × 3 winding arrangement. The inner diameter of the coils is 75.0 mm and the outer diameter is 78.5 mm. The inner separation between the pair is 61.6 mm and the outer separation is 68.6 mm. These are used to provide a magnetic field for the main chamber MOT and part of the field for a magnetic trap. They are wound from a square shaped copper wire. The copper wire has cross sectional dimensions of 3.5 mm by 3.5 mm and has a 1 mm diameter hole at the centre for water cooling. The ratio between the coil separation, s and radius, R is designed to be $R = \sqrt{3}s$. This ratio is shown in Fig. 3.10 by the diagonal line cutting the quadrupole coils. This ratio is specifically chosen since it satisfies the anti-Helmholtz condition which optimises the uniformity of the gradient of the field [78]. The simulated field for the quadrupole coils is shown in Fig. 3.11. The gradient at the centre is 0.31 G cm^{-1} A^{-1}.

Bias Coils

The bias coils are in a dipolar configuration and are necessary to provide a bias field for processes such as degenerate Raman sideband cooling or Fesh-

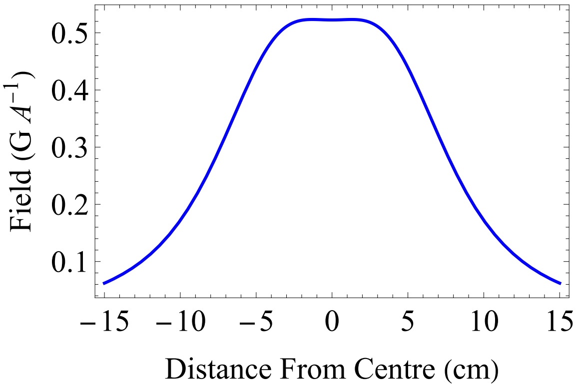

Figure 3.12: Plot of simulated bias fields.

bach resonances. The Bias coils are wound from square copper cabling which has a width of 4.4 mm with a 1.4 mm diameter hole for water cooling. The number of windings is 2×4. The inner diameter is 132.4 mm and the outer diameter is 136.8 mm. The inner separation is 55.6 mm and the outer separation is 66.1 mm. The ratio of separation to diameter has been chosen to satisfy the Helmholtz condition: $R = s$. This minimises the curvature of the field at the centre. The field at the centre is simulated to be 0.51 G A^{-1}. A suitable range of fields we need to work with can be determined by where we expect to find Feshbach resonances. For example, KCs Feshbach resonances suitable for molecule formation can be found in the regions 0 G to 950 G with possible resonances at 146.5 G and 236 G and 935.2 G [42, 61, 79]. The curvature of the bias field is calculated to be 0.002 G $\mathrm{cm}^{-2}\mathrm{A}^{-1}$.

Jump Coils

The jump coils are also in a dipole configuration but are smaller and have less windings (2×2) than the bias coils. This is to ensure the inductance of these coils are lower allowing for faster ramping times. This necessary so that we can ramp to a specific bound state and 'skip over' other bound states we may have to cross over to obtain the desired state. The jump coils allows us to ramp fast past these unwanted resonances to minimise losses. The coils have an inner diameter of 108.4 mm, and outer diameter of 112.8 mm and an inner and outer separation of 53.6 mm and 57.1 mm respectively. These coils too are designed to satisfy the Helmholtz condition. They have a calculated field at the centre of 0.31 G A^{-1} and an estimated curvature of

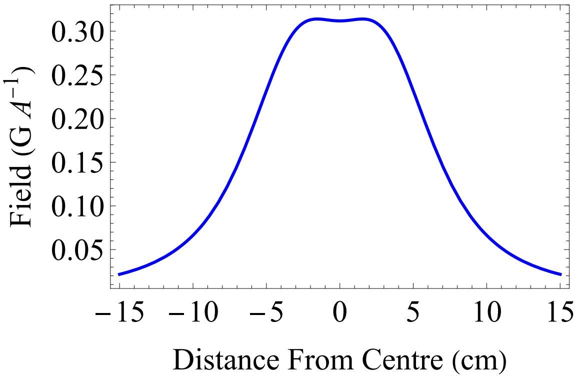

Figure 3.13: Plot of simulated jump fields.

0.002 G cm^{-2}A^{-1}. Figure 3.13. shows the simulated field along the separation axis for the jump coil pair.

K Trap Coils

The K trap coils are designed to complement the quadrupole coils in creating a magnetic trap for K and the other species. A magnetic trap is a necessary to cool K further before loading into an optical dipole trap, whether by sympathetic cooling with another species or by direct forced evaporate cooling.

Previous work has managed to sympathetically cool a sample of ^{41}K with ^{87}Rb in a magnetic trap at a gradient of 155 G cm^{-1} [80]. The maximum current provided by our power supply is 400 A which can only allow the quadrupole coils to reach a magnetic field of 120 G cm^{-1}. Although it is only 35 G cm^{-1} lower than the target, the atom number density in a magnetic trap scales as the cube of the gradient of the field. Reaching 155 G cm^{-1} would improve the cooling efficiency. It was therefore necessary to construct new coils to boost the gradient for a magnetic trap stage.

At the time of the construction of these new coils the chamber had already been fully assembled so we needed to construct around what was already in place. Figure 3.14 shows a cross sectional cut through the centre of the chamber, at all angles around the centre. The background is a density plot which shows the contributions to the gradient from a coil wound at that radius and separation the pair. The black regions show obstructions where a coil cannot be positioned. Unfortunately it was impossible to place them on the line which satisfied the anti-Helmholtz condition.

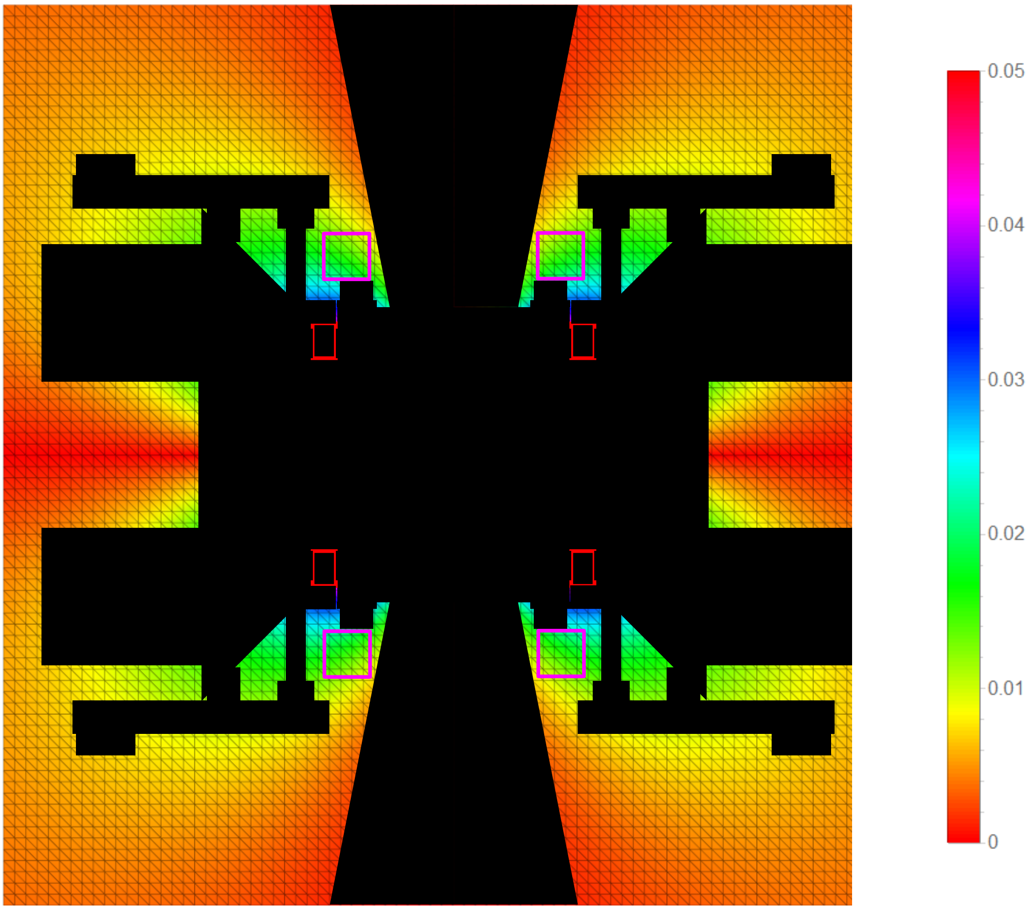

Figure 3.14: Density plot of cross section of magnetic field gradient contribution from coil located at that point on the plot. The units of field contribution are in G cm^{-1} A^{-1}. The plot has been divided into 3.5×3.5 mm^2 squares where each square is representative of a coil winding. The blackened out region are blocked regions and windings cannot be placed here because of obstructions from the main chamber, other coils or beams. The magenta squares show the locations of the newly constructed coils and the red squares show the locations of the current quadrupole coils.

We had to aim for a coil which would give us a reasonable contribution to the field but limit the power consumed by the coils. The magenta squares show the location chosen. The K-trap coils are 4×4. They have an inner diameter of the coils are 55.5 mm and an outer diameter of 66.0 mm. The inner separation is 101.1 mm and the outer separation is 111.6 mm. A customised nylon mount was designed and constructed and the K trap coils are glued to it. The mount allows us to bring the coil down from above and rest the

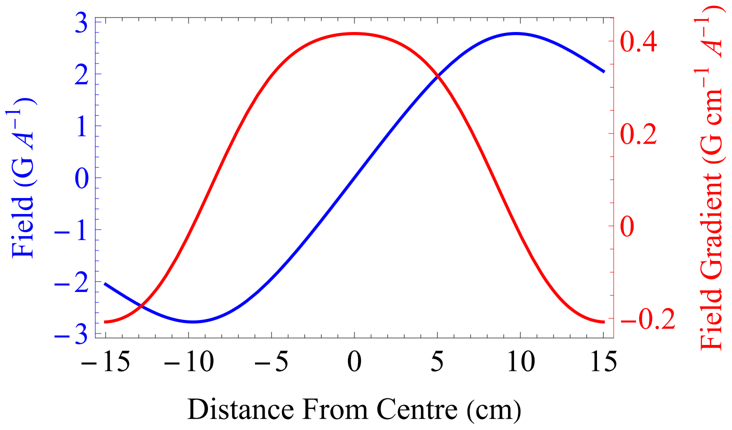

Figure 3.15: Simulated plot of the quadrupole fields (blue, left axis) and the field gradient (red, right axis) through the central axis along the direction of separation.

coils on the vertical viewport bolt heads. Two long threaded rods at opposite ends of the mount screw into the main coil TUFNOL mount. Two hex bolts are then used to secure the coils in place.

The contribution to the field gradient at the centre is 0.42 G cm^{-1} A^{-1}. Figure 3.15 shows the field along the vertical axis of the coils.

In order to reach the target gradient of 155 G cm^{-1}, we will drive the quadrupole coils at their maximum current - tested to be 380 A - since these coils give a large contribution. The, K-trap coils on a second power supply, can then be driven at 88.5 A to supply the remaining gradient. The total power drawn from the new coils is estimated to be 2.2 kW.

Shims

The remaining coils unaccounted for on the main chamber are the shim coils. Figure 3.17 shows the field strength as a function of the displacement along the separation axis and table 3.4 summarises the shim parameters.

The vertical shim coils are circular. They have 6 × 6 windings and are wound from 1 mm thick circular copper wire. They have an interior diameter of 326.6 mm and an exterior diameter of 332.1 mm. They also have an

	Quadrupole	Bias	Jump	K Trap
Windings	2 × 3	2 × 4	2 × 2	4 × 4
Inner Diameter (mm)	75.0	132.4	108.4	55.5
Outer Diameter (mm)	78.5	136.8	112.8	66.0
Inner Separation	61.6	55.6	53.6	101.1
Outer Separation	68.6	66.1	57.1	111.6
Field at Centre (G A^{-1})	-	0.52	0.31	-
Field at Centre (G cm^{-1} A^{-1})	0.31	-	-	0.42
Curvature at Centre (G cm^{-2} A^{-1})	-	0.002	0.004	-

Table 3.3: Summary of coils in the main coil assembly, does not include the shims.

	Vertical Shims	Horizontal Shims
Windings	6 × 6	8 × 10
Inner Diameter or Length and Width (mm)	326.6	176.5 and 99.5
Outer Diameter or Length/Width (mm)	332.1	189.2 and 109.4
Inner Separation (mm)	169.8	310.9
Outer Separation (mm)	175.3	317.5
Field At Centre (G A^{-1})	2.0	0.94

Table 3.4: Table summarising the characteristics of the main chamber shim coils.

interior separation of 169.8 mm and an exterior separation of 175.3 mm. They produce a field across the centre of the arrangement of 2.0 G A^{-1}.

The horizontal shims consist of two rectangular pairs perpendicular to each other. Each pair has 8 × 10 windings and are wound from the same cable as the vertical shims. The interior width of a single coil is 99.5 mm, the exterior width is 109.4 mm, the interior length is 176.5 mm and the exterior length is 189.2 mm. The interior separation of the coils is 310.9 mm and the exterior separation is 317.5 mm. Each pair in the dipole configuration can produce a field of 0.94 G A $^{-1}$.

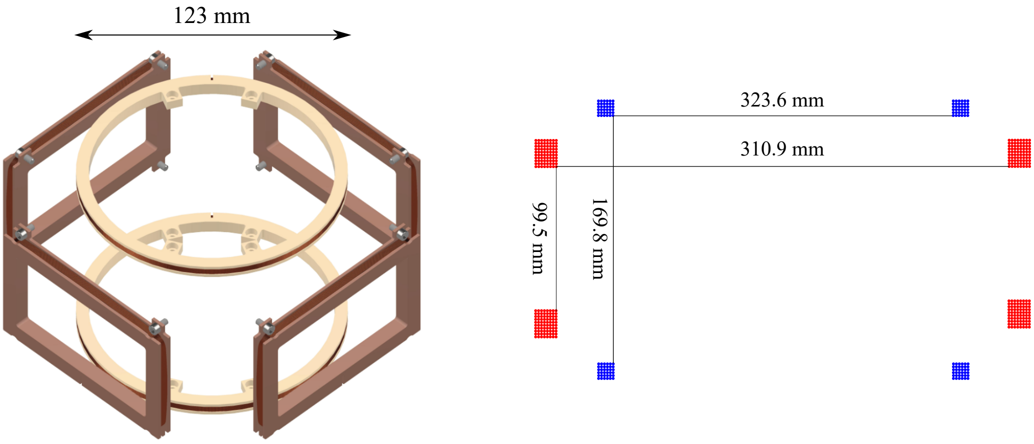

Figure 3.16: Diagram of shim coils. Left is an inventor drawing of the coils. Right is a diagram indicating the coil positioning on a 2D-plane cut through the centre of one of the horizontal shim coils. Shown here is the interior width of the rectangular coils, the interior length of the coils (distance in and out of page) is 176.5 mm. The red dots show the horizontal shims and the blue dots show the vertical shims. The scale on the left drawing shows the diameter of the vertical shims.

3.5 Science Cell

After the atoms have been cooled they will be optically transported from the main chamber to the science cell, using a moving standing wave [77, 81], for the final stage of the experiment. Here, the imaging and molecule formation will take place. We have already discussed the electrodes in chapter 2. A detailed discussion of the science cell magnetic coils and microscope is beyond the scope of this thesis but will be expected to be discussed in subsequent theses. In this section we will only summarise the science cell and associated equipment and discuss the glass cell itself.

Figure 3.18 shows a drawing of the science cell section. The top image shows a top down view of the science cell and the bottom image shows a side on view of the science cell where the cross section is cut at the half-way point.

The science cell is positioned after an ion pump that keeps the vacuum in the science cell well below 10^{-10} mbar. The glass cell is rectangular with dimensions 60 mm × 25 mm × 25 mm. The current arrangement of four electrodes run concentric and parallel to the long side of the science cell and are held in place by macor insulators.

The science cell is positioned at the centre of an arrangement of circular coils

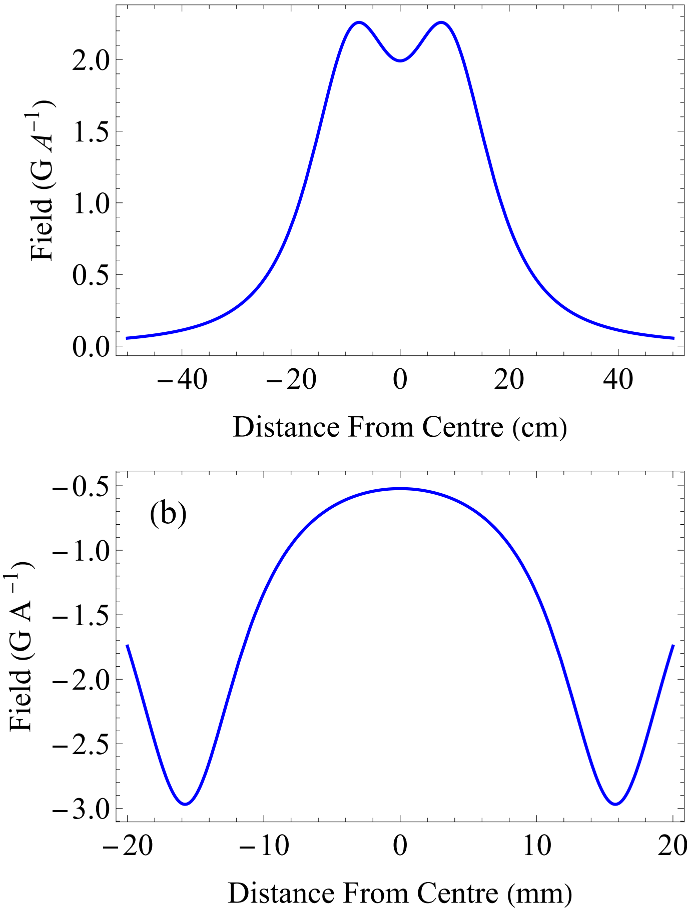

Figure 3.17: Plot of the field of the shim coils. (a) Vertical shims along central axis of separation. (b) One pair of horizontal shims along axis of separation. 0 cm is defined as the centre of the coil pair.

as shown. These coils comprise of a pair of jump coils, quadrupole coils and a pair of bias coils. The quadrupole coils provide the field gradient needed for selecting a layer from the lattice.

The microscope objective sits directly below the science cell. When the high resolution imaging light is incident on a filled lattice the objective will gather the fluorescence produced. This will be sent to a camera for imaging. The microscope objective rests on a stage which is itself is mounted onto piezo actuators. These piezos allow for fine adjustment of both the position of the microscope objective and the angle.

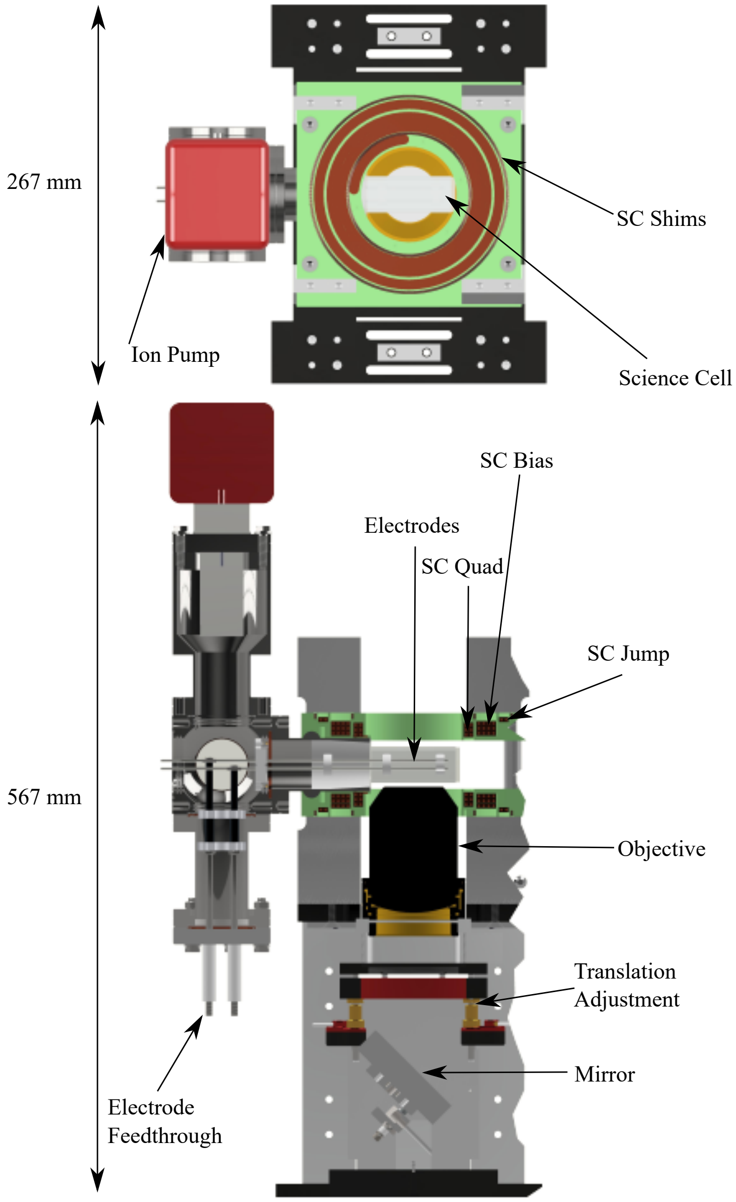

Figure 3.18: Top: Science cell section from top down view. Bottom: Science cell section from side on. The bottom view is a cross sectional cut through the centre (except the objective).

Chapter 4

Spectroscopy on Potassium

4.1 Introduction

Experiments employing laser cooling require lasers that are frequency stabilised to better than the linewidth of the transition used for cooling. For alkali-metal atoms this corresponds to a frequency stability of $\lesssim 1$ MHz. One method of achieving this is with a spectroscopy technique to obtain a sub-Doppler error signal from an atomic hyperfine structure. The error signal is then used as feedback to correct any frequency deviations of the laser. Some of the most common methods are dithering the current to extract the derivative of the saturated absorption signal [82–84], frequency modulation spectroscopy [85, 86], dichroic atomic vapour laser locking (DAVLL) [87–90], far off resonance locking with the Faraday effect [91, 92], polarization spectroscopy [93–95] and modulation transfer spectroscopy (MTS) [96, 97].

MTS is a pump-probe spectroscopy technique that works by modulating the pump beam with an electro-optical modulator (EOM) to produce sideband components and carrier components. When the pump beam is overlapped with the probe beam in a vapour cell, and near resonance with the vapour, a four wave mixing process tranfers the sidebands from the pump to the probe. The beating between the sidebands and the probe carrier can then be detected by a fast photodiode which produces the MTS signal. MTS has two key advantages. Firstly, MTS generates a dispersive signal on a zero background; the zero crossing of which occurs when the laser is exactly on resonance with the associated transition. Secondly, the MTS signal is dominated by cycling transitions which can be useful in cases where the hyperfine structure is too narrow to resolve with other spectroscopic techniques such as the $S_{1/2} \rightarrow P_{3/2}$ transition in bosonic potassium [98]. This makes it an effective tool for laser frequency stabilisation.

A considerable body of theoretical and experimental work has been published on MTS, for example see [96–107]. There has already been a comprehensive study on the D_2 lines of potassium [98]. However, to our knowledge, very little work has been published on the D_1 lines of potassium either in theory or experiment; an MTS spectrum has been reported but in a wider study of simultaneously locking multiple lasers to a single cell [108].

The small hyperfine splitting in the $4P_{3/2}$ state of bosonic potassium makes it difficult to resolve the individual hyperfine components of the D_2 transition spectroscopically and has a detrimental impact on the efficiency of laser cooling [109]. In contrast the hyperfine components of the D_1 transition are resolvable due to the simpler structure and slightly larger splitting. This transition has found important applications for gray molasses cooling [110, 111] and degenerate Raman sideband cooling [112] and is useful for efficiently spin-polarizing a sample of potassium atoms.

The bosonic isotopes of potassium also have the interesting feature that the ground-state hyperfine splitting is smaller than the Doppler width of the D_1 and D_2 transitions in a room-temperature vapour. This leads to the existence of ground-state crossover resonances in pump-probe spectroscopy schemes. These crossovers are something that are notably absent in the D line spectra of rubidium and caesium [89, 113]. Similar ground-state crossover resonances have been previously observed in the D_2 transition of Lithium [104]. The presence of ground-state crossover features in potassium motivates a comparison between the MTS spectrum of the D_1 and D_2 lines as well as a comparison against a species whose hyperfine levels are farther apart such as rubidium. We can seek to establish their suitability as candidates for frequency stabilisation.

In this work we present a detailed study of MTS of the D_1 transition of potassium, comparing our results with MTS of the D_2 line. To elucidate the role of the ground-state crossover, we contrast our results with spectra obtained for rubidium. We also present spectra for different polarisation configurations, showing that the configuration where the beams have linear and perpendicular polarisation offers the strongest signal for locking.

Throughout we compare our experimental results with the predictions from a theoretical model based upon the solutions to the time dependent optical Bloch equations without the use of any phenomenological constants. We find the calculations predict a large dispersive signal for the crossover features.

This chapter is outlined as follows: first we will give a summary of the theory and generation of the dispersive signals used in MTS. We will then give an overview of the experimental setup. We will then summarise the results of the MTS from the experiment and compare it against the predicted theory.

4.2 MTS Theory

The section will only give a brief overview of the theory concerning the MTS lineshapes. A more comprehensive discussion of theory can be found in [99].

In MTS a laser beam is split into a pump and probe path. The probe is sent directly to a cell containing a vapour of the atomic species. The pump is passed to an EOM which phase-modulates the laser's electric field adding sidebands to the laser at integer multiples of the EOM modulation frequency. The modulated field can subsequently be described by [89]:

$$E = E_0 \left[\sum_{n=0}^{\infty} J_n(\delta) \sin\left[(\omega_c + n\omega_m)t\right] + \sum_{n=0}^{\infty} (-1)^n J_n(\delta) \sin\left[(\omega_c - n\omega_m)t\right] \right], \tag{4.1}$$

where E_0 is the amplitude of the electric field, J_n is the n^{th} order Bessel function, ω_c is the carrier frequency and ω_m is the modulation frequency. δ is the modulation index. The modulation index is chosen such that we are in a regime where $J_m(\delta) << J_1(\delta)$, where $m > 1$, This means the electric field only has a carrier frequency and a pair of well defined sidebands. Equation 4.1 can be simplified to:

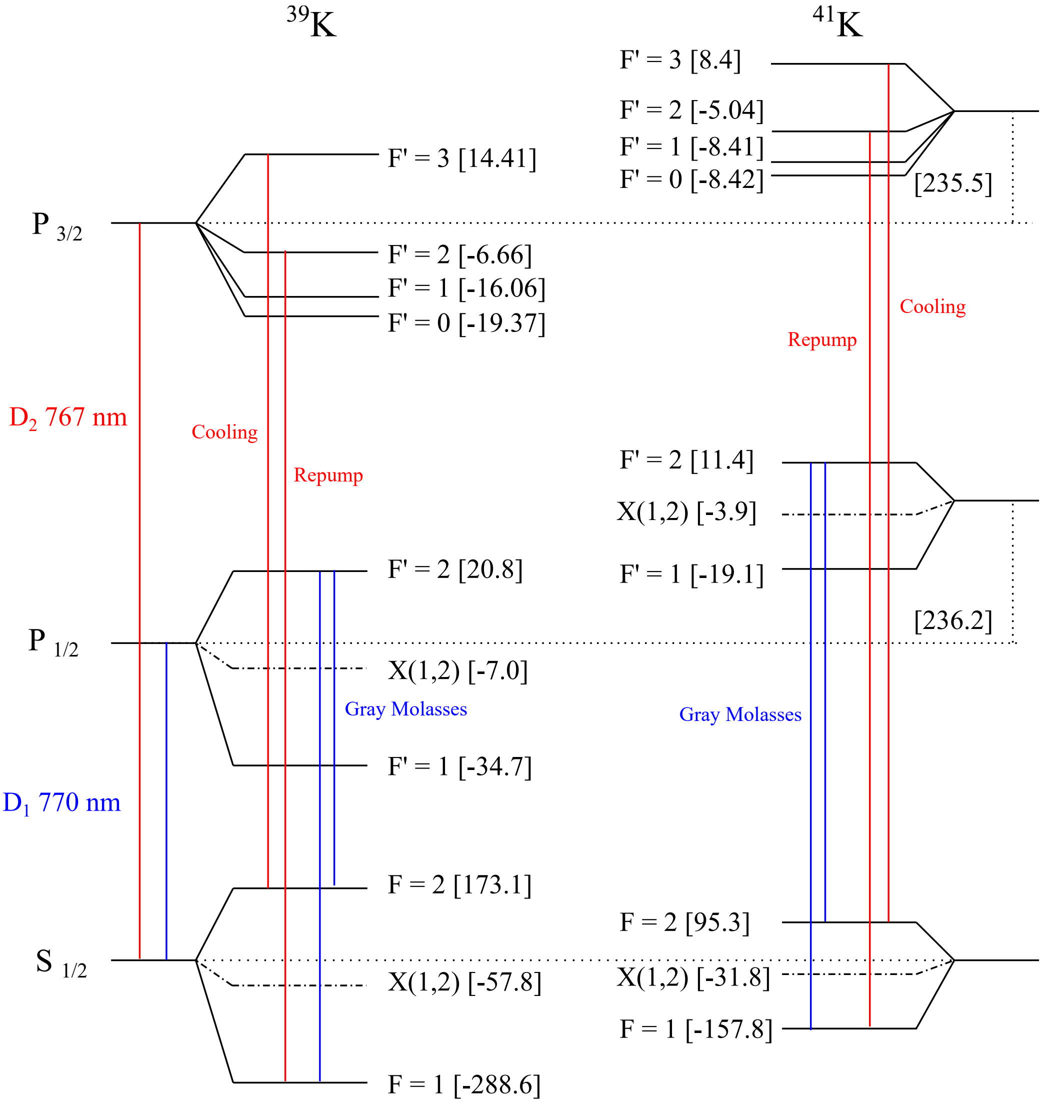

Figure 4.1: The hyperfine structure of K relevant to the D_1 and D_2 transitions, The transitions relevant to cooling are also labelled. Levels are labelled by the quantum number F for the total angular momentum of the state and hyperfine shifts are given in MHz using the values from [114]. The horizontal dot-dashed lines show the positions of crossovers for the $S_{1/2}$ and $P_{1/2}$ manifolds.

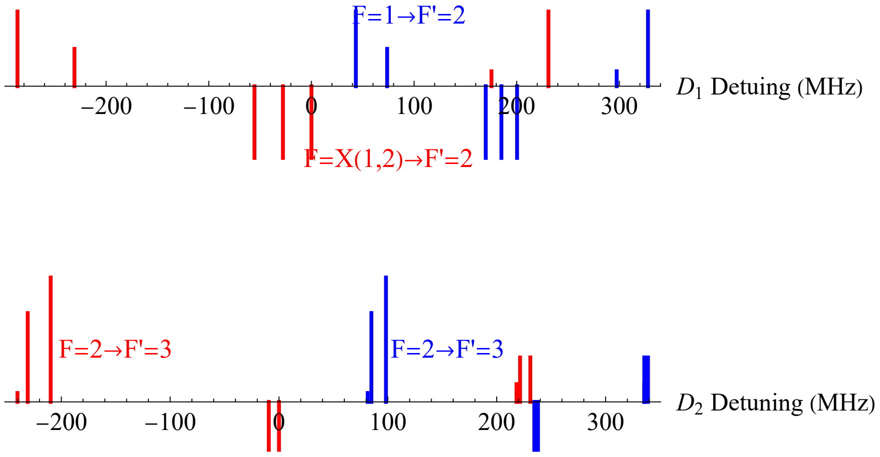

Figure 4.2: The line spectra of the bosonic isotopes of K, lines above the axis correspond to normal transitions and have heights reflecting the relative oscillator strengths. Lines below the axis correspond to crossover transitions. Ground state crossovers are indicated by circles at the bottom of the line. For clarity, excited-state crossover transitions have been omitted for the D_2 transition. For both spectra, zero detuning corresponds to the $X(1,2) \rightarrow F' = 2$ transition in ^{39}K. Note, in the experiment the spectra will be weighted by the natural abundances of the isotopes shown in the figure.

$$E = E_0 \left[J_0(\delta) \sin\left[\omega_c t\right] + J_1(\delta) \sin\left[(\omega_c + \omega_m)t\right] - J_1(\delta) \sin\left[(\omega_c - \omega_m)t\right]\right]. \tag{4.2}$$

The modulated pump is overlapped with the probe inside the vapour cell. As the laser is scanned across a transition or crossover a four wave mixing process transfers the modulation from the pump to the probe creating a new sideband on the probe [115]. A fast photodiode is positioned to record the probe signal. The fast photodiode directly measures the beating between the probe carrier and the probe sideband. This probe signal varies in accordance to the equation:

$$S(\omega_m) = \frac{C_m}{\sqrt{\Gamma^2 + \omega_m^2}} J_0(\delta) J_1(\delta) \tag{4.3}$$

$$\times \left([L_1 - L_{-1/2} + L_{1/2} - L_1] \cos(\omega_m t + \phi)\right. \tag{4.4}$$

$$\left. + [D_1 - D_{-1/2} - D_{1/2} + D_1] \sin(\omega_m t + \phi)\right), \tag{4.5}$$

where Γ is the natural linewidth of the species, ϕ is the phase of the E-field and C_m is an amplitude coefficient that is dependent on other experimental parameters (i.e. gain of the low-pass filter). The other terms are given by:

$$L_n = \frac{\Gamma^2}{\Gamma^2 + (\Delta - n\omega_m)^2}, \tag{4.6}$$

and

$$D_n = \frac{\Gamma(\Delta - n\omega_m)}{\Gamma^2 + (\Delta - n\omega_m)^2}, \tag{4.7}$$

where Δ is the detuning. From Eq. 4.5 we can see that by applying a lock in technique it is possible to extract either an in-phase component:

$$L_1 - L_{-1/2} + L_{1/2} - L_1, \tag{4.8}$$

or a quadrature component:

$$D_1 - D_{-1/2} - D_{1/2} + D_1, \tag{4.9}$$

which gives us the signal for frequency stabilisation.

This is a very brief summary of the theory of MTS. The simulated lineshapes used in this chapter were calculated by Professor Heung-Ryoul Noh by solving the associated master equation for the system. A more detailed theoretical treatment can be found in a variety of his works such as: [99, 100, 116, 117]. The theory and results used in this chapter specifically for K will be described in detail in our planned publication [60].

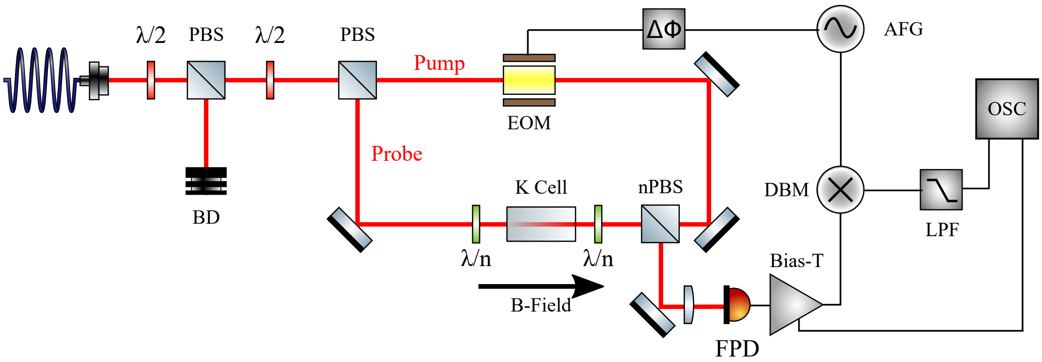

Figure 4.3: Experimental setup for modulation transfer spectroscopy (MTS). The red solid line indicates the laser beam path. Two polarizing beam splitters (PBS) and waveplates are used to determine the total power and ratio between the pump and probe beams. The waveplates labelled λ/n are exchanged depending on the polarization configuration: $n = 2$ for linear polarization configurations or $n = 4$ for circular polarization configurations. Laser light is output from a fiber. The transmitted probe beam is detected on a fast photodiode (FPD). The resulting MTS signal is extracted using a double-balanced mixer (DBM) and low-pass filter (LPF). nPBS: 50:50 non-polarizing beam splitter. BD: Beam dump. EOM: Electro-Optical modulator. AFG: Arbitrary function generator. OSC: Oscilloscope.

4.3 Experiment

The experimental setup is shown in Fig. 4.3. The laser source is an external cavity diode laser (Toptica DL Pro). We couple the laser light through a single mode polarization maintaining fiber such that the subsequent output beam profile is Gaussian. A pair of polarizing beam splitters (PBS) in combination with a pair of $\lambda/2$ waveplates are used to control the total power of laser light delivered to the spectroscopy setup and the ratio of power between the pump and probe beams. The probe light is passed directly to the potassium vapor cell. The cell is housed inside a brass block with a pair of heating elements attached. The cell temperature is raised to 99(2)°C where we expect a vapor pressure of 3.5×10^{-5} mbar. The probe and pump beams are collimated such that their $1/e^2$ diameters at the centre of the cell are 2.06(2) mm and 1.96(5) mm, respectively.

The pump light is passed through a homebuilt EOM. The EOM uses a $LiTaO_3$ crystal electrically contacted to a pair of brass capacitor plates. The addition of an inductor creates a simple LCR circuit that resonantly enhances the voltage across the crystal. The resonance frequency of the EOM is at 6.054(5) MHz. We always drive the EOM on resonance at its maximum voltage, producing sidebands with 15.0(1.0)% of the total pump intensity. More details of the EOM can be found in previous work [89].

We investigate different combinations of laser polarization. To maintain a well defined quantisation axis we apply a weak magnetic field with a set of rectangular coils which are concentric with the cell. The coils provide a 1.5 G magnetic field at the centre of the cell in a direction along the beam propagation axis. By switching around the waveplates indicated in Fig. 4.3 we are able to study four different polarization configurations of the laser light through the cell: circular polarization where the pump and probe drive opposite transitions ($\sigma^+\sigma^-$), circular polarization where the pump and probe drive the same transitions ($\sigma^+\sigma^+$), linear polarization where the pump and probe are perpendicular (lin$\perp$lin) and linear polarization where the pump and probe are parallel (lin $\parallel$ lin).

A simple set of electronics apply a phase lock-in technique to demodulate the MTS signal. The homebuilt fast photodiode detects the beat signal between the modulated probe carrier and the sidebands. This signal is passed through a bias-tee [Mini-Circuits model: ZFBT-4R2GW] which filters out the DC component of the signal corresponding to the standard saturated absorption profile and sends it to a secondary channel of the oscilloscope. The modulated component is passed to the double balanced mixer (DBM) [Mini-Circuits model: ZAD-1H+] which multiplies the signal with the reference signal provided by the arbitrary function generator (AFG) [Tekronix model: AFG 3102]. The AFG has two outputs. One output is used to drive the EOM and the second output is used as a local oscillator which acts as our reference for the demodulation. The relative phase of the two outputs can be set using the AFG, allowing us to fully characterise the phase parameter. The demodulated signal can then be sent to the oscilloscope for data acquisition or to feedback circuitry to stabilize the laser frequency.

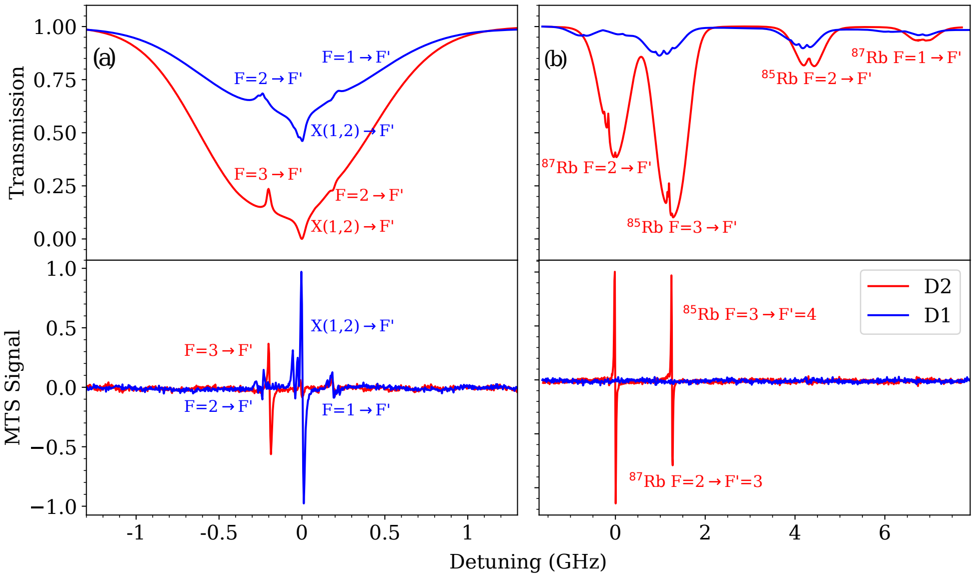

Figure 4.4: (a) Absorption signal as filtered by bias-T (top) and MTS signal (bottom) for potassium in the $\sigma^+\sigma^+$ configuration. The cell length is 2 cm and heated to 99 °C. Data were taken with probe and pump beam intensities of 78.0(1.5) mW cm^{-2} and 86(5) mW cm^{-2} respectively. (b) Signal for rubidium in the $\sigma^+\sigma^+$ configuration. The cell length is 4 cm and at 20 °C. Data were taken with probe and pump beam intensities of 90(1.7) mW cm^{-2} and 53(2) mW cm^{-2} respectively. The red lines show the D$_2$ transition and the blue lines show the D$_1$ transition. For potassium, zero detuning corresponds to the $X(1,2) \rightarrow F' = 2$ transition in ^{39}K for the D$_1$ trace and the $X(1,2) \rightarrow F' = 3$ transition for the D$_2$ trace. For rubidium, zero detuning corresponds to the $F = 2 \rightarrow F' = 2$ in ^{87}Rb for the D$_1$ trace and the $F = 2 \rightarrow F' = 3$ transition for the D$_2$ trace. The vertical axes for both (a) and (b) share the same ticks.

4.4 Results

4.4.1 Comparison with D$_2$ and rubidium MTS

To better illustrate the role of the crossovers and cycling transitions in MTS we have recorded an MTS trace for the D$_2$ and D$_1$ transitions of both potassium and rubidium for a brief comparative study. The species ^{87}Rb is suitable for a comparison against potassium since they both have the same hyperfine quantum numbers.

Figure 4.4(a) shows the absorption spectroscopy and MTS signals for the D$_1$

and D_2 transitions in potassium. The vertical axis for the MTS signals are normalised with respect to the ^{39}K D_1 $X(1,2) \rightarrow F = 2$ feature. These data were taken using the $\sigma^+\sigma^+$ configuration with a probe probe beam intensity and pump beam intensity of 78.0(1.5) mW cm^{-2} and 86(5) mW cm^{-2} respectively. All intensities quoted for the experiment are the peak intensity where the beam is assumed to be Gaussian. We note from the absorption profile on Fig. 4.4(a) that all of the hyperfine transitions lie within the same Doppler profile. The D_2 transition shows the standard MTS signal, with a single strong feature resulting from the $F = 2 \rightarrow F' = 3$ closed transition on a flat zero background. This feature is ideal for laser frequency stabilization on the K D_2 transition [98]. For the D_1 transition we observe several strong features in the MTS signal, despite the absence of a closed transition. We have a strong resonance at the ground-state crossover. The signal is dominated by the ground state crossover transition, $X(1,2) \rightarrow F' = 2$, providing a feature suitable for laser frequency stabilization. We note that the $X(1,2)$ crossover features involve both ground state energy levels such that the pump beam and probe beam can simultaneously interact with atoms in both states preventing hyperfine optical pumping, effectively 'closing' the transition. These strong ground-state crossovers that have also been reported in the D_2 MTS of lithium [104]. In contrast, the crossover signals for the D_2 transition are weak, as reported previously [98]. For the $\sigma^+\sigma^+$ configuration the existence of a cycling transition may be detrimental; optical pumping on the cycling transition will populate the $F = 2, m_f = 2$ ground state, but on the crossover at least one of the pump or probe beams will be interacting with the depopulated $F = 1$ state. This will restrict transfer of the sidebands from the pump to the probe, weakening the signal. For the D_1 at least, these strong resonances in the absence of a cycling transition merit further study.

Figure 4.4(b) shows the absorption spectroscopy and MTS signals for the D_1 and D_2 transitions in rubidium. These data were taken taken using the $\sigma^+\sigma^+$ configuration with a probe probe beam intensity and pump beam intensity of 90.0(1.7) mW cm^{-2} and 53(2) mW cm^{-2} respectively. Again the MTS signal for the D2 transition is dominated by the cycling transitions. However, in contrast to K, the MTS signal on the D_1 transitions for Rb does not show any measurable features. This can be attributed to the lack of ground state

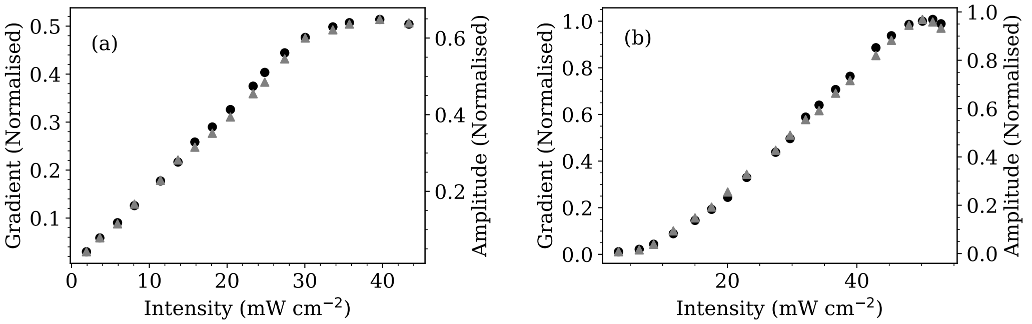

Figure 4.5: Gradient (black circles) and amplitude (grey triangles) of the $X(1,2) \rightarrow F' = 2$ ^{39}K transition as a function of the beam intensity in the lin ∥ lin configuration. Results are shown for (a) the pump beam optimised at a constant probe of 23.7(4) mW cm^{-2} and (b) the probe beam optimised with a constant pump of 16.4(1) mW cm^{-2}.

crossover transitions; in Rb the ground state hyperfine splitting (greater than 3 GHz for both isotopes) is significantly greater than the Doppler broadening on the order 500MHz in a room temperature cell, as evident in the absorption spectrum.

4.4.2 Optimisation and comparison against theory

We use the strongest feature resulting from the $X(1,2) \rightarrow F' = 2$ transition to optimise the parameters of the MTS setup for the D1 transition in K. Figure 4.5 shows the gradients and amplitudes of the signal as a function of the intensities of both the (a) pump and (b) probe beams, with the intensity of the other beam held constant. We optimise the intensities to obtain the steepest gradient for the lin ∥ lin configuration which is shown on Fig. 4.6(a). The pump intensity was optimised first with a constant probe intensity of 47.4(8) mW cm^{-2}; then the probe intensity was optimised with a constant pump intensity of 32.8(2) mW cm^{-2} (chosen arbitrarily). The optimised intensities were found to be 36(3) mW cm^{-2}, and 59.5(1.1) mW cm^{-2} for the pump and probe beams, respectively. Note the saturation intensity is 1.75 mW cm^{-2} [114].

Figure 4.6(a) shows, as an example, the experimental (solid lines) and theoretically predicted (dashed lines) MTS signal for the lin ∥ lin configuration for phase steps 30° apart. Note the phase is defined as the difference in phase between the photodiode signal and the reference signal at the double

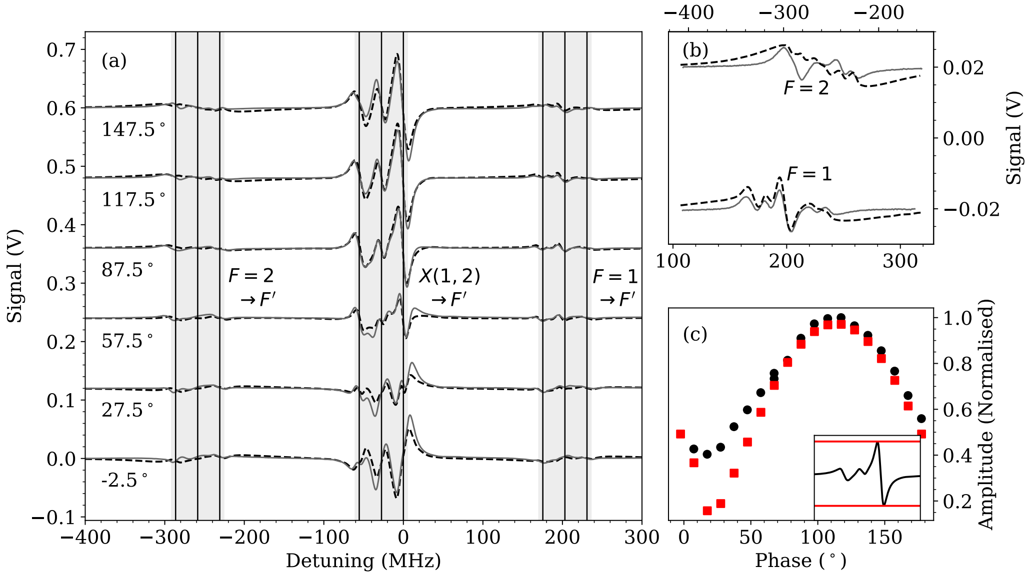

Figure 4.6: (a) MTS trace for the lin || lin configuration at different phases. The data are taken at 25(2)mW cm^{-2}, 5.5(4)mW cm^{-2} and 59.5(1.1)mW cm^{-2} for the pump carrier, pump sidebands and probe respectively. The grey solid trace is the experimental data and the black dashed trace is the fitted simulation. An arbitrary vertical offset is added between traces to separate the signals recorded at different phases. Highlighted regions indicate areas where we see transitions and have their ground-state shown next to them. Vertical lines show the transition locations for ^{39}K. Numbers on the left of each phase show the phase ϕ. (b) MTS signal zoomed into the $F = 2 \rightarrow F'$ (top) and $F = 1 \rightarrow F'$ (bottom) transitions at 117.5 °. A vertical offset has been added to separate the two transitions. (c) The amplitude of the $X(1, 2) \rightarrow F' = 2$ feature as a function of the phase for experimental (black circles) and theoretical predictions (red squares).

balanced mixer after having corrected for the arbitrary experimental offset. There are three distinct regions highlighted corresponding to features arising from the $F = 1$ ground state (right), the $X(1, 2)$ crossover (center) and the $F = 2$ ground state (left). It is also worth noting that the rightmost region also has a significant contribution from the ^{41}K $X(1, 2)$ crossovers as well, see Fig. 4.1, but the other features are purely from ^{39}K. Figure 4.6(b) are zoomed into the $F = 2 \rightarrow F'$ (top) and $F = 1 \rightarrow F'$ (bottom) ground-state transitions respectively.

The peak-to-peak amplitude for the $X(1, 2) \rightarrow F' = 2$ feature as a function of the phase are shown in Fig. 4.6(c). Traces of different phase are taken by introducing a phase delay using the AFG and are taken in 10° steps. This additionally allows us to measure the in-phase, where the phase is 0° and

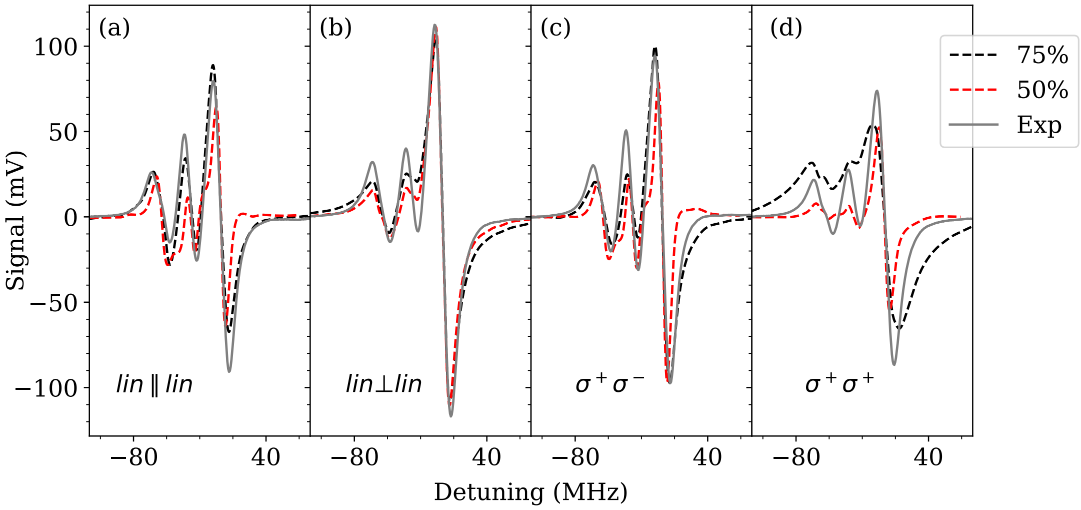

Figure 4.7: MTS signal for each polarization configuration. The parameters optimised for the lin $\parallel$ lin configuration are the same parameters used across all configurations. The black lines indicate the best fit theory for simulations at 75% intensities and the gray solid lines show the experimental data. We have also included, for comparison, the best fit theory data for a simulation at 50% of the quoted intensities: the red dashed lines. The polarization configurations are (a) lin $\parallel$ lin, (b) lin $\perp$ lin, (c) $\sigma^+\sigma^-$ and (d) $\sigma^+\sigma^+$. The data are shown only for the central feature.

quadrature, where the phase is 90°, components. We note that the optimal peak-to-peak amplitude is not obtained in the full quadrature or or in-phase scenarios but rather at a relative phase of 112.3°.

The simulation assumes a flat-top intensity distribution rather than the Gaussian profile used in the experiment. To partially compensate for this, intensities used in the simulation are set to 75% of the quoted peak experimental intensities. The width of this top hat function is equal to the $1/e^2$ diameter of the beam. Two contributions are calculated: an in-phase component $I(\delta)$ and a quadrature component $Q(\delta)$, where δ is the detuning. These are superimposed to obtain the signal, S, as a function of the relative phase $\tilde{\phi}$,

$$S[\delta,\tilde{\phi}] = A(I(\delta)\cos\tilde{\phi} + Q(\delta)\sin\tilde{\phi}), \tag{4.10}$$

where A an arbitrary amplitude factor to match the theory to the experimental measurements. Experimentally there are two contributions to $\tilde{\phi}$

tilde; the relative phase ϕ set by the AFG and an arbitrary phase offset ϕ_0 arising from cable delays. Thus to compare the theory and experiment we use $\tilde{\phi} = \phi - \phi_0$, and adjust the value of ϕ_0 to find the best agreement. In practice, traces for all measured phases of a given polarization are fitted simultaneously to Eq. (4.10) to extract the parameters A and ϕ_0.

Figure 4.6 shows the comparison between theory and experiment for the lin $\|$ lin configuration. MTS signals are shown for steps of 30° in the phase $\tilde{\phi}$. We can see that there is generally good agreement. For phases where the $X(1,2) \rightarrow F'$ features are maximised, the relative peak heights and signal widths agree particularly well. Further evidence is shown by (c) which compares the experimental amplitude against the predicted amplitude for the dominant feature over phases from 0° to 180°. We certainly see in the region closest to the maximum that we get better agreement. For the weaker $F = 1 \rightarrow F'$ and $F = 2 \rightarrow F'$ transitions shown in (b) and there is reasonable agreement, although there are differences in some cases.

4.4.3 Different polarisation configurations

A simple reconfiguration of the waveplates in Fig. 4.3 allows us to look at the MTS signal for other polarization configurations. The results are shown in Fig. 4.7 for the signals arising from $X(1,2) \rightarrow F'$ transitions. The traces were taken with $\tilde{\phi} = 117.5$ °, close to the optimum phase of 112.3 ° degrees from Fig. 4(b). The laser parameters were the same as the optimum values found for the lin $\|$ lin configuration. The data shown here are the ground crossover (central) resonances only. In the lin $\perp$ lin case we observe a substantial increase in the amplitude of the $X(1,2) \rightarrow F' = 2$ signal and a reduction in the size of the neighbouring features. There is very good agreement between the theory and experiment for all cases except for the $\sigma^+\sigma^+$ configuration. We note that in this case the theory predicts substantially broader features than are observed experimentally. The Rabi frequencies of laser beams in the experiment lie between 2 and 4 Γ. In this region of laser intensities, our assumption of three-photon interactions may be insufficient, in particular for the specific polarisation configuration, and we may need new calculations of higher order interactions in this case. This kind of improvement in the calculation is beyond the scope of this thesis.

Polarization	A (V)	ϕ_0 (°)
lin ∥ lin	1787(7)	110.7(4)
lin ⊥ lin	886(3)	109.4(3)
$\sigma^+\sigma^-$	1576(5)	108.3(3)
$\sigma^+\sigma^+$	1232(8)	103.7(7)

Table 4.1: Fitted parameters for D_1 experimental results against theory. Each of the polarization configurations are listed. A and ϕ_0 are as defined in Eq. (4.10).

Table 4.1 shows the fitted values of A and ϕ_0 for all polarisation configurations. The values of A and ϕ_0 mean little on their own since they are arbitrary and exclusive to our specific setup, however in the context of theory we expect these values to be constant across different polarization configurations. We find good agreement between the different configurations for the phase offset, with all cases falling within a 7 ° range (1.4° if we exclude the $\sigma^+\sigma^+$ data). The amplitude conversion factor, A, does not agree between different configurations. We note that although the lin ∥ lin and the $\sigma^+\sigma^-$ results are are in reasonable agreement; the lin ⊥ lin disagrees by a factor of 2 compared with lin ∥ lin. The theory predicts that the amplitude of the $X(1, 2) \rightarrow F = 2$ transition should be at least a factor of two larger in the linear perpendicular case than in the lin ∥ lin case given the same value of A. However, given that both have different values for A then this is not observed in experiment.

It is of interest to investigate how the theoretical predictions depend upon the intensities used. As mentioned previously, the simulation assumes a uniform flat-top intensity distribution but the beam in the experiment is Gaussian. Figure 4.7 also includes the simulations for intensities at 50% of the experimental peak intensities. Across all polarisation configurations the broadening is substantially less. Although the relative heights of the peaks is somewhat mismatched we note an immediate improvement in the agreement between the theory and experiment for the $\sigma^+\sigma^+$. However, the width of the other features is underestimated by the theory in this case. This is a crucial point. If simulating the beam at the peak intensity quoted, then it would be a uniform beam but with a constant intensity at the peak of the Gaussian beam. This may result in an overestimation of power being delivered to the atoms. Likewise a uniform beam at 50% of the peak intensity (the average beam intensity) may underestimate the power at the atoms. It is evident from the simulations shown in Fig. 4.7 that there is a strong intensity dependence from the theory which may assist in explaining some of discrepancies. We choose, albeit arbitrarily, 75% of the peak beam intensity obtain theory between these two extremes. Regardless, the simulation still produces results in reasonable agreement with the experiment for the lin $\|$ lin, lin$\perp$lin and the $\sigma^+\sigma^-$ cases. We have not used a Gaussian beam in our simulations because it is too computationally expensive. In addition, the difference between experiment and theory might be reduced by using new calculations of higher order interactions. We are currently elaborating the calculation to enhance the accuracy.

4.5 Conclusions

We have presented an experimental study of the modulation transfer spectroscopy of the D_1 transition in K. We have also presented a theoretical model which can be used to predict the MTS which shows generally good agreement with the experimental measurements. We have shown that for the D_1 transition, the MTS signal shows strong features originating from ground state crossover transitions. We have optimized various experimental parameters, including the beam intensities and polarisations, to maximise the $X(1,2) \rightarrow F' = 2$ feature, providing a good reference for laser frequency stabilisation. We expect these results will be of interest to researchers employing the D_1 transition for laser cooling and optical pumping of potassium in quantum gas experiments. These transitions provide a good reference for frequency stabilisation.

Chapter 5

Optimisation of Potassium Laser Cooling

5.1 Introduction

This chapter shall detail the laser cooling strategy adopted to obtain a cold sample of ^{41}K. We have been able to cool a sample of 10^8 atoms to 48 µK. The sample is initially obtained in a MOT in our main chamber before subsequently being cooled using molasses. There are numerous difficulties in the cooling of the bosonic isotopes of K which largely arise due to their narrow hyperfine structure [118].

With ultracold K we can form KCs molecules. As mentioned previously, the advantages of this molecule over RbCs are: a stable fermionic isotope ^{40}K, a greater dipole moment of 1.92 D and the miscibility of K and Cs in their degenerate phases.

5.2 Cooling Strategy

The D_2 lines ^{39}K and ^{41}K both have a natural linewidth of $\Gamma = 6.035(11)$ MHz [119] and a nuclear spin of 3/2. The hyperfine structure of both isotopes is detailed in Fig. 4.1. Immediately one notices that for ^{39}K $P_{3/2}$ hyperfine manifold extends only for 6.5 Γ. For ^{41}K it is just a mere 2.8 Γ.

In other alkali metal atoms such as Rb and Cs the cooling transitions for the MOT and the molasses are far enough apart to be resolved. A high powered beam acting on a cycling transition to deliver the cooling force and a low powered repump beam to recover atoms decaying to the wrong ground state is sufficient to achieve the low temperatures necessary for trapping a cold sample on the order of tens of microkelvin. However, in K if one were to naively use a similar cooling configuration to what would normally be used for Cs or Rb then the unresolved energy structure presents a challenge to cooling.

Specifically, the close proximity of the $F' = 2$ to the $F' = 3$ energy level means a considerable number of atoms will undergo the $F = 2 \rightarrow F' = 2$ transition as opposed to the desired cooling transition $F = 2 \rightarrow F' = 3$. As we are blue detuned to the $F' = 2$ level then this unwanted transition presents a large source of heating. From the $F' = 2$ state atoms can decay to the $F = 1$ ground state. As such, atoms are effectively depumped from the $F = 2$ ground state and exit the cycling transition. Furthermore, having the detuning too close to the cooling transition increases the rate of photon rescattering (another source of heating) but detuning too far excites the wrong transition. All of these effects ultimately have a negative effect on the efficiency of the Doppler and sub-Doppler cooling processes [118].

Initial attempts at sub-Doppler cooling by the Inguscio group [118] involved a two stage molasses. The first stage utilises an intense cooling beam red detuned from the entire $P_{3/2}$ hyperfine manifold complemented with a repump beam of similar magnitude in intensity and also red detuned from the whole hyperfine manifold. The intensity of the cooling beam typically sits in the regime of 20 I_{sat} or greater. The second stage would then see the beams red detuned on the order of 0 - 1 Γ from their respective transitions. The first stage has a large capture velocity but poor cooling force. As such it acts as a pre-cooling stage. The second stage has a strong sub-Doppler component but a weak capture velocity. This strategy took their MOT sample and dropped it to a temperature of roughly 200 µK

Our strategy follows a similar approach to that developed by the Modugno group in 2011 [109, 120]. Being too closely detuned from the $F = 2 \rightarrow F' = 3$

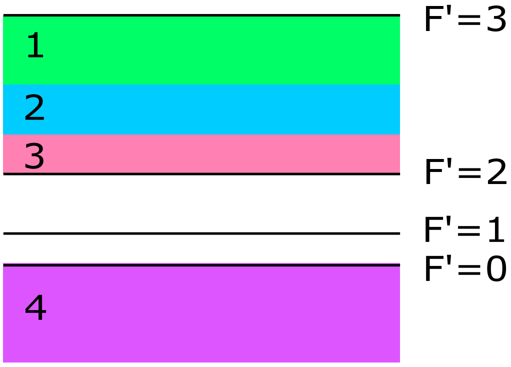

Figure 5.1: Hyperfine structure of ^{41}K illustrating (not to scale) the different cooling regions. Inspiration for this image taken from [109].

transition with a high intensity results in a strong photon re-scattering effect, particularly in dense samples. Too close to the $F = 2 \rightarrow F' = 2$ results in heating from too much interaction with the laser field propagating in the incorrect direction. Key to the cooling strategy involves striking a region in-between these extremes which allows sufficient depumping of the population to the $F = 1$ ground state to reduce the re-scattering rate whilst using a similarly intense repump beam to maintain a proportion of the population in the cycling transition. It should also be noted that due to the intensity of the repump beam then this means that it also provides an additional cooling force. Therefore, which beams we refer to as cooling and repump is a matter of convention more-so than technically correct terms.

Region	Doppler Cooling	Sub-Doppler Cooling
1	Yes	Yes
2	No	Yes
3	No	No
4	Yes	No

Table 5.1: Table showing which forces are present in which region. ‘Yes’ tells us that particular component of the force acts towards the center and vice versa.

On further study one can divide the $P_{3/2}$ hyperfine manifold into several distinct regions depending on the presence of Doppler and sub-Doppler cooling forces. This is illustrated by Fig. 5.1 and the definition of each region is given by table 5.1. It is possible to approximate the region borders by calculating the contribution to the cooling forces for the transition: $F = 2 \rightarrow F' = 3$ and $F = 2 \rightarrow F' = 2$. The Doppler component of the cooling force is given by:

$$f_{23} - f_{22} = \hbar k^2 \Omega^2 \Gamma v \left(-\frac{\delta}{(\delta^2 + \Gamma^2/4)^2} + A \frac{\Delta - \delta}{((\Delta - \delta)^2 + \Gamma^2/4)^2} \right), \qquad (5.1)$$

where Ω is the Rabi frequency of the cooling beam, δ is the detuning from the $F = 2 \rightarrow F' = 3$ transition, Δ is the splitting between the $F' = 2$ and $F' = 3$ energy levels, v is the velocity of the atoms, and A is the ratio of the Clebsh-Gordan coefficients of the associated transitions [120]. The first term is the force originating from the $F = 2 \rightarrow F' = 3$ transition and likewise the second term is the force from the $F = 2 \rightarrow F' = 2$ transition. We can attain sub-Doppler cooling by starting with an intense cooling beam (greater than 5 $\mathrm{I_{sat}}$ per beam) at a detuning of around -0.6 Γ and adiabatically ramping the detuning through region 1 and region 2 whilst ramping down the intensity. This allows us to exploit both the large capture velocity of the Doppler cooling component with the strong force of the sub-Doppler cooling component in region 1 of the hyperfine manifold. In addition, the ramping allows the laser to interact with various velocity classes which adiabatically narrows the velocity distribution.

In [109] there is an initial molasses stage in which the beams are completely red detuned from the $P_{3/2}$ manifold for a small time when the magnetic field is off. In our cooling sequence we skip this initial stage of the molasses and instead have only the adiabatic ramp but still manage to achieve temperatures similar to that in [109]. We skip this stage to shorten the total molasses time. This keeps the molasses time for K consistent with Cs for simultaneous molasses.

5.3 Cooling Laser Setup

Fig 5.2 shows the laser layout used for the initial cooling stages of K atoms and the absorption imaging in the main chamber. The main source of light is provided by a Toptica TA pro. This is a diode laser in the Littrow configuration which seeds a TA. Some of the seed light is picked off and sent to an MTS setup similar to Fig. 4.3 for frequency stabilisation. The TA can output 1 W of laser power at 767 nm. The raw output beam is very elliptical so the TA light is passed through a high power fiber to make the beam circular and Gaussian.

AOM Number	AOM Purpose	Model	Center Frequency (MHz)
1	3D-Cooling	G&H AOMO 3080-122	+/-80
2	3D-Repump ^{39}K	G&H AOMO 3110-120	+120
3	3D-Repump ^{41}K	G&H AOMO 3200-124	+200
4	2D-Repump ^{41}K	G&H AOMO 3200-124	+200
5	2D-Repump ^{39}K	G&H AOMO 3110-120	+120
6	2D-Cooling	G&H AOMO 3080-120	+/-80
7	Spectroscopy	G&H AOMO 3080-120	-80

Table 5.2: Table outlining the purpose of AOMs shown in Fig. 5.2. 'G&H' refers to Gooch and Housego. AOM centre frequencies are the single pass frequencies.

After this fiber we have about 550 mW of light for use in cooling. The beam is passed onto a path of six AOMs, of which four are currently active. We use these AOMs to control both the detuning and the powers of the cooling and repump beams in order to optimise the potassium cooling sequence. The power is distributed using a combination of $\lambda/2$ waveplates and PBSs. The layout is currently designed to switch between the two bosonic isotopes of K. The AOMs are divided into two boxes in Fig. 5.2. The bottom three AOMs in the blue box are used for the 3D-MOT. The top three in the yellow box are used for the 2D-MOT. Each set consists of a single AOM for the cooling light and one AOM for the ^{39}K repump and another for the ^{41}K repump. The red box shows the MTS setup used for locking the laser and introducing an overall offset. Figure 5.3 shows how the AOMs are used to tune the laser close to the different transitions. Switching between the isotopes for the cooling AOM requires changing the order. To switch the repumps we redistribute the light accordingly. Since this chapter focuses on ^{41}K the beam path for

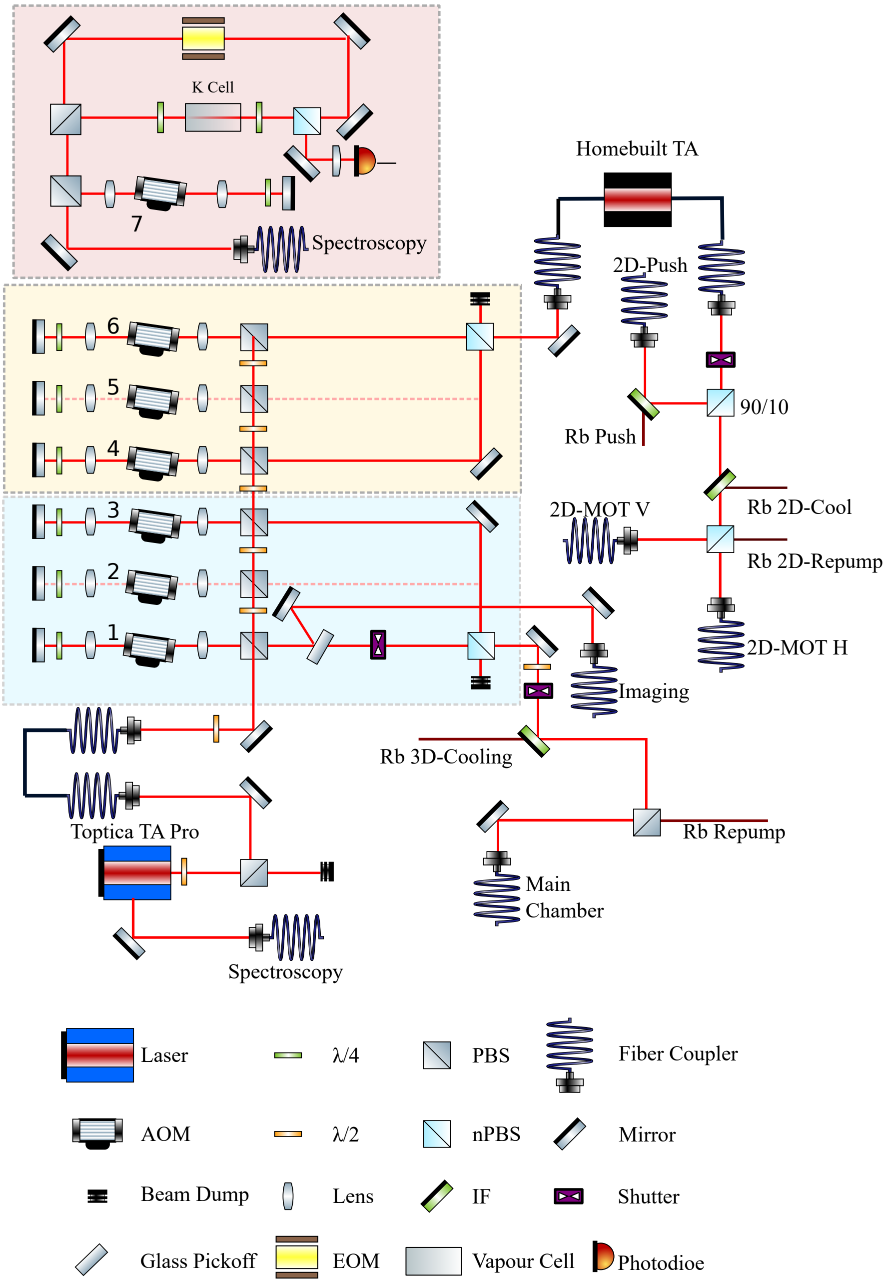

Figure 5.2: Laser schematic for the K-cooling and main chamber imaging. Solid red lines show the laser path. Black solid lines show the fiber optics. Darker red lines indicate the Rb cooling laser and where the beams overlap (the Rb setup is not shown). The key for symbols is at the bottom. AOM: Acoustic Optical Modulator, $\lambda/2$: half waveplate, $\lambda/4$: quarter waveplate, PBS: polarising beam splitter, nPBS: non-polarising beam splitter (50:50 unless otherwise stated), IF: interference filter. Indicated next to fiber couplers are the beams final locations on the main experimental table. Numbers next to AOMs correspond to table: 5.2.

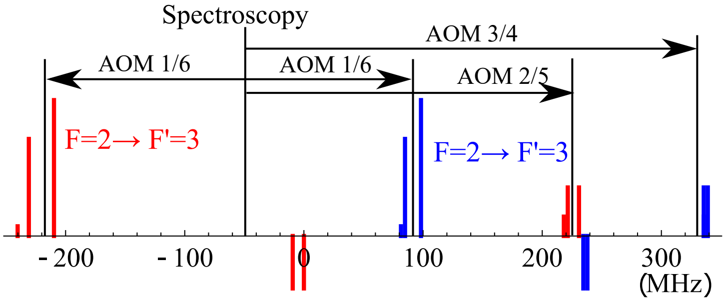

Figure 5.3: Stick spectrum of D_2 lines of K. The spectroscopy line shows where the spectroscopy offset AOM locks the laser frequency with respect to the transitions. The lines then show how the AOMs are used to access the different transitions. Red lines represent the ^{39}K transitions and the blue lines represent the ^{41}K transitions. The peak height indicates the relative oscillator strength. Peaks on the bottom are the same height and represent ground state crossover resonances.

the ^{39}K AOMs are grayed out on the figure. The 3D-MOT AOMs are driven by homebuilt drivers which can be controlled from the lab computer. The 2D-MOT AOMs are also driven by homebuilt drivers but do not need to be controlled from the lab computer since their detunings and powers will remain constant throughout the MOT loading process.

Of the 550 mW only 60 mW is sent to the 2D-MOT AOMS. The output of these AOMs are recombined on a nPBS to match their polarisation and passed through a homebuilt TA. This amplifies the light again. Ten percent of the output of this TA is picked off for the push beam. The push is overlapped on an interference filter with the Rb push and sent to the Rb/K 2D-MOT cell. The remaining 90% is overlapped with the Rb 2D cooling beam on an interference filter. Despite the close proximity of the wavelengths the interference filter allows an overlap with greater than 90% efficiency. This is then combined with the Rb repump before being sent to the 2D-MOT cell cooling axes. It is worth noting that with Rb the repump and cooling light are prepared by separate lasers. The K 3D-cooling AOMs similarly have the repump and cooling beams recombined and are overlapped with the Rb cooling beam on an interference filter before being sent through an optical fibre to the main chamber. At the main chamber the beams have a collimated $1/e^2$ diameter of 1.76(4) cm.

Additional shutters are put in place to block optical paths during the imaging part of the sequence.

5.4 K Fluorescence Imaging

When a MOT is detected fluorescence imaging becomes a very useful diagnostic tool. We use this to optimise the initial loading into a 3D-MOT. In short, the technique works by gathering the scattered photons from a MOT cloud into a photodiode and using the voltage to estimate the atom number. The voltage is directly proportional to atom number so the 2D-MOT can be optimised for atom number without calibration initially. Note, the calibration outlined here was performed after the MOT was optimised and the results in the subsequent section then employ this calibration.

5.4.1 Six Level Theory

We are again at a disadvantage due to the narrow hyperfine structure of K. Fluorescence imaging in most atoms assume a two level model, which is not an assumption that can be safely made here. We instead need a six level model. We follow a similar model to that outlined in [121] which is based on a similar approach used in Cs [122]. We will describe this model here in summary.

The model uses a semi-classical approach in which optical coherences are ignored. Instead, transition rates are modelled using the transitions' oscillator strength. The population of each state is obtained by solving the rate equation when the system is in equilibrium (when the net transfer of populations between states is 0).

The fluorescence imaging will consider two beams. The cooling beam has intensity $\mathrm{I_c}$ and detuning from the $F = 2 \rightarrow F' = 3$ transition of δ_c. The second beam, the repump beam, has intensity I_r and a detuning from the (forbidden) transition $F = 1 \rightarrow F' = 3$ of δ_r. We consider four excited states, the levels in the $P_{\frac{3}{2}}$ manifold, and two ground states, the levels in the $S_{\frac{1}{2}}$ manifold, as depicted in Fig. 4.1. The rate equation for the ground states are:

$$\dot{p_F} = \sum_{F'} R_{F'F}(p_{F'} - p_F) + \Gamma_{F'F} p_{F'}, \tag{5.2}$$

where $R_{F'F}$ is the transition rate between F and F', p_F is the population of state F and $\Gamma_{F'F} = b_{F'F}\Gamma$ and $b_{F'F}$ is the branching ratio between F' and F. The rate equations for the excited states are:

$$\dot{p_{F'}} = R_{F'1}(p_1 - p_{F'}) + R_{F'2}(p_2 - p_{F'}) - \Gamma p_{F'}. \tag{5.3}$$

The transition rates $R_{F'F}$ are given by:

$$R_{F'F} = \frac{c_{F'F}\Gamma_{F'F}}{2} \left(\frac{I_{\mathrm{F}}/I_S}{1 + 4\left(\frac{\delta_F}{\Gamma}\right)} \right), \tag{5.4}$$

where $c_{F'F}$ are the oscillator strengths, I_F is the laser intensity, δ_F is the detuning from $F' = 3$ and I_S is the saturation intensity (1.75 mW cm^{-2}). Setting the equilibrium condition: $\dot{p}_F = 0$ for all states, we arrive at the exact solutions:

$$p_F = \frac{\sum_{F'}(R_{F'F} + \Gamma_{F'F})p_{F'}}{\sum_{F'} R_{F'F}}, \tag{5.5}$$

for the ground states and:

$$p_{F'} = \frac{R_{F'1}p_1 + R_{F'2}p_2}{R_{F'1} + R_{F'2} + \Gamma}, \tag{5.6}$$

for the excited states.

Combining these two equations we obtain:

$$p_2 = \frac{\sum_{F'} \frac{R_{F'2}+\Gamma_{F'2}}{R_{F'1}+R_{F'2}+\Gamma} R_{F'1}}{\sum_{F'} \frac{R_{F'1}+\Gamma_{F'1}}{R_{F'1}+R_{F'2}+\Gamma} R_{F'2}} p_1. \tag{5.7}$$

This formula allows us to obtain the population of the ground state $F = 2$ as a fraction of the $F = 1$ population. Using Eq. 5.6 we can also obtain the populations of the excited states. This gives us the details needed to estimate the atom number with fluorescence imaging. The total power emitted by the MOT cloud is proportional to the sum over the excited states:

$$P = \frac{N\Gamma hc}{\lambda}\sum_{F'} p_{F'}, \tag{5.8}$$

Here h is Plank's constant, c is the speed of light, λ is the transition wavelength and N is the total number of atoms. The detunings applied for optimal 3D-MOT load are: $\delta_{\mathrm{c}} = -4.65\ \Gamma$ and $\delta_{\mathrm{r}} = -6.13\ \Gamma$. The peak intensities for the cooling and repump are, respectively: $\mathrm{I_c} = 5.2\ \mathrm{I_{sat}}$ and $\mathrm{I_r} = 5.5\ \mathrm{I_{sat}}$. This gives us a total excited state population fraction of $\sum_{F'} p_{F'} = 0.32$.

5.4.2 Calibration

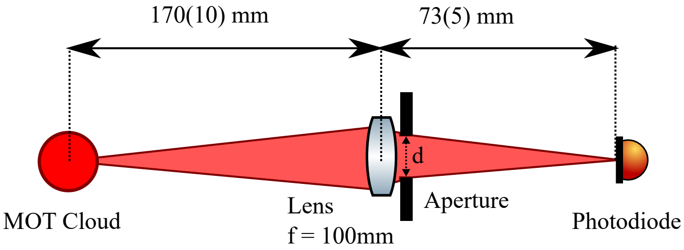

Figure 5.4: Diagram of fluorescence imaging calibration. The photons produced by the MOT cloud are gathered by a lens of focal length 100 mm and focused onto a photodiode. An adjustable aperture is placed immediately in front of the lens to determine the maximum solid angle with which we can view the MOT cloud.

To calibrate the fluorescence imaging we need to obtain the solid angle from which a photodiode can gather light from the MOT cloud. Figure 5.4 shows the calibration setup. The MOT cloud emits photons in all directions equally. A certain fraction of these photons are gathered by a lens and focused onto a photodiode. The first stage of the calibration is determining the solid angle of photons gathered by the lens. The lens provides the uppermost limit of the solid angle but other features, such as the vacuum chamber viewport, may limit this further.

The first stage is to determine the size of the MOT being imaged. A CCD camera is placed at the position of the photodiode without an aperture. The magnification of this system is given by the ratio:

$$M = -\frac{73}{170} = -0.43(4). \tag{5.9}$$

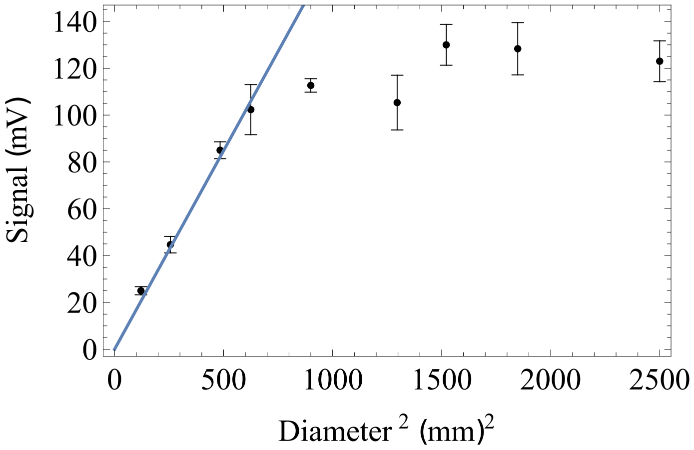

Figure 5.5: Photodiode voltage as a function of the square of the aperture diameter. Data points are shown with standard uncertainties. The line is fit to the first four data points. The data show a linear relationship until 650 mm^2.

The camera detects a MOT image of diameter 2.4 mm in the horizontal direction and 3.2 mm in the vertical direction. Meaning the MOT cloud size being imaged in the horizontal and vertical respectively is: 5.6(5) mm and 7.4(7) mm.

The CCD is removed and the photodiode and aperture now put in place, the voltage reading is recorded as a function of the square of the iris diameter. Figure 5.5 shows the photodiode reading as a function of the iris diameter for the saturated K MOT. When we refer to ‘saturated atom number’ we mean the region the maximum atom number loaded into the 3D-MOT where the loading curve reaches a saturation point. The data are linear up to a diameter of 26 mm (650 mm^2). Since the voltage levels off at this diameter this is the diameter at which all of the possible photons are gathered. Thus we can determine that the solid angle is:

$$\Omega = \frac{d^2\pi}{4L^2}, \tag{5.10}$$

where d is the maximum diameter and L is the distance between the lens and the MOT. From this: $\Omega = 0.176(7)$ sr. This represents fraction of the total power emitted from the MOT cloud. The voltage reading from the photodiode is related to the power incident on it, P_{PD} by:

$$V = \mathcal{R}(\lambda) P_{\mathrm{PD}} R, \tag{5.11}$$

where $\mathcal{R}(\lambda)$ is the responsivity at wavelength λ. From equations 5.8, 5.10 and 5.11 we get the relationship for the atom number of the MOT;

$$N = \frac{16L^2}{d^2} \frac{V}{\mathcal{R}(\lambda) R} \frac{\lambda}{hc} \frac{2}{\Gamma} \left(\sum_{F'} p_{F'} \right)^{-1} . \tag{5.12}$$

In our case, we are using a Thorlabs photodiode PDA100A. The responsivity at 767 nm is 0.51. In addition, we can tune the gain of this photodiode which allows us to vary R. These measurements were taken where $R = 475$ kΩ. Using the linear relationship established in Fig. 5.5 we get a photodiode voltage of $V_{\mathrm{PD}} = 114(3)$ mV. Applying Eq. 5.12 this gives us an estimated atom number of $N = 10.2(3) \times 10^7$ atoms and subsequently a voltage to atom number calibration of $0.0298(9) \times 10^8$ mV^{-1}.

It should be noted that this calibration was done using a temporary photodiode on the larger viewport. These measurements were done with this for two reasons. Firstly, the smaller viewports where the photodiodes will sit permanently do not have enough room around them to install the apparatus for calibrating the photodiode and readings from the permenant diodes would have to be done with a smaller viewport meaning a smaller solid angle. Thus the need for a temporary photodiode to calibrate in parallel. Secondly, we needed three photodiodes to perform a three species MOT measurement as outlined in the next chapter. For the second photodiode, model Thorlabs PDF10A2, its calibration constant was found to be 0.21 times smaller. Thus, for the permanent photodiode the atom number to voltage calibration is $0.142(4) \times 10^8$ mV^{-1}.

5.5 2D-MOT Optimisation

The 2D-MOT was optimised for maximum atom number into the 3D-MOT which was detected by fluorescence imaging. Light from the 2D-MOT is provided by a homebuilt-TA [chip model: Eagleyard EYP-TPA-0765-01500] as shown in Fig. 5.2. This 2D-MOT is shared with Rb for which we identified

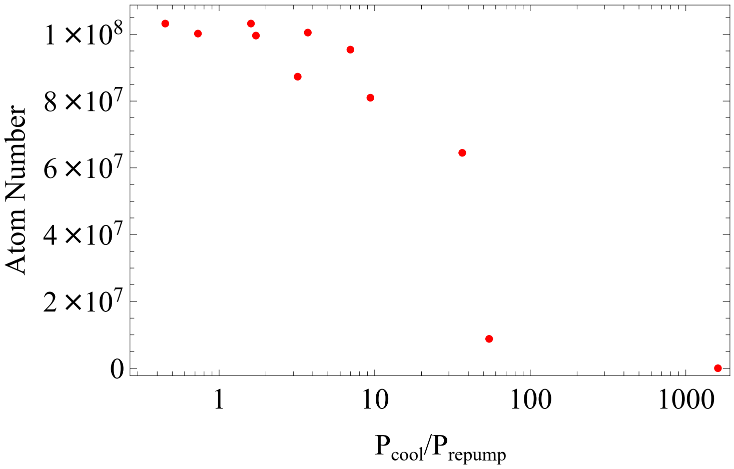

Figure 5.6: Saturated atom number in 3D-MOT vs cooling to repump power ratio in 2D-MOT. x-axis is logarithmic. Atom numbers are taken after 10 seconds of loading. This is used to obtain the optimal ratio of repump to cooling.

the optimal quadrupole gradient at 17.2 G/cm. As such, to best optimise the MOT for K whilst ensuring Rb remains trappable we shall keep the gradient constant at 17.2 G/cm.

5.5.1 Push Optimisation

The output of the homebuilt-TA is split between the cooling axes and the push with a half waveplate and PBS. We are able to actively monitor the atom number in the 3D-MOT using fluorescence imaging. To find the optimal share of the power to be diverted to the push we simply rotated the waveplate until the greatest atom number is achieved in the 3D-MOT. At the optimal setting the power of the push beam is 69 mW (with a beam diameter of 0.8 mm this gives a peak intensity of 156.8 I_{sat}). The rest of the power is diverted to the horizontal and vertical cooling axes which each have a power of 131mW and 167mW respectively. It is worth noting that the push beam is derived from the same light as the cooling and repump beams and as such will have the same detunings as the cooling axes.

5.5.2 Power Optimisation

To optimise the power of the 2D-MOT we first established the ratio at which the power will be split between the cooling and the repump beams for the 2D-MOT. The repump and cooling beams are combined before simultaneously seeding the homebuilt-TA. By keeping the total power roughly constant (a seed power of 12 mW) we can adjust the share of the power sent to the respective repump and cooling AOMs by adjusting the angle of the waveplate placed just before the PBS for AOM 4 in Fig. 5.2. Figure 5.6 shows the cooling power to repump power ratio vs atom number. The measurements of the atom number were taken after 10 s of loading and are all well into the saturated region of the MOT loading curve. Clearly the greater atom number seems to favour the region where the ratio is less than 3. We use a power ratio of 1.4; giving a a total cooling and repump power (along the cooling axes) of 115 mW and 82 mW respectively.

5.5.3 Detuning Parameters Optimisation

The 2D-MOT detuning is varied using the 2D-MOT's cooling and repump AOMs. Figure 5.7(a) shows the saturated atom number in the 3D-MOT as a function of the 2D-MOT cooling beam detuning. The cooling beam is optimal at a detuning of -4 Γ (24MHz). This is well clear of the entire hyperfine manifold suggesting all of the allowed transitions are scattering atoms and providing a net force towards the centre of the trap. For these measurements the repump was sitting at a detuning of -1.84 Γ from the $F = 1 \to F' = 2$ transition. With the cooling optimised, Fig. 5.7(b) shows the atom number as a function of repump detuning. The graph plateaus between -1.6 Γ and -2.3 Γ. We find that a detuning of -2.2 Γ (-13.6MHz) is the region where most atoms are found at. The parameters of the 2D-MOT optimisation are summarised on table 5.3. At the end of this optimisation we can load nearly 10^8 atoms in a time of 12s.

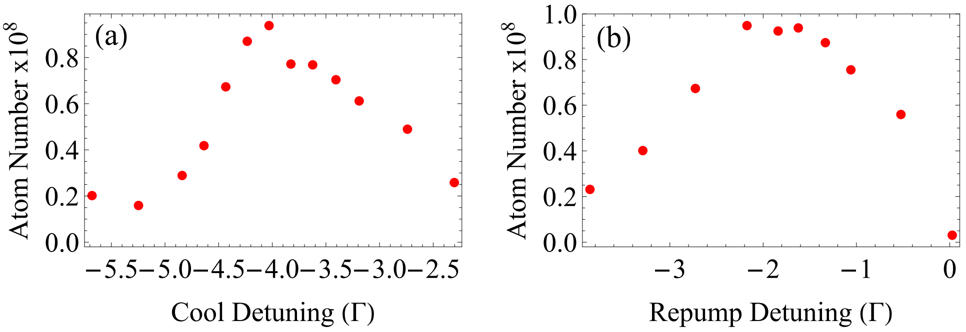

Figure 5.7: (a) Saturated atom number in 3D-MOT (estimated with the fluorescence imaging) vs cooling beam detuning from the $F = 2 \rightarrow F' = 3$ transition for the 2D-MOT.(b) Saturated atom number in 3D-MOT vs repump beam detuning from the $F = 1 \rightarrow F' = 2$ transition for the 2D-MOT.

	Cooling	Repump	Push
Total Power	115mW	82mW	69mW
Total Peak Intensity	$93\mathrm{I}_{\mathrm{sat}}$	$65\mathrm{I}_{\mathrm{sat}}$	$156.8\mathrm{I}_{\mathrm{sat}}$
Detuning	-4 Γ	-2.2 Γ	-4 Γ and -2.2 Γ

Table 5.3: Summary of 2D-MOT parameters.

5.6 K Absorption Imaging

Before optimising further we need to get an idea of what the atomic cloud in the main chamber looks like. Analysing this data can give an us a crucial set of parameters that can be used characterise fundamental aspects of the cloud such as atom number and temperature. We setup and optimise a low resolution imaging system for our K atoms in the main chamber.

This type of imaging is performed by flashing a laser near resonance with an atomic transition twice: once with atoms and secondly without atoms. The must also be circularly polarised to excite the cycling transition. The atoms sit between the absorption beam output and a CCD camera. The difference between the two images can then be used to infer the optical density of the cloud. If the optical density (OD) is not saturated then Beer's law states:

$$I = I_0 e^{-\mathrm{OD(x,y)}} = I_0 e^{-n(x,y)\sigma}, \tag{5.13}$$

where I is the laser intensity incident on the camera with the atoms present, I_0 is the intensity without the atoms, n is the atom number density and σ is the absorption cross section given as [123]:

$$\sigma = \frac{\sigma_0}{1 + 4\left(\frac{\Delta}{\Gamma}\right)^2 + \frac{I_0}{I_{\text{sat}}}}. \tag{5.14}$$

Here σ_0 is the on resonance absorption cross section:

$$\sigma_0 = \frac{\hbar\omega\Gamma}{2I_{\text{sat}}}. \tag{5.15}$$

The OD is given by:

$$\text{OD}(x, y) = \sigma n(x, y). \tag{5.16}$$

The atom number density can be extracted from the absorption image as:

$$n(x, y) = \frac{1}{\sigma} \ln\left(\frac{I_0(x, y)}{I(x, y)}\right). \tag{5.17}$$

It is thus possible to extract the atom number by:

$$N_{\text{atoms}} = \frac{1}{\sigma} \int_{-\infty}^{\infty} \int_{-\infty}^{\infty} \text{OD}(x, y) dx dy. \tag{5.18}$$

Figure 5.8 shows the data taken for optimising the absorption imaging probe for K. Data is initially taken at a bias field of 2.1 G. The field is flipped (therefore flipping the quantisation axis) and the data retaken at $-2.1G$. We can then compare both results. The data are fitted to a Lorentzian:

$$\text{OD}(\delta) = \frac{2A}{\pi} \frac{w}{4(\delta - \delta_0)^2 + w^2} + B, \tag{5.19}$$

where A is the amplitude of the Lorentzian, B is the background, w is the full width at half maximum, δ is the detuning and δ_0 is the detuning where the Lorentzian is maximum. δ_0 is where the cycling transition, including the Zeeman sublevel, is on resonance at the set bias-field. For 2.1 G the optimal detuning is at -3.78(10) MHz and for -2.1 G the optimal detuning is at 2.28(6) MHz.

Two points are of note. Firstly, the optimal detunings are quite different given that the field flip should be nearly symmetric. This is because, as mentioned in the previous chapter, the frequency reference used for locking, $F = 2 \rightarrow F'$, is comprised of multiple transitions due to the unresolved hyperfine structure. So the lock can be estimated to be off the $F = 2 \rightarrow F' = 3$ transition by $\frac{-3.78(10)+2.28(6)}{2} = -0.75(6)$ MHz. Secondly, there is a tail to negative side of the 2.1 G data which does tend to the background value. We can see from Fig. 5.9(c) at a bias field of 2.1 G the $|F' = 2, m_{F'} = 2\rangle$ Zeeman sublevel and the $|F' = 3, m_{F'} = -3\rangle$ are within 10 MHz of each other. This means the $F = 2 \rightarrow F' = 3$ transition used for imaging can no longer be considered isolated.

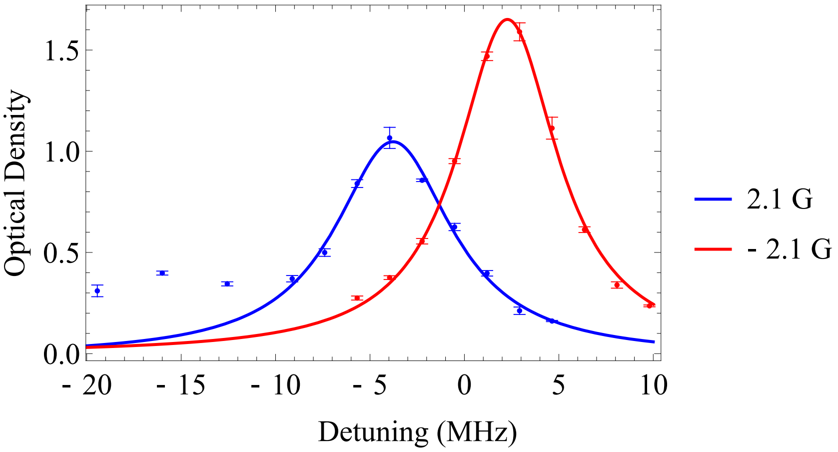

Figure 5.8: Data acquired for optimising the detuning of the probe for absorption imaging. The different colours show the strength of the applied bias field (blue: 2.1 G and red -2.1 G). The probe is scanned over one linewidth and the data fitted to a lorenztian. The vertical axis shows the optical density and the horizontal axis shows the detuning from the $F = 2 \rightarrow F' = 3$ transition in MHz.

We therefore tune our probe to a detuning of +2.28 MHz with the field at -2.1 G. Subsequent optimisation procedures are performed by optimising the OD at each stage since a greater OD implies a greater atom number density, therefore lower temperatures and a greater atom number.

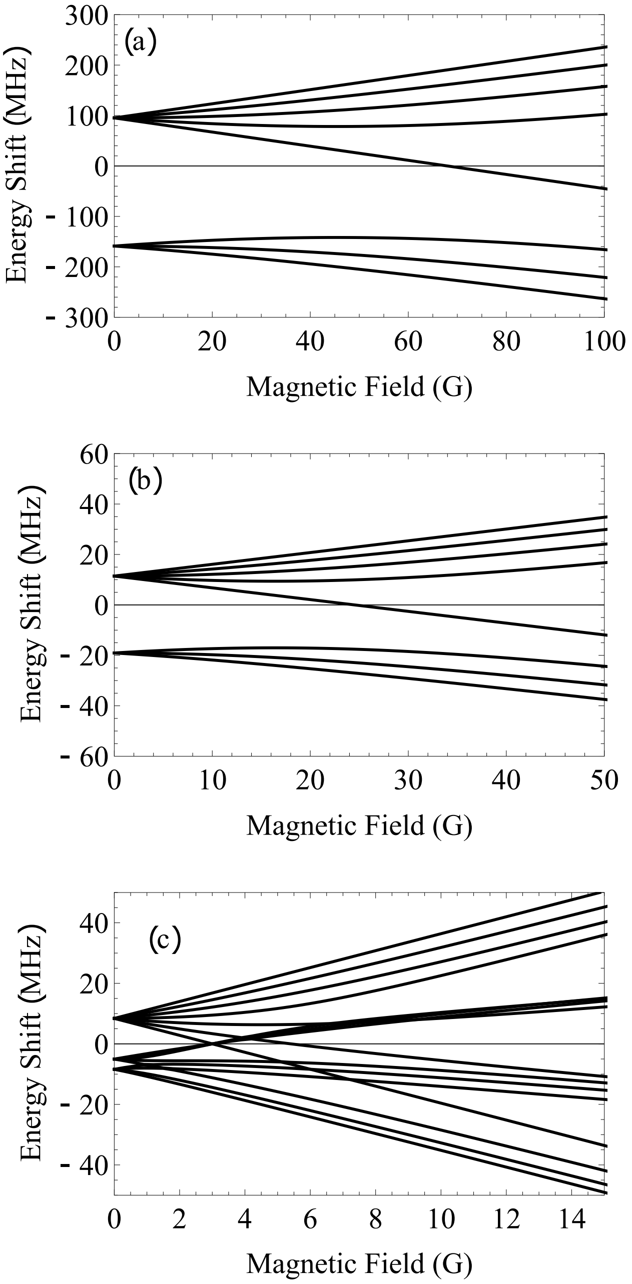

Figure 5.9: Breit-Rabi diagrams for ^{41}K. (a) $S_{1/2}$, (b) $P_{1/2}$ and (c) $P_{3/2}$.

5.7 3D-MOT Optimisation

5.7.1 Initial MOT

We now seek to optimise the 3D-MOT parameters. We do this by optimising the optical density for the different parameters open to us. From Eq. 5.18 we see that finding the maximum optical density also corresponds to the maximum atom number. The parameters we can optimise are: the 3D cool beam detuning, 3D cool beam power, 3D repump beam detuning and the 3D repump beam power. The gradient of the magnetic coils are determined by the optimisation of the Cs loading (which is expected to be loaded simultaneously) and such are kept fixed at Cs loading optimal value of 7.5 G/cm. Note that from herein, detunings on the cooling beam are referenced from $F = 2 \rightarrow F' = 3$ where as detunings quoted on the repump beam are from $F = 1 \rightarrow F' = 2$.

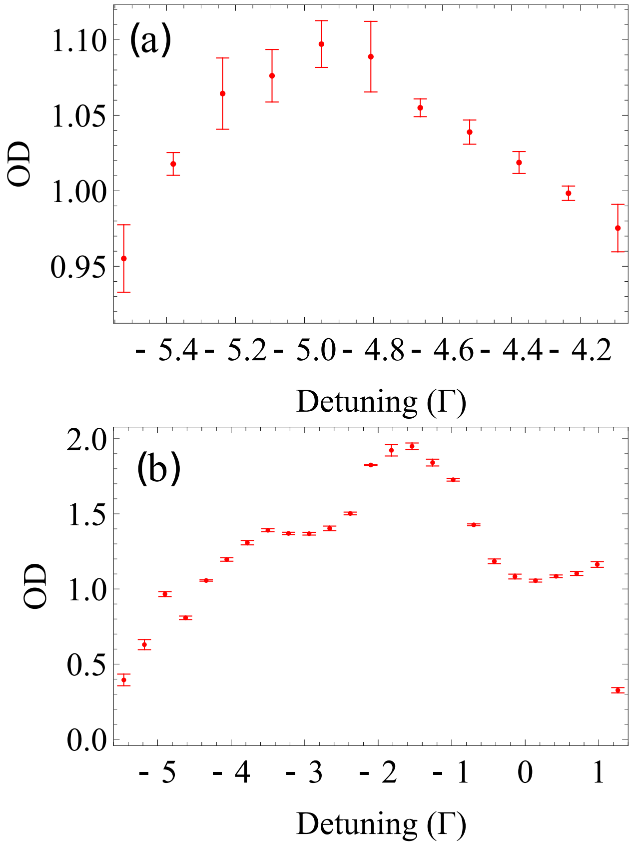

Figure 5.10: Absorption OD dependency of MOT detuning. (a) Cooling beam, 0 Γ refers to the resonance for the $F = 2 \rightarrow F' = 3$ transition. (b) Repump beam, 0 Γ refers to the resonance for the $F = 1 \rightarrow F' = 2$ transition. Standard errors are shown.

Figure 5.10 shows the dependency of the optical density of the MOT as a function of the detuning. Each cooling and repump beam are carrying peak intensities of 5.4(3) I_{sat} and 5.6(3) I_{sat} respectively. We find that the optimal MOT loading occurs at a detuning of -4.9 Γ and -1.8 Γ for the cooling and the repump respectively. In both cases, this is red detuned below the entire $P_{3/2}$ manifold which is not unexpected.

	Detuning	Intensity
Cooling	$-4.7\ \Gamma\ (F = 2 \rightarrow F' = 3)$	5.4(3) $\mathrm{I_{sat}}$
Repump	$-1.8\ \Gamma\ (F = 1 \rightarrow F' = 2)$	5.6(3) $\mathrm{I_{sat}}$

Table 5.4: Summary of 3D-MOT parameters.

Increasing the power into the beams from here will have little effect since the MOT is saturated at these powers. So we maintain the powers at 11.5 mW (5.4(3) $\mathrm{I_{sat}}$) and 12 mW (5.6(3) $\mathrm{I_{sat}}$) per beam for the cooling and repump respectively, the maximum powers. It may be possible to increase the atom number by increasing the 2D-MOT vapour pressure. We can do this by increasing the current to the dispensers but we are reluctant to do this since the dispensers have shown out of character behaviour when increasing the current in the past. Table 5.4 summarises the results of the 3D-MOT characterisation.

5.7.2 cMOT

When the MOT is fully loaded we create a compressed MOT (cMOT) to shrink the size of the atom cloud. This concentrates the atoms towards the centre of the molasses beam arrangement, exposing most of the atoms to most intense part of the beam. This process also increases the phase-space density of the atoms. Compressing the MOT will heat the atom cloud but this heat is subsequently removed with the molasses process. We additionally increase the magnification of the absorption imaging to now image what will now be a smaller MOT.

To compress the MOT we ramp up the magnetic field from 7.5 G/cm to 27.5 G/cm in 1 ms. In addition we reduce the intensities of the beams. The limiting factor of the density of the MOT is the rate of light assisted collisions so further detuning and reducing the intensity are necessary to decrease the rate of such collisions in addition to reducing the photon scattering rate.

Figure 5.11 shows the OD from the absorption image signal as a function of the detuning. The optimal cooling detuning is $-4.7\ \Gamma$. The optimal repump detuning is $-4.2\ \Gamma$ which is a slightly larger detuning to the original MOT.

We find the best intensities per beam are 2.3(2) $\mathrm{I_{sat}}$ for the cooling and 0.35(3) $\mathrm{I_{sat}}$ for the repump. The cMOT is not a stable state so we cannot remain at these parameters for long without losing atoms. We have a 1 ms ramping stage. These parameters are held for 100 ms before a further 1 ms ramp off for the magnetic fields for the molasses adiabatic ramp.

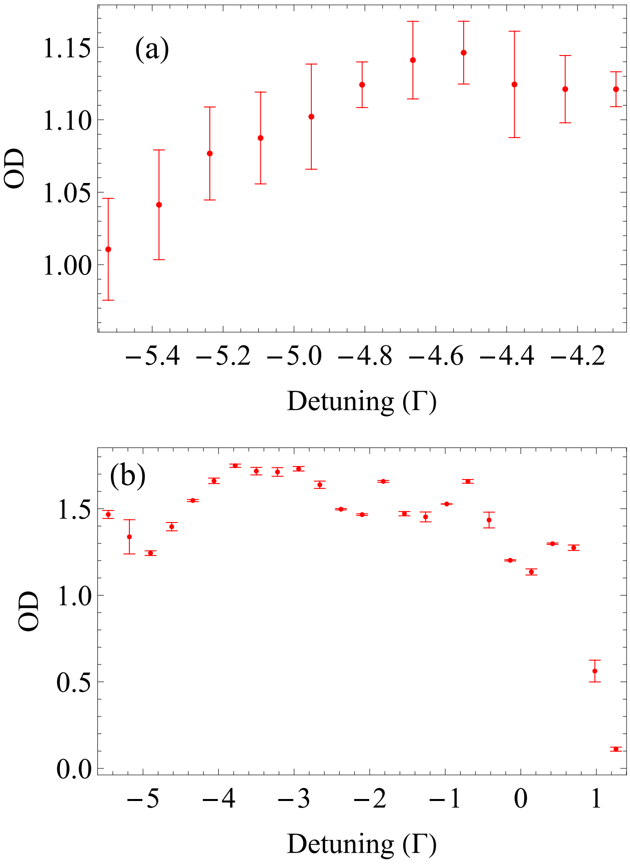

Figure 5.11: Absorption OD dependency of cMOT beams detuning. (a) Cooling beam, 0 Γ refers to the resonance for the $F = 2 \rightarrow F' = 3$ transition. (b) Repump beam, 0 Γ refers to the resonance for the $F = 1 \rightarrow F' = 2$ transition. Standard errors are shown.

	Detuning	Intensity
Cooling	$-4.9\,\Gamma\ (F = 2 \rightarrow F' = 3)$	2.3(2) $\mathrm{I_{sat}}$
Repump	$-4.2\,\Gamma\ (F = 1 \rightarrow F' = 2)$	0.35(3) $\mathrm{I_{sat}}$

Table 5.5: Summary of cMOT parameters.

5.8 Molasses Optimisation

5.8.1 Initial Parameters

This part of the cooling sequence seeks to exploit the sub-Doppler cooling forces so the magnetic field is set to 0(0.2) G. We now bring the cooling detuning to zone I in Fig. 5.1 to access the sub-Doppler cooling effects.

To optimise the for the initial detunings and powers we set the parameters to the initial values and hold the parameters constant for 8 ms. After this we perform a 10 ms time of flight measurement. The measurement is repeated to find the parameter which yields the maximum optical density. After the optimal initial parameters are found we then find the optimal end parameters of an 8 ms ramp again by finding the parameters which optimise the optical density. Finally, a temperature measurement is performed.

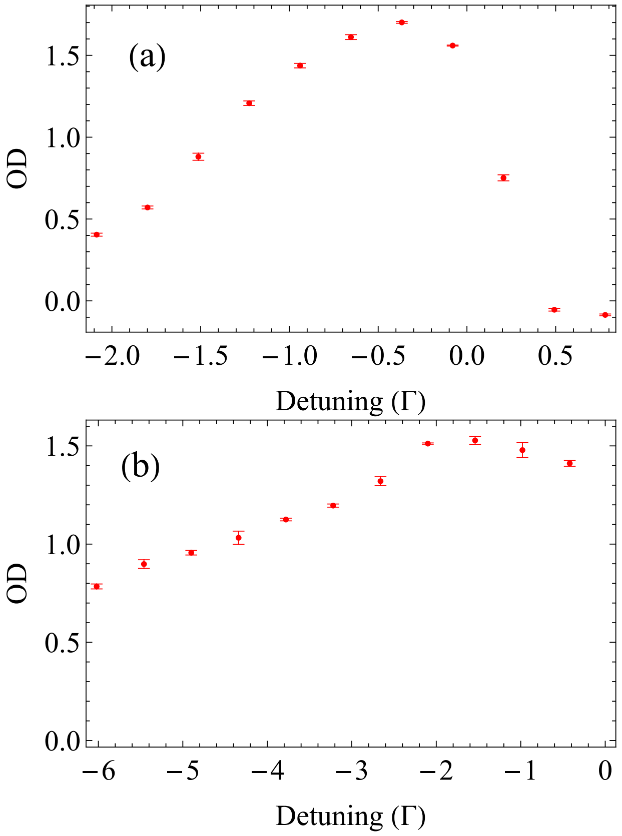

Figure 5.12: Absorption OD dependency of molasses beams initial detuning. (a) Cooling beam, 0 Γ refers to the resonance for the $F = 2 \to F' = 3$ transition. (b) Repump beam, 0 Γ refers to the resonance for the $F = 1 \to F' = 2$ transition. Standard errors are shown.

Figure 5.12 shows the dependence of the OD of the atom cloud on the detuning of the molasses beams at the start the ramp. The molasses process is initiated at detunings of $-0.5\ \Gamma$ for the cooling beam and $-2\ \Gamma$ for the repump beam. The cooling detuning is now very close to the $F = 2 \rightarrow F = 3$ transition allowing us to utilise the large sub-Doppler cooling force. The intensities applied at this stage are 2.3(2) I_{sat} and 0.025(2) I_{sat} for the cooling and repump respectively.

5.8.2 Adiabatic Ramp

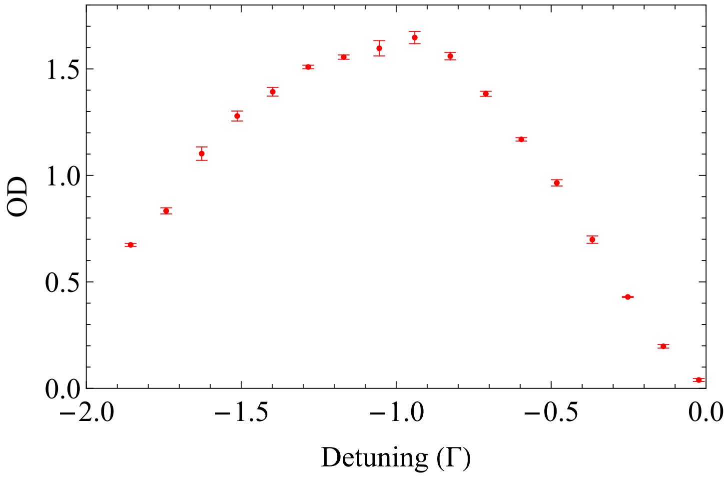

Figure 5.13: Absorption OD dependency of final detuning for molasses. Data for cooling beam, 0 Γ refers to the resonance for the $F = 2 \rightarrow F' = 3$ transition.

From the initial molasses parameters the cooling detuning and intensity is adiabatically ramped to a final value. Sweeping these detunings allows the sub-Doppler cooling forces to interact with a wider range of velocity classes of atoms which narrows our velocity distribution. The ramp is linear and lasts 8 ms. The final detuning of the ramp is $-1.1\ \Gamma$. The final intensity is 0.07(3) I_{sat}. The parameters of the repump beam are kept constant throughout the ramp. Table 5.6 summarises the values for this ramp.

5.8.3 Temperature Measurement

As mentioned earlier it is also possible to obtain a temperature measurement from the absorption imaging. A time of flight (TOF) measurement is used.

	Initial Detuning	Initial Intensity	Final Detuning	Final Intensity
Cooling	$-0.5\ \Gamma$	2.3(2) $\mathrm{I_{sat}}$	$-1.1\ \Gamma$	0.07(3) $\mathrm{I_{sat}}$
Repump	$-2\ \Gamma$	0.025(2) $\mathrm{I_{sat}}$	$-2\ \Gamma$	0.025(2) $\mathrm{I_{sat}}$

Table 5.6: Summary for molasses parameters. The initial values show the repump and cooling parameters at the start of the ramp. The final parameters show the values at the end of the ramp. Where values have changed, the change is linear over 8 ms.

Repeating the experiment to measure the expansion of the cloud, when all cooling and trapping force are off, as a function of time can yield an estimate of the cloud's temperature. If we define the cloud's $1/e^2$ width as σ and its temperature as T then cloud's rate of expansion is related to temperature according to the law:

$$\sigma(t)^2 = \sigma_0^2 + \frac{k_B T}{m} t^2. \tag{5.20}$$

where m is the mass of a particle and k_B is the Boltzmann constant.

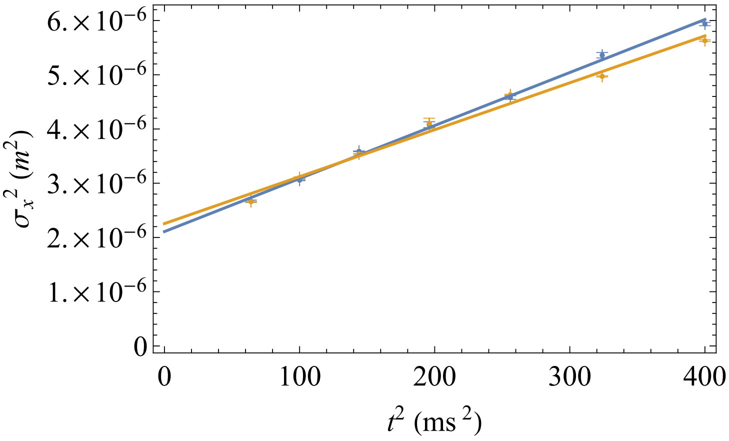

Figure 5.14: Time of flight measurement for potassium temperature at end of molasses. Vertical axis is the σ^2 value of the cloud and the horizontal axis is the t^2 value of the cloud. Orange and blue lines show the expansion of the width in vertical and horizontal directions respectively.

Figure 5.14 shows the data extracted from the TOF measurement. The gradient yields an horizontal temperature of 48.2(1.5) µK and a vertical temperature of 42(2) µK which is in agreement with previous results [109]. The

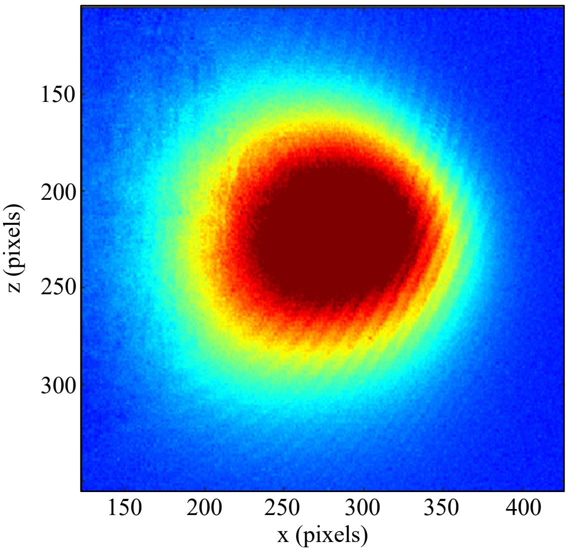

Figure 5.15: Absorption image of potassium after 5 ms time of flight. The x and z axes are in pixels.

absorption images also give us an estimated atom number of $1.02(2) \times 10^8$.

Figure 5.15 shows an exemplar absorption image of the optimised ^{41}K sample after 5 ms time of flight. The cloud's $1/e^2$ width here is 1.7(2) mm and 1.20(13) mm in the x and z directions respectively. The estimated atom number from this image is $1.1(2) \times 10^8$.

5.9 Summary of K MOT and Molasses

Figure 5.16 shows the final and optimised sequence for sub-Doppler cooling of ^{41}K to 48 µK. This allows us to achieve a sample of 10^8 ^{41}K atoms at a temperature of 48.2(1.5) µK in our setup. With the cooling processes now optimised our sample is now prepared for optical trapping and polarised.

5.10 Polarisation of K

Is it necessary to polarise the atom sample into one of the Zeeman states. This ensures the maximum amount of atoms can be captured in a magnetic trap. The choice of available Feshbach resonances are also determined by the polarisation.

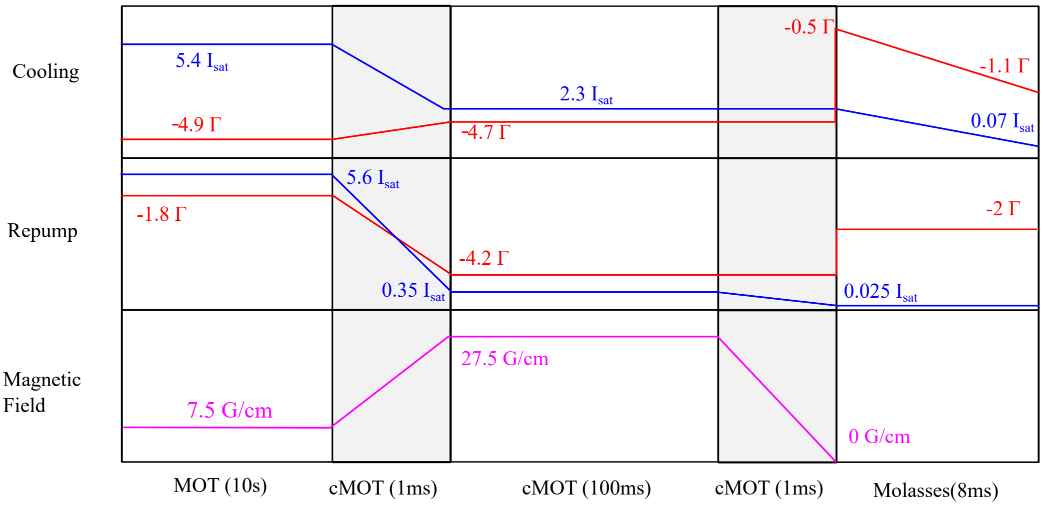

Figure 5.16: Finalised cooling sequence for K to end of molasses. Axes are not drawn to scale. Red lines show the detunings from resonance: cooling transition $F = 2 \rightarrow F' = 3$ and repump transition: $F = 1 \rightarrow F' = 2$. Blue lines show the intensity of the beam. Magenta lines show the magnetic field gradient. The horizontal axis is split into different sections to show the different cooling stage.

5.10.1 Polarisation Scheme

Simple optical pumping schemes allow us to polarise a sample of atoms into either of the ground positive spin stretched states: $\mathrm{S}_{1/2}|F = 1, m_F = 1\rangle$ or $\mathrm{S}_{1/2}|F = 2, m_F = 2\rangle$. Figure 5.17 show the two possible schemes for optical pumping. The $|F = 2, m_F = 2\rangle$ is suitable for magnetic trapping since the Zeeman shift of this state increases linearly with magnetic field strength. From Fig. 5.9 we see that $|F = 1, m_F = -1\rangle$ can be used for magnetic trapping but the Zeeman shift reaches a maximum at about 45.3 G before being pushed down as it enters the Paschen-Back regime. This will limit the maximum trappable temperature for this state. However, $|F = 1, m_F = 1\rangle$ is preferable when searching for Feshbach resonances [42]. We have only optimised polarising into the $|1, 1\rangle$ state thus far.

Applying a bias field and using near resonant σ polarised light will drive transitions that optically pump the spin stretched states where the atoms will remain since this is also a dark state. We use the D_1 transition for this procedure to avoid the unresolved hyperfine structure in the D_2. A repump beam is also necessary since the transitions $F' = 1 \rightarrow F = 2$ and $F' = 2 \rightarrow F = 1$ are allowed which will optically depump our desired F

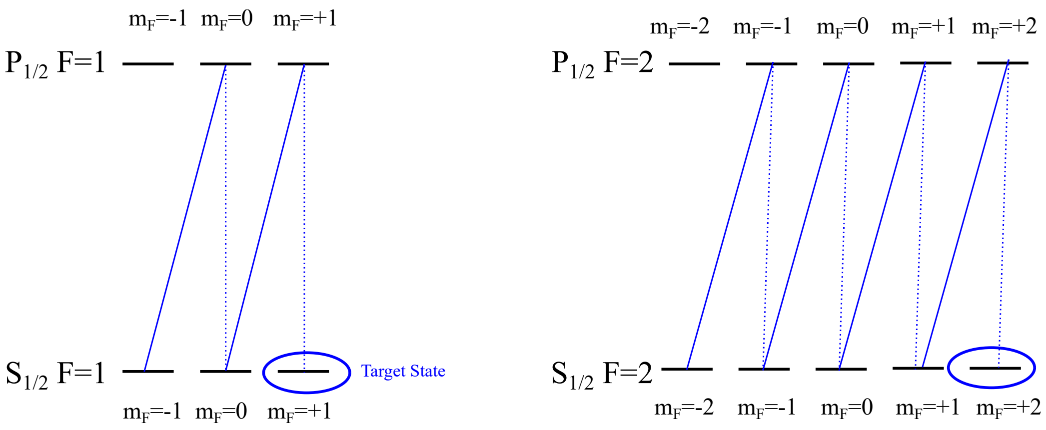

Figure 5.17: Polarising schemes for K. Left: polarising to the $|F = 1, m_F = 1\rangle$ state, right: $|F = 2, m_F = 2\rangle$. Both cases are using circularly polarised light for a σ^+ transition. Solid lines indicate a stimulated transition, broken lines indicate spontaneous emission.

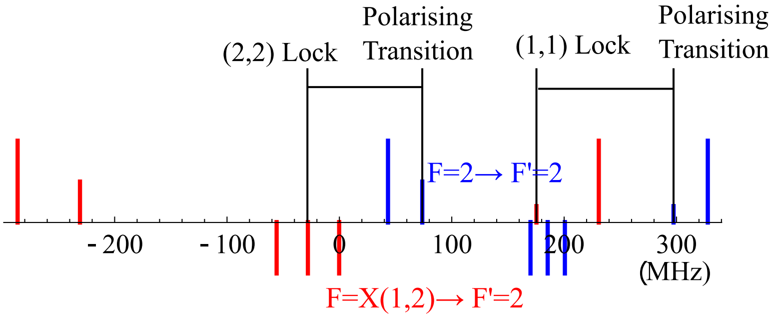

Figure 5.18: Stick spectrum of D_1 lines of K. The black lines show where the laser can be locked and shifted to by our polarising AOM. Red transitions are from ^{39}K and blue transitions are from ^{41}K. Lines on the bottom show ground state crossover resonances. Lines on the top are real transitions whose oscillator strength is indicated by the height of line.

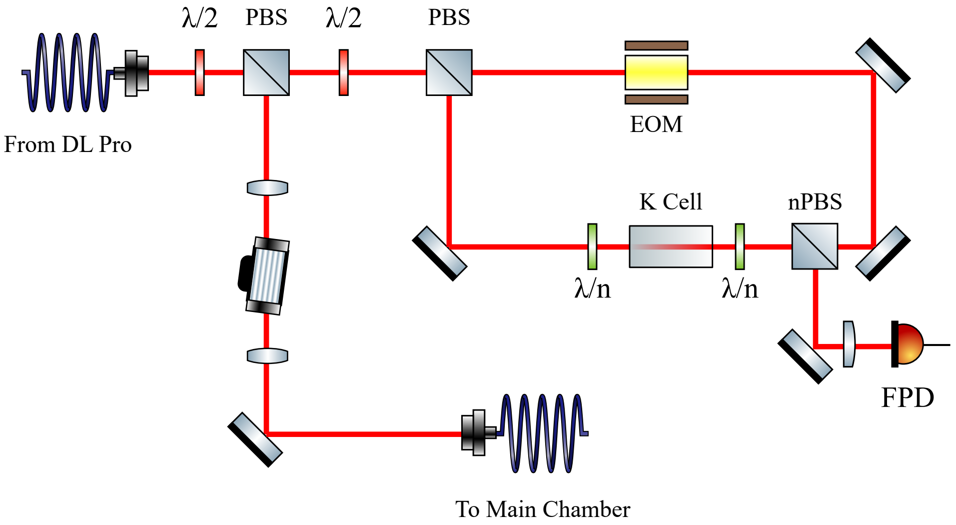

Figure 5.19: Optical setup for polarising atoms. This is a similar to set to Fig. 4.3. Light is produced by a Toptica DL pro which fed to the schematic in this figure through a fibre. Light split between an MTS setup for locking the DL Pro and an AOM which is used for amplitude control.

ground state. For this repump we use the D_2 MOT beams.

5.10.2 Polarising Laser Schematic

Figure 5.19 shows the laser setup used for preparing the polarising light. The light is produced by a Toptica DL Pro and delivered to the setup through a fibre. An MTS setup is used to lock the laser and an AOM, with a centre frequency of 110 MHz, is used for timing and detuning the polarising pulse.

For polarising into the $|1, 1\rangle$ state, the laser is frequency stabilised to the $F = 1 \rightarrow F' = 2$ ^{39}K MTS feature in the lin ∥ lin configuration and the 3D-MOT cooling beam is used to depump the F=2 ground state. However if one wished to polarise into the $F = 2, m_F = 2$ state then locking to the ^{39}K $F = X(2, 1) \rightarrow F' = 2$ feature in the lin⊥lin configuration would be used and instead the 3D-MOT repump would be used to depump the $F = 1$ ground state.

The cooling light is initially applied alone for 200 µs to optically pump to the $F = 1$ ground state. This is done with an intensity of 0.025(2) I_{sat} and a detuning of $-1.1\ \Gamma$ (the final molasses parameters). During this period the shim coils of the chamber are ramped on to provide a provide a bias field of

285 mG parallel to the propagation of the polariser beam. With the cooling light still on, the polariser light is then applied at optimised detunings and intensities for 5ms.

5.10.3 Polariser Optimisation

To optimise the polariser we magnetically trap the atoms with the MOT coils after the polarising sequence has ended. Atoms in the $|F = 1, m_F = 0, -1\rangle$ states will not be trapped. We can obtain the atom number immediately after switching the trap off with an absorption image.

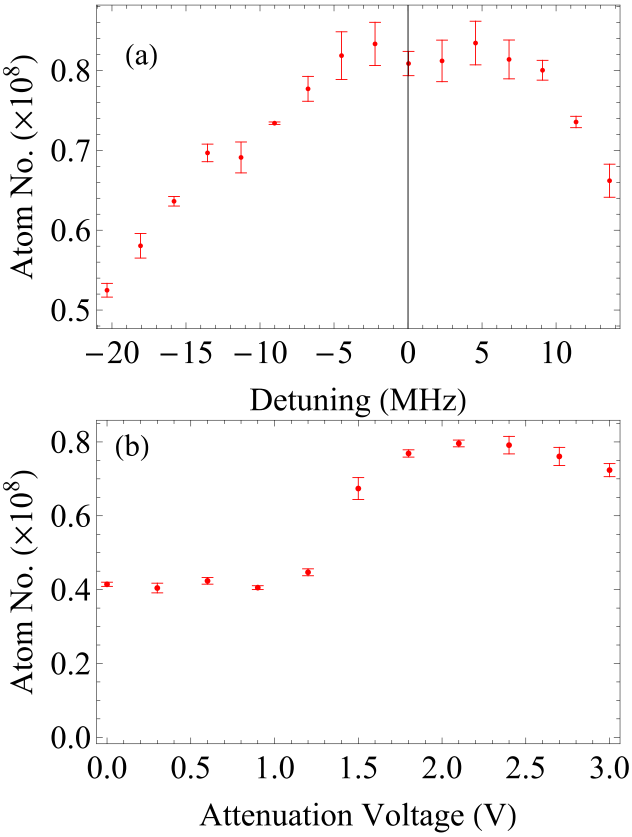

Figure 5.20: Atom number captured in magnetic trap after polarising. (a) Atom number vs polariser detuning. (b) Atom number vs attenuation voltage of the AOM.

Figure 5.20(a) shows the parameter optimisation for the polariser beam. The detuning is found to be optimal at -2.22 MHz from the $F = 1 \rightarrow F' = 1$ transition. There is a slight dip in atom number when on resonance. Figure 5.20(b) shows the atom number as a function of the attenuation voltage applied to the AOM. The optimal attenuation voltage corresponds to a power of 400(20) µW.

The atom number achieved in the magnetic trap after polarising is $0.83(3) \times 10^8$ atoms (out of 1.08×10^8). Without a polariser this number is 0.35×10^8. So the polariser yields an increase 44% efficiency for 77% total efficiency.

5.11 Outlook

Having prepared a sample of ^{41}K we are now in a position for subsequent cooling steps. We have tried to load K into an optical dipole trap from this stage previously but the relatively high temperature resulted in very short trap lifetimes. In next the stage will involve a magnetic trap which may either be used to evaporatively cool the K directly or sympathetically cool the K by evaporating with another species. In the next chapter we discuss a three species MOT in which it may be possible to load Rb as a sympathetic coolant. We hope to cool ^{41}K to BEC with Cs to search for Feshbach resonances. Most of this experimentation regarding molecule formation will be performed in the main chamber before we move KCs to the science cell.

Chapter 6

Three Species Magneto-Optical Trap

6.1 Introduction

We have found that loading ^{41}K into a dipole trap simultaneously with Cs has proven quite difficult. Currently, when Cs is prepared for loading into a 1064 nm optical dipole trap the temperature is typically on the order of 1 µK after DRSC. However, the temperature of ^{41}K, as discussed in chapter 5, is near 50 µK after molasses. At present we do not have further cooling for K in the form of gray molasses or DRSC. These can be implemented but we do not have the funding available at present. For ^{41}K gray molasses has proven only to reach 42 µK [110] and DRSC on this species remains untested.

This temperature difference presents a problem when trying to mix the two species in an optical dipole trap. The dipole trap that is used for Cs is too shallow for K but increasing the power of the dipole trap to compensate also increases the heating rate for Cs. An alternative method we could potentially use would be to utilise our Rb to sympathetically cool Cs and K in a magnetic trap. Prior to this, we need to study loading three species simultaneously in a MOT.

This chapter will introduce our laser schematic for cooling Rb and Cs. We will also discuss the optimisation of the fluorescence imaging and give a brief summary on the MOT parameters for both species. Finally, we will look at fluorescence image curves from loading all three species into the MOT, similar to [124].

6.2 Laser Layout for Rb and Cs

6.2.1 Rb

Figure 6.1 shows the laser setup used for the MOT light, Doppler and Sub-Doppler cooling and absorption imaging for Rb.

The main cooling light is provided by a Toptica TA pro optimised for 780 nm and capable of outputting up to 2 W of power. The light is passed through a high power fiber to make the beam Gaussian. This light is then passed through an AOM bank consisting of five AOMs, the purpose of which is provided on Table 6.1. AOMs 2 and 5 are double passed and feed directly into the 2D-MOT and 3D-MOT respectively. Both the 2D-MOT and 3D-MOT light are overlapped with the K lasers (magenta lines) on an interference filter. The interference filters are not exactly at 45° with respect to the reflected beam, rather the angle is precisely tuned to optimise the power from the K cooling beams. AOM 3 feeds into the push beam which is overlapped with the K 2D cooling light on a PBS. Additionally, AOMs are used to time the sequence.

Laser light from the side-port of the TA (light directly from the diode) is delivered to a spectroscopy setup. The setup consists of an AOM for offset locking the laser and a Rb cell with a retro-reflected beam. This allows us to obtain the sub-Doppler transmission signal. The laser current is modulated to obtain the error signal for locking. The laser is locked to the ^{87}Rb D$_2$ $F = 2 \rightarrow F' = 3$ transition.

AOM 1 provides light for polarising and degenerate Raman sideband cooling (DRSC). A discussion of the DRSC is beyond the scope of this thesis. In the case of AOM 5 the 2D cooling light is double passed but the 0th order is reflected to another AOM path which will be used in the future for the 'blast': removing unwanted Rb atoms in the microscope imaging cycle.

The repump light is provided by a separate Toptica DL pro. It is fed directly to a pair of AOMs: 7 which is used for the amplitude and offest control of the repump beam and 8 which is used for the degenerate Raman sideband cooling. A small amount of the Rb repump power is picked off for locking the repump. Note that the Rb cooling light shares fibres with the K cooling light so both MOTs are exactly overlapped at the main chamber.

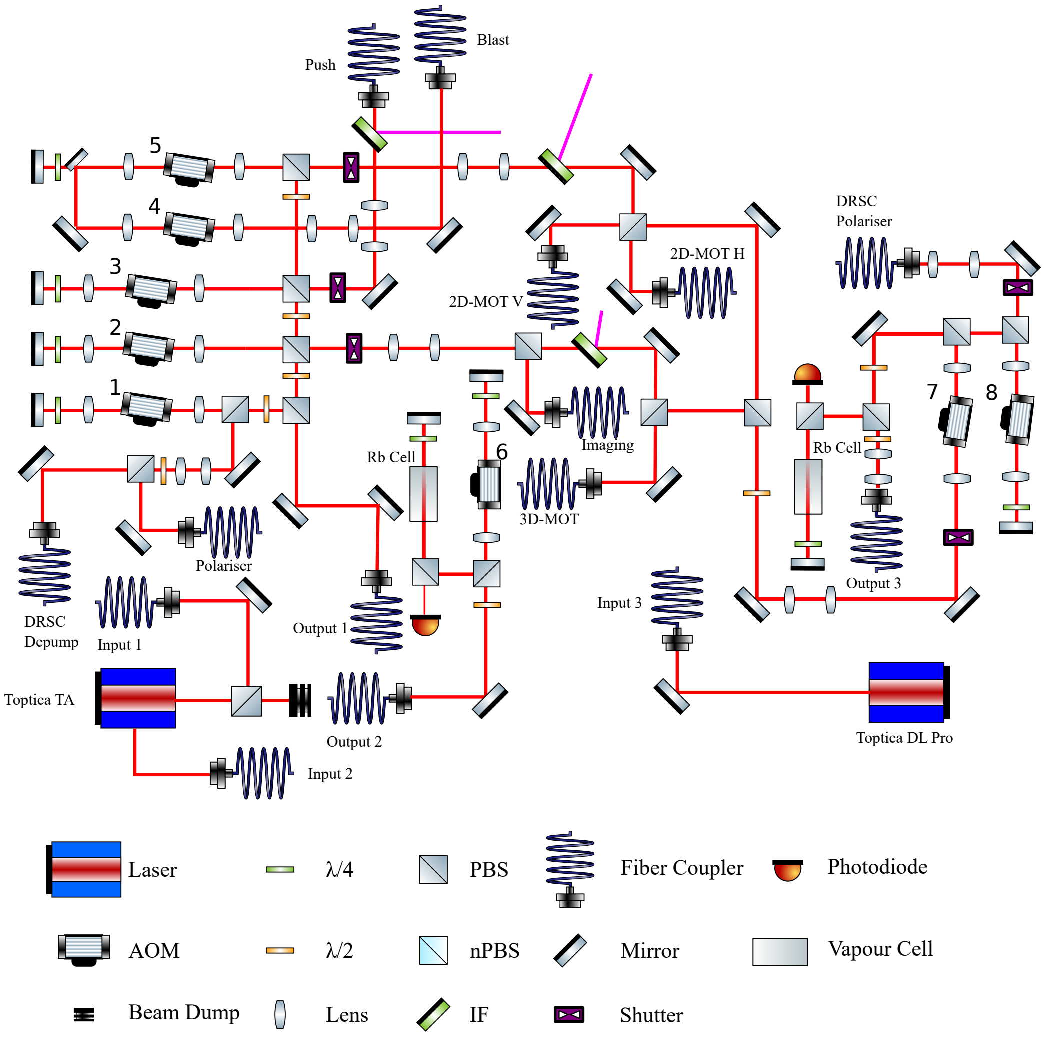

Figure 6.1: Laser schematic for the Rb-cooling and main chamber imaging. Solid red lines show the laser path. Fibre optics are linked with 'input'/'output' labels. Magenta lines indicate the beams from the K setup and correspond to the overlap sites indicated in Fig. 5.2. The key for symbols is at the bottom. AOM: Acoustic Optical Modulator, $\lambda/2$: half waveplate, $\lambda/4$: quarter waveplate, PBS: polarising beam splitter, nPBS: non-polarising beam splitter (50:50 unless otherwise stated), IF: interference filter. Indicated next to the fiber couplers are the beams final locations on the main experimental table. Numbers next to AOMs correspond to Table 6.1.

AOM Number	AOM Purpose	Model
1	DRSC Depump	G&H AOMO 3110-120
2	3D Cool	G&H AOMO 3110-120
3	Push	G&H AOMO 3110-120
4	Blast	G&H AOMO 3110-120
5	2D Cool	G&H AOMO 3110-120
6	Spectroscopy Offset	G&H AOMO 3110-120
7	Repump	G&H AOMO 3080-122
8	DRSC Polariser	G&H AOMO 3080-122

Table 6.1: Table outlining the purpose of AOMs shown in Fig. 6.1. 'G&H' refers to Gooch and Housego. This table is for Rb cooling.

6.2.2 Cs

Figure 6.1 shows the laser setup used for the MOT light for, Doppler and Sub-Doppler cooling and absorption imaging for Cs.

The main cooling light is provided by a Toptica TA pro optimised for 852 nm and capable of outputting up to 2 W of power. The light is initially passed through a high power fiber. This light is then passed through an AOM bank consisting of five AOMs, the purpose of which is provided on Table 6.2. AOMs 2 and 5 are double passed and feed directly into the 2D-MOT and 3D-MOT respectively. AOM 3 feeds into the push beam which is overlapped with the K cooling light on a PBS. AOMs are again used for timing the sequence.

Laser light from the side-port of the TA (light directly from the diode) is delivered to a spectroscopy setup. The setup consists of an AOM for offset locking the laser and a Cs cell with a retro-reflected beam. This allows us to obtain the sub-Doppler transmission signal. The laser current is modulated to obtain the error signal for locking. The laser is locked to the ^{133}Cs D$_2$ $F = 4 \rightarrow F' = 5$ transition.

AOM 2 is doubled passed but the 0th order is fed directly to AOM 1 which is a double passed AOM for the Cs DRSC. Likewise, the 0th order of AOM 5 is passed through AOM 4 for the blast.

The repump light is provided by a separate Toptica DL pro. It is fed directly to a pair of AOMs: 7 which is used for the amplitude and offest control of the repump beam and 8 which is used for the degenerate Raman sideband cooling. A small amount of the Rb repump power is picked off for locking the repump. Cs has delivery fibres independent from the Rb/K MOT so it is at an advantage in that the MOTs can be slightly displaced allowing for less loss due to light assisted collisions. The displacement can be removed in subsequent cooling stages (for example both species will share the same dimple trap). We have used an alternative method in one of our other labs where Rb and Cs are displaced at the MOT stage by using an on resonant probe beam which slightly shifts one MOT.

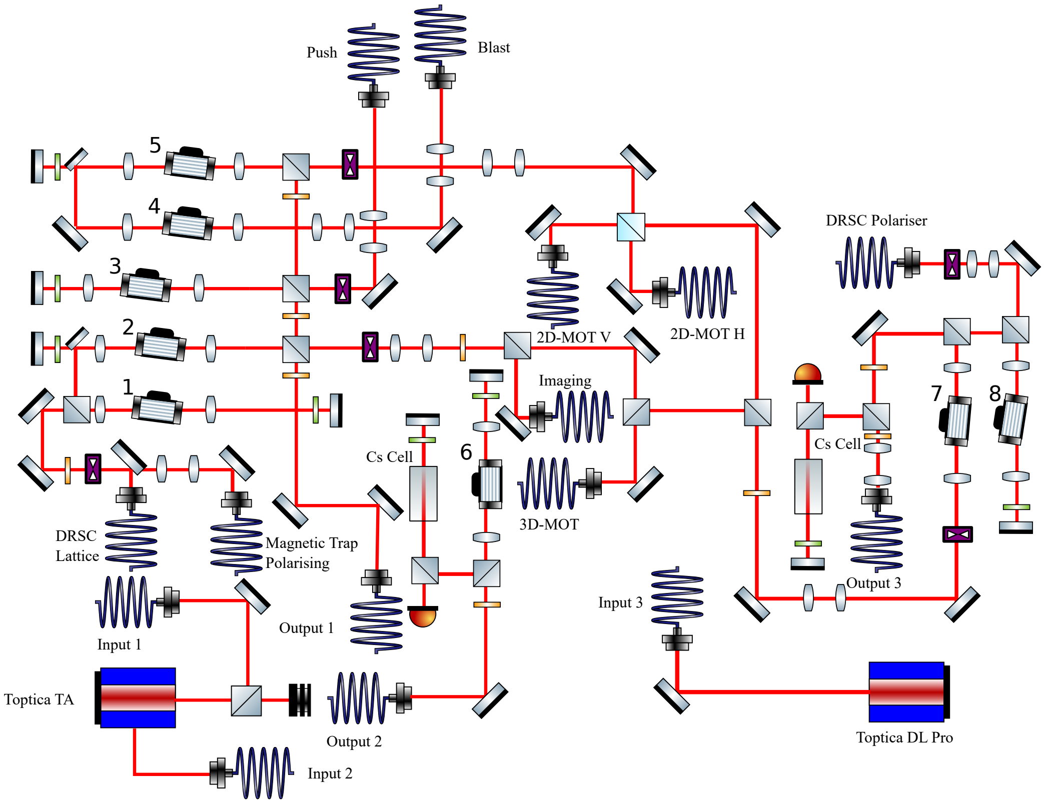

Figure 6.2: Laser schematic for the Cs-cooling and main chamber imaging. Solid red lines show the laser path. Fibre optics are linked with‘input’/‘output’ labels. The key for symbols is located in Fig. 6.1. Numbers next to AOMs correspond to Table 6.2.

AOM Number	AOM Purpose	Model
1	DRSC Lattice	G&H AOMO 3200-124
2	3D Cool	G&H AOMO 3110-120
3	Push	G&H AOMO 3110-120
4	Blast	G&H AOMO 3110-120
5	2D Cool	G&H AOMO 3110-120
6	Spectroscopy Offset	G&H AOMO 3110-120
7	Repump	G&H AOMO 3110-120
8	DRSC Polariser	G&H AOMO 3110-120

Table 6.2: Table outlining the purpose of AOMs shown in Fig. 6.2. ‘G&H’ refers to Gooch and Housego. This table is for Cs cooling.

6.3 MOT Parameters Summary

Tables 6.3 and 6.4 show the parameters for the 3D-MOT and 2D-MOT, respectively, for all species in the 3 species MOT. These parameters are the optimised parameters for the individual species (when no other MOT is on) and will be the parameters we will use in this chapter when testing our 3 species MOT. These parameters were applied at a gradient of 7.5 G/cm.

Species	Cooling Detuning (Γ)	Repump Detuning (Γ)	Beam $1/e^2$ Diameter (cm)	Cooling Intensity (I_{sat})	Repump Intensity (I_{sat})
^{41}K	-4.9	-1.8	1.76	5.4	5.6
^{133}Cs	-1.02	0	1.74	60.8	2.4
^{87}Rb	-1.99	0	1.76	57.3	3.09

Table 6.3: Table showing the cooling parameters for the 3D-MOT for all three species. The detunings are in units of Γ where Γ is the natural linewidth of the species to which the detuning refers to ($\Gamma = 6.0$ MHz for Rb and K and $\Gamma = 5.2$ MHz for Cs). Beam diameter is an average of the 3 MOT beams. I_{sat} is the saturation intensity of the species to which the listed intensity refers to (1.8 mW/cm^2 for K, 1.7 mW/cm^2 for Rb and 1.1 mW/cm^2 for Cs).

The full optimisation for these parameters are presented only in summary in this thesis.

Species	Cooling Detuning (Γ)	Repump Detuning (Γ)	Beam $1/e^2$ Vertical Diameter (cm)	Beam $1/e^2$ Horizontal Diameter (cm)	Cooling Power (mW)	Repump Power (mW)
^{41}K	-4	-2.2	0.81	7.9	115	82
^{133}Cs	-2.7	0	0.84	7.8	160.5	5.3
^{87}Rb	-3.79	0	0.81	7.9	105.5	7.2

Table 6.4: Table showing the cooling parameters for the 2D-MOT for all three species. The detunings are in units of Γ where Γ is the natural linewidth of the species to which the detuning refers to. Beam powers quoted are averages of the vertical and horizontal powers.

6.4 Fluorescence Imaging Calibration

In this section we calibrate the fluorescence imaging in a similar fashion to that used in Sec. 5.4. Figures 6.3 (a) and (b) show the data for the calibration of the fluorescence imaging for Rb and Cs. Similar to K, the captured fluorescence is focused onto a wide area diode. An iris is placed in front of the collection lens and the signal voltage as a function of the square of the iris diameter is recorded. In addition to the data, Fig. 6.3 (a) and Fig. 6.3 (b) also show the linear fits to the region of the data where there is linear behaviour.

Unlike in the K case, we can use a simple two level model for the calibration of Rb and Cs since their hyperfine structures are much better resolved. Recall equation 5.12:

$$N = \frac{16L^2}{d^2}\frac{V}{\mathcal{R}(\lambda)R}\frac{\lambda}{hc}\frac{2}{\Gamma}\left(\sum_{F'} p_{F'}.\right)^{-1} \tag{6.1}$$

For a two level model the equation can be reduced to:

$$N = \frac{16L^2}{d^2}\frac{V}{\mathcal{R}(\lambda)R}\frac{\lambda}{hc}\frac{2}{\Gamma}\frac{1+4\left(\frac{\delta}{\Gamma}\right)^2 + I/I_{\text{sat}}}{I/I_{\text{sat}}}. \tag{6.2}$$

where I is the beam intensity, I_{sat} is the saturation intensity, δ is the delta is the detuning and the remaining symbols have their usual meanings defined

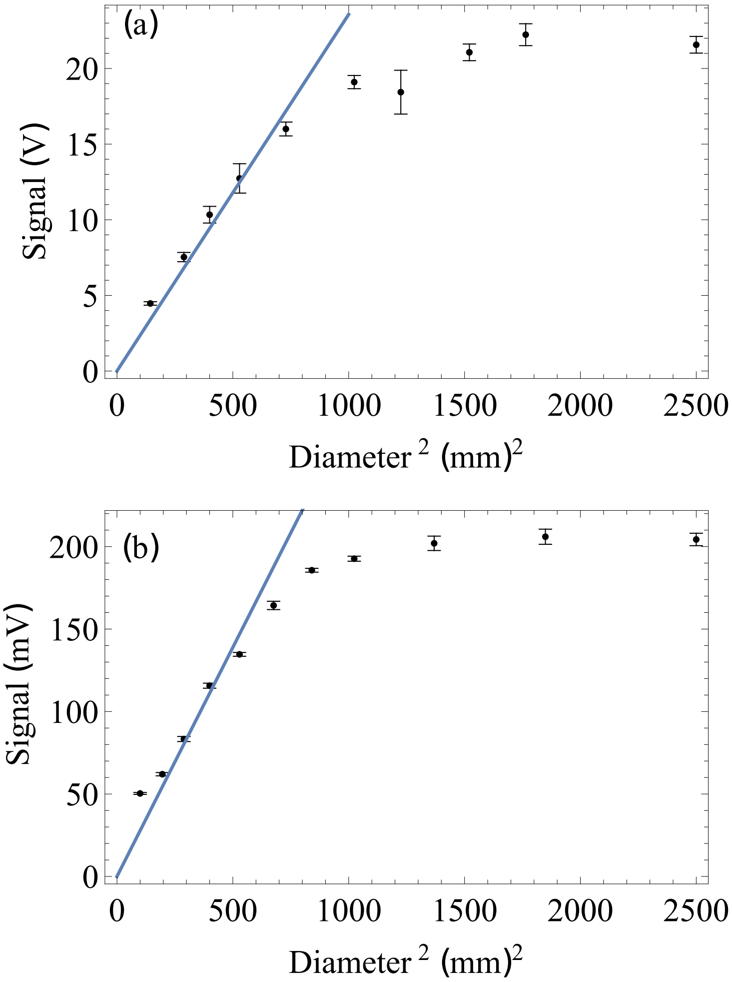

Figure 6.3: Photodiode voltage as a function of the square of the aperture diameter for (a) Cs and (b) Rb. Data points are shown with standard uncertainties. The line is fit to the first five data points. The data show a linear realtionship until 729 mm^2 for Cs and 529 mm^2 for Rb.

in equation 5.12.

For both species the approximate distance between the MOT and the iris is $L = 176$ mm.

The photodiode used was Thorlabs model PDA100A. For Cs the responsivity is $\mathcal{R}(\lambda) = 0.55$ A/W and the gain is set such that $R = 47500\ \Omega$. A voltage reading of $V = 16.4$ mV at an iris diameter of $d = 27$ mm gives an estimated atom number of 1.2×10^8 atoms, or a calibration of $0.073 \ \times 10^8$ mV^{-1}. As in the case K, this calibration was done with a temporary photodiode. A permanent photodiode, Thorlabs model PDF10A2, was calibrated in parallel which has a resulting calibration of $1.5 \ \times 10^6$ mV^{-1}.

For Rb: $\mathcal{R}(\lambda) = 0.51$ A/W and $R = 47500\ \Omega$. We obtain $V = 109.7$ mV at an iris diameter of $d = 22$ mm yielding an estimated atom number of 99.2×10^8 atoms. This results in a calibration of $0.90\ \times 10^8\ \text{mV}^{-1}$. Again, this number on a permanent photodiode has the calibration $1.2\ \times 10^7\ \text{mV}^{-1}$.

6.5 Realisation of Three Species Magneto Optical Trap.

In order to study a 3 species MOT, we run a sequence which incorporates all combinations of atomic species. Figure 6.4 shows the atom number over time as the sequence is run and Table 6.5 shows which MOTs are active at each point in the sequence.

Initially, the Rb is loaded on its own followed by a combination of Cs and Rb. This prevent the Cs MOT from reaching the maximum atom number due to a slight interaction between the MOTs. In the next region the Rb is switched off. In region IV the potassium MOT is activated in parallel to the Cs MOT. Since the K MOT is significantly smaller than the Rb MOT then there is little interaction between the K and Cs MOT.

In region VI where both the K and Rb MOT are active there is a significant drop in atom number for K, though not completely. Since K and Rb share the same fibres to deliver the laser light from the main table but not Cs, then the light assisted collisions with Rb will cause the atom number in K to drop off quite significantly as shown. This is something that will have to be taken into consideration moving forward. It may be possible to apply a similar technique as described prior, where a probe beam can be used to introduce a displacement to one of MOTs.

It is important to note that the Cs MOT is physically displaced from the Rb/K MOT because Cs has its own MOT beams. Hence, Rb and K when on at the same time will undergo light assisted collisions which drops the population of the K MOT to about 10% of its total value and drops Rb slightly. However, Cs does not interact as with the others.

Region	Rb	Cs	K
I	On	Off	Off
II	On	On	Off
III	Off	On	Off
IV	Off	On	On
V	Off	Off	On
VI	On	Off	On
VII	On	On	On

Table 6.5: Table outlining which set of laser cooling beams are on or off for each point of the sequence in fig 6.4.

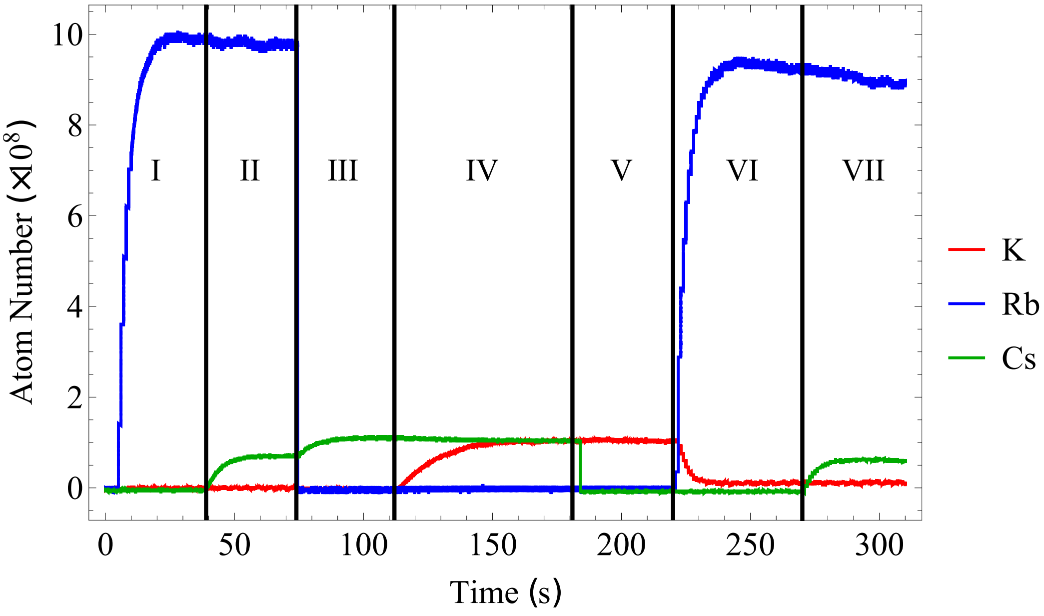

Figure 6.4: Flourescence signal showing the estimated atom number MOT loading for each species (obtained from the fluorescence imaging). In each region a different combination of MOT cooling beams are used. The combination in each region is shown on Table 6.5.

6.6 Outlook

It is important to note, the reason for pursuing this 3 species MOT was because we were having difficulty combining K and Cs in an optical dipole trap, most notably due to the temperature differences. K is of the order of 50 µK at the end of the molasses and Cs can reach the order of 2 µK after DRSC. This temperature difference has the consequence of reducing the dipole trap lifetime for both species.

One possible solution that is proposed is to use the Rb, of which there is clearly a large abundance of, as a sympathetic coolant for both Cs and K in a magnetic trap. The unfortunate hyperfine scattering properties of Cs and K make this quite difficult. In essence, the trappable states of Cs are $|F = 3, m_F = -3\rangle$ and $|F = 4, 4\rangle$. It has been previously established that two body losses for the $|4, m_F 4\rangle$ state are quite high owing to inelastic collisions arising from the magnetic dipole interactions [125]. Alternatively one could use the $|F = 3, m_F = -3\rangle$. However, the trappable K state which is not limited by the Paschen-Bach regime is the $|F = 2, m_F = 2\rangle$ state. In this case both Cs and K would be in a spin stretched state but the m_F number would have a different sign which would almost certainly lead to two body losses due to spin flip collisions. We are studying the theory to attempt to estimate the two body loss rate to establish the viability of this method.

Another solution might be to sequentially load the Cs after K but cool the K, again using Rb, prior to loading the Cs. As outlined in chapter 3, we constructed a magnetic trap extension to our main chamber but have yet to test it which we hope to do soon.

Chapter 7

Multi Purpose Cavity Locking

7.1 Introduction

A crucial part of the indirect molecule formation is stimulated Raman adiabatic passage (STIRAP). STIRAP requires laser frequency stabilisation at frequencies where there isn't a convenient atomic or molecular reference line and linewidth narrowing to better than 1 kHz. This is conveniently achieved by stabilising the laser frequencies to a high finesse optical cavity.

In addition to STIRAP, we also have plans to study Cs Rydberg atoms in optical tweezers (not in our microscope apparatus). The wavelengths associated with KCs STIRAP are 915 nm and 1415 nm for the Stokes and pump transitions respectively. For Cs Rydberg atoms a three photon excitation can be accessed with the wavelengths: 895 nm and 1359 nm to transfer atoms from $6S_{1/2} \rightarrow 7S_{1/2}$ via the D_1 transition in preparation for the jump to Rydberg states. Since the wavelengths for either application are coincidentally close we can readily tune an ECDL with a diffraction grating for the appropriate purpose as needed.

We outline the development of the Pound-Drever-Hall locking system for such lasers. We will give an overview of the cavity, followed by a layout and discussion of the preparation of the laser system and finally a brief spectroscopic study of the first two transitions in the Rydberg excitation scheme in Cs.

7.2 Applications

7.2.1 KCs STIRAP

When molecules are associated on a Feshbach resonance they will be on a weakly bound vibrationally excited state. We can transfer the molecules to the rovibrational ground state using STIRAP. STIRAP is a two-photon process where accurately timed pulses can transfer the molecules from one state to another via an intermediate dark state using a Raman resonance [14, 126–129].

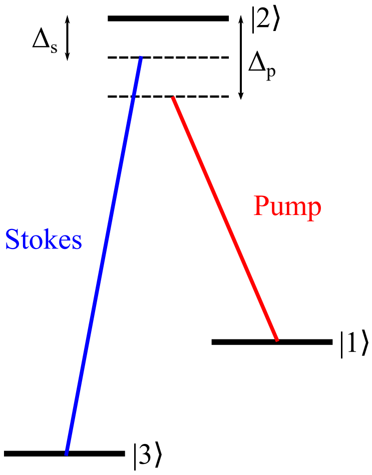

Figure 7.1: Three level energy diagram for STIRAP. $|1\rangle$ is the initial state. We aim to transfer the population to $|3\rangle$ using the intermediate state.

Consider a three level system with levels

$$|1\rangle = \begin{pmatrix}1\\0\\0\end{pmatrix} \quad |2\rangle = \begin{pmatrix}0\\1\\0\end{pmatrix} \quad |3\rangle = \begin{pmatrix}0\\0\\1\end{pmatrix}. \tag{7.1}$$

and in the configuration shown in Fig. 7.2. In our molecular system $|1\rangle$ is the initial Feshbach state, $|2\rangle$ is the intermediate state in a higher electronic potential and $|3\rangle$ is the rovibrational ground state. Using the rotating the wave approximation, the Hamiltonian which governs this system is [130, 131]:

$$\hat{H} = \frac{\hbar}{2} \begin{pmatrix} 0 & \Omega_P(t) & 0 \\ \Omega_P(t) & 2\Delta_P & \Omega_S(t) \\ 0 & \Omega_S(t) & 2(\Delta_P - \Delta_S) \end{pmatrix}, \tag{7.2}$$

where Δ_P is the detuning of the pump beam from the $|1\rangle \rightarrow |2\rangle$ transition with an associated Rabi frequency of Ω_P and Δ_S is the detuning of the Stokes beam from the $|2\rangle \rightarrow |3\rangle$ transition with an associated Rabi frequency Ω_S. When the lasers are on resonance we obtain the following eigenvectors associated with this Hamiltonian:

$$\left|a^+\right\rangle = \begin{pmatrix} \sin\theta\sin\varphi \\ \cos\varphi \\ \cos\theta\sin\varphi \end{pmatrix} \left|a^0\right\rangle = \begin{pmatrix} \cos\theta \\ 0 \\ -\sin\theta \end{pmatrix} \left|a^-\right\rangle = \begin{pmatrix} \sin\theta\cos\varphi \\ -\sin\varphi \\ \cos\theta\cos\varphi \end{pmatrix}. \tag{7.3}$$

θ and φ are mixing angles defined by

$$\tan\theta = \frac{\Omega_P}{\Omega_S}, \tag{7.4}$$

and

$$\tan 2\varphi = \frac{\sqrt{\Omega_P^2 + \Omega_S^2}}{\Delta_P}. \tag{7.5}$$

The state $|a_0\rangle$ is a dark state with no component of $|2\rangle$ and only has a dependence on mixing angle θ. From Eq. 7.4 we can see that if we apply the lasers to the system initially such that $\Omega_P = 0$ and $\Omega_S >> 0$ then the entire population should be in $|1\rangle$. As we slowly ramp the laser intensity to approach the opposite extreme of $\Omega_P >> 0$ and $\Omega_S = 0$ then the population can be transferred from $|1\rangle$ to $|3\rangle$ without losing molecules to the $|2\rangle$ state.

Studying the time evolution with the master equation of the system, it can further be shown that if the laser pulses follow Gaussians appropriately separated in time such as shown in Fig. 7.2(a) then a solution to this equations exists such that the population can be coherently transferred from $|1\rangle$ to $|3\rangle$ as shown in Fig. 7.2(b) [130, 131] allowing near unity efficiency of transfer.

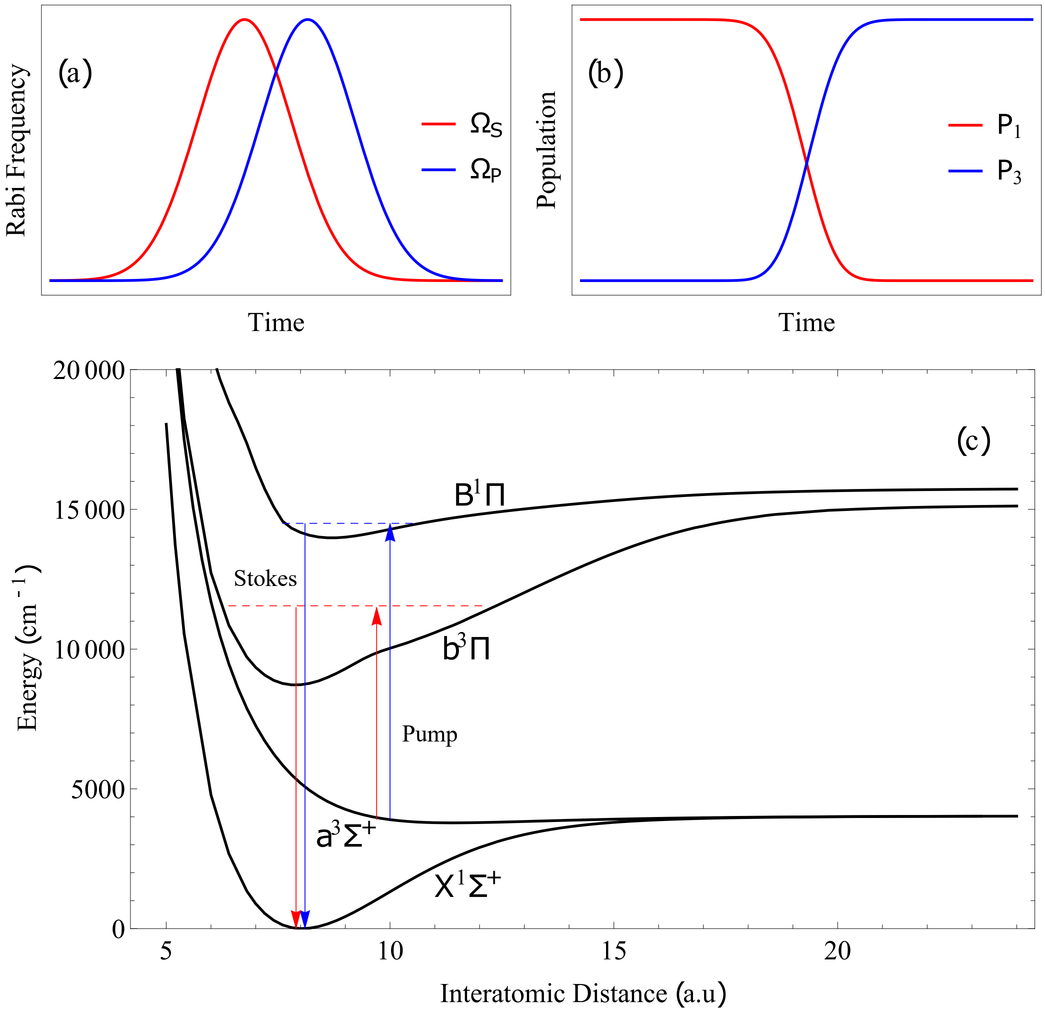

Figure 7.2: (a) Example of a pair of STIRAP pulses. The graph shows the Rabi frequency against time. (b) Population evolution as STIRAP pulses in (a) are applied. (c) Molecular potentials with possible STIRAP routes for KCs. Data aquired from [132]

.

Since it is impossible to ramp the laser intensities infinitely slowly then the process cannot be truly adiabatic. This, in addition to laser decoherence means the process is not 100 % efficient. The efficiency, P, is limited by the condition [133, 134]:

$$P = \exp\left(-\frac{\pi^2\Gamma}{\Omega_0^2\tau} - \frac{D\tau}{2}\right), \tag{7.6}$$

where $\Omega_0 = \sqrt{\Omega_P^2 + \Omega_S^2}$, Γ is the natural linewidth of $|2\rangle$, τ is the transfer time and D is the relative linewidth of the two lasers. We then need to act to minimise the two terms inside the exponential. This gives us the condition:

$$\frac{\Omega_0^2}{\pi\Gamma} \gg \frac{1}{\tau} \gg D. \tag{7.7}$$

From this, we then need a pair lasers which can produce high Rabi frequencies in addition to narrow linewidths and an intermediate state with a long lifetime. We can see then that the maximum intensity of the lasers is primarily what limits the linewidth.

Figure 7.2(c) shows selected molecular potentials for KCs with data acquired from [132]. These potentials show viable routes to the rovibrational ground state from the Feshbach state and gives us possible choices for $|1\rangle$, $|2\rangle$ and $|3\rangle$. It is important that the states $|1\rangle$, $|2\rangle$ are optically coupled and have good spatial overlap for a favourable transition dipole matrix element [132] and likewise for the $|2\rangle$ and $|3\rangle$ pair. We have opted to take the route through the $b^3\Pi$ potential. This requires lasers with wavelengths 1415 nm and 915 nm to drive the pump and Stokes transitions respectively. In addition, we will later use the same cavity to lock 977 nm and 1557 nm lasers for use in RbCs STIRAP. So the cavity will be used to lock to four wavelengths simultaneously.

7.2.2 Cs Rydberg

Rydberg atoms are atoms where the valence electron has been excited to a high principle quantum number [135]. Figure 7.3 outlines restricted energy level diagram relevant to the proposed Rydberg excitation scheme. We are using a three photon excitation scheme which follows $6S_{1/2} \rightarrow 6P_{1/2} \rightarrow 7S_{1/2} \rightarrow nP$ where n denotes a principal number in the Rydberg regime. Our excitation scheme is quite unusual in that we are exciting via the D_1 transition rather than the more commonly used D_2 transition. A third wavelength between 780 nm and 778 nm will be needed for a third excitation. Since 780 nm is used for Rb cooling then we already have plenty of frequency stabilised lasers near our needed wavelength. An offset locking mechanism, such as a transfer cavity, can be used to acquire the precise wavelength. The wavelengths for the more routinely used D_2 scheme will be out of range for the purpose bought KCs STIRAP lasers.

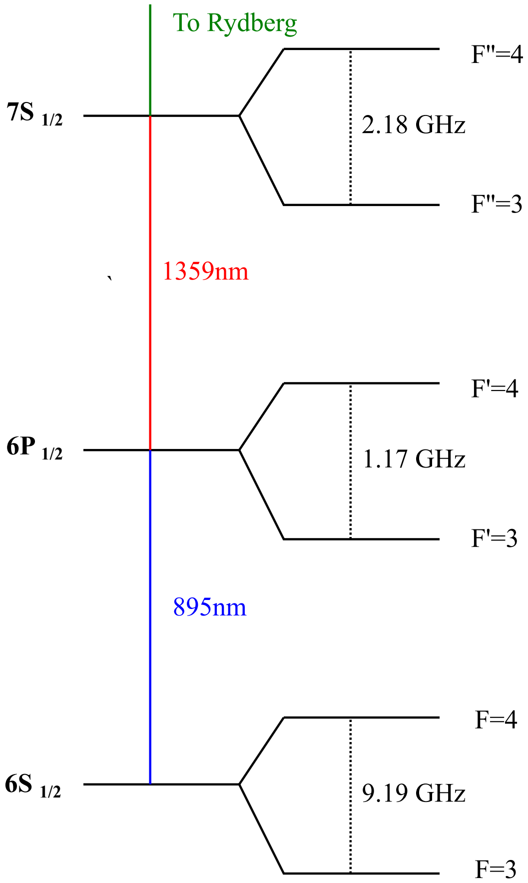

Figure 7.3: Energy level diagram for Rydberg excitation. Bold numbers listed left are the fine quantum terms. Coloured lines show wavelengths of transitions. Hyperfine splittings are shown. F is the hyperfine quantum number.

We lock to a cavity to allow for far detunings from the intermediate states. This helps minimise loss from spontaneous emission in these states but at the expense of not being able to lock to an atomic reference. Also, narrow linewidths are required to prevent laser induced dephasing [136]. These narrow linewidths should hopefully provide us with the necessary tools to study Rydberg atoms in the vicinity of a rovibrational ground state molecule and form a platform for novel experiments such as those discussed in [137] and [138].

7.3 Pound-Drever-Hall technique

7.3.1 Cavity Basics

The Pound-Drever-Hall (PDH) technique is implemented by locking a laser to an absorption feature produced by the spectrum of an optical cavity. The advantages of locking to a high finesse cavity are that the error signal has a very steep gradient which can be used to achieve sub kilohertz linewidth for frequency stabilisation and that the cavity peaks span wavelengths where there are no atomic or molecular references.

An optical cavity is, put briefly, two mirrors, each with a radius of curvature R_1 and R_2, separated by a distance L. Collectively R_1, R_2 and L must satisfy an optical stability criterion. Each mirror may allow a very low (typically less than 1 %) transmission. When a beam is incident on the outside surface of the mirror a small amount may enter the cavity. A beam whose wavelength is such that its electric field has nodes incident on the interior of both mirrors will resonate within the cavity. That is to say the laser's wavelength must satisfy:

$$\lambda = \frac{2L}{n}, \tag{7.8}$$

where n is an integer. This resonance causes destructive interference at the exterior of the entrance mirror and constructive interference at the exterior of the opposite mirror. This means a beam on resonance will appear to be transmitted through the cavity despite the mirrors' relatively low transmission. The frequency between different resonant modes of the cavity is given by:

$$\Delta f = \frac{c}{2L}. \tag{7.9}$$

We define this Δf as the free spectral range. However, all possible modes are not just trivially represented by the laser frequency. In addition to the frequency modes, both the longitudinal and transverse beam alignment can access various other modes of the cavity.

The behaviour of the beam inside the cavity must satisfy the paraxial wave equation [139]:

$$\left(\boldsymbol{\nabla}_{x,y}^2 - 2ik\frac{\partial}{\partial z}\right) E(x,y,z) = 0. \tag{7.10}$$

This equation has solutions:

$$E(x,y,z) = E_0 H_m\left(\frac{\sqrt{2}x}{w(z)}\right) H_p\left(\frac{\sqrt{2}y}{w(z)}\right)\frac{w_0}{w(z)} e^{\frac{-x^2-y^2}{w(z)^2}} \times e^{-i\left(kz-(1+m+p)\tan^{-1}\left(\frac{z}{z_0}\right)\right)} e^{-i\frac{k(x^2+y^2)}{2R(z)}}. \tag{7.11}$$

Here, E_0 is the amplitude of the electric field, H_m is the m^{th} Hermite polynomial, x and y are the horizontal and vertical displacement from the optical axis, z is the displacement along the optical axis, k is the wave-vector of the beam and w_0 is the beam waist. In addition, the beam radius at a given point $w(z)$, the wavefront curvature $R(z)$ and the Rayleigh range z_0 are defined as:

$$w(z) = w_0\sqrt{1+\left(\frac{z}{z_0}\right)^2}, \tag{7.12}$$

$$R(z) = z\left(1+\left(\frac{z_0}{z}\right)^2\right), \tag{7.13}$$

and

$$z_0 = \frac{\pi w_0^2}{\lambda}. \tag{7.14}$$

Breaking down Eq. 7.11, we have three distinct parts to interpret:

$$H_m\left(\frac{\sqrt{2}x}{w(z)}\right) H_p\left(\frac{\sqrt{2}y}{w(z)}\right), \tag{7.15}$$

represents the Hermite modes of the cavity. When the longitudinal and transverse alignment of a Gaussian beam into the cavity is sufficiently good, these modes will largely vanish leaving us with the single TEM_{00} ($m = 0$

and $p = 0$) mode which is also itself a typical Gaussian beam. That is to say $H_0 = 1$ for all x, y and z. It is this mode we wish to aim for to lock the laser.

$$\frac{w_0}{w(z)} e^{\frac{-x^2-y^2}{w(z)^2}}, \tag{7.16}$$

can be interpreted as the Gaussian propagation of the beam. This part means the beam will still diverge in a similar fashion to a standard Gaussian beam. Finally:

$$e^{-i\left(kz-(1+m+p)\tan^{-1}\left(\frac{z}{z_0}\right)\right)} e^{-i\frac{k(x^2+y^2)}{2R(z)}}, \tag{7.17}$$

adds an additional phase shift for each mode of m and p. A pair of TEM$_{00}$ modes will be separated in frequency by a free spectral range. The other modes of the cavity are separated in frequency by:

$$\Delta f_{n,m,p} = \frac{c}{2L}\left(n + (m+p+1)\frac{\cos^{-1}\sqrt{g_1 g_2}}{\pi}\right), \tag{7.18}$$

where g_i is a property of the cavity and reflecting surface defined by:

$$g_i = 1 - \frac{L}{R_\mathrm{i}}, \tag{7.19}$$

where R_M is the radius of curvature of the mirror.

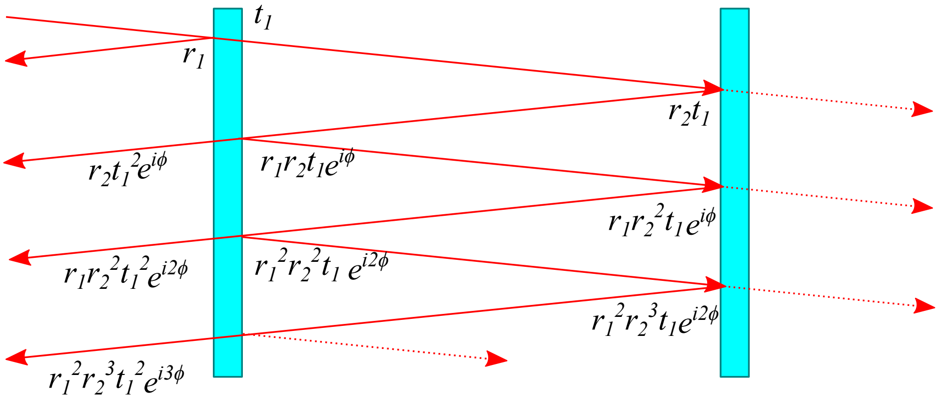

Figure 7.4: Illustration of the electric field of the laser evolves with each round trip of the cavity. The amplitude of the field as a fraction of the initial amplitude is shown with each reflection and transmission. Every time the first mirror is hit a small amount is re-transmitted back in the direction from where the beam came. The angles of reflection are exaggerated for clarity.

In the PDH system, we use the reflected signal to stabilise the laser. Figure 7.4 can be used to best understand the reflected signal of the cavity. Only a fraction of t_1 of the initial beam incident on the cavity passes through the first mirror. This hits the opposite mirror only to be reflected back. It is important to note that with each pass through the cavity the beam will undergo a phase shift of $\phi = 2\pi\frac{2L}{\lambda}$ and as such a phase factor of $e^{i\phi}$ is added to our E-field.

At this point, when the beam interacts with the entry mirror again it will transmit a portion with a fraction of $t_1^2 r_2 e^{i\phi}$ of the initial amplitude and a portion $t_1 r_2 r_1 e^{i\phi}$ will be sent for another trip around the cavity. The next transmitted beam has a factor of $r_1 r_2^2 t_1^2 e^{i2\phi}$. It should be obvious that each round trip adds a factor of $r_1 r_2 e^{i\phi}$ to the transmitted coefficient. In effect, the beam reflected from the cavity is then the sum of all of these reflected beams, including the initial reflection. It then follows:

$$E_r = E_{\text{inc}} \left(-r_1 + t_1^2 r_2 e^{i\phi} \sum_{n=0}^{\infty} \left(r_1 r_2 e^{i\phi} \right)^n \right). \tag{7.20}$$

This is just a geometric series so can be simplified to:

$$E_r = E_{\text{inc}} \left(-r_1 + \frac{t_1^2 r_2 e^{i\phi}}{1 - r_1 r_2 e^{i\phi}} \right). \tag{7.21}$$

If we let $r_1 = r_2 = r$ and $t = 1 - r$ then we can reduce this equation to:

$$\frac{E_r}{E_{\text{inc}}} = r \frac{e^{i\phi} - 1}{1 - r^2 e^{i\phi}}. \tag{7.22}$$

The intensity of the reflected light is proportional to the square of the electric field (i.e. $I_r \propto |E_r|^2$). We can express the intensity in terms of the airy function:

$$\frac{I_t}{I_{\text{inc}}} = 1 - \frac{I_r}{I_{\text{inc}}} = \frac{1}{1 + \frac{2r^2}{(1-r^2)^2}(1 - \cos\phi)}. \tag{7.23}$$

Figure 7.5 shows how the transmission of the cavity varies as a function of the phase evolution. The finesse of the cavity is defined as the ratio of the free spectral range, Δf, and the full width at half maximum $\Delta\nu$. A high finesse

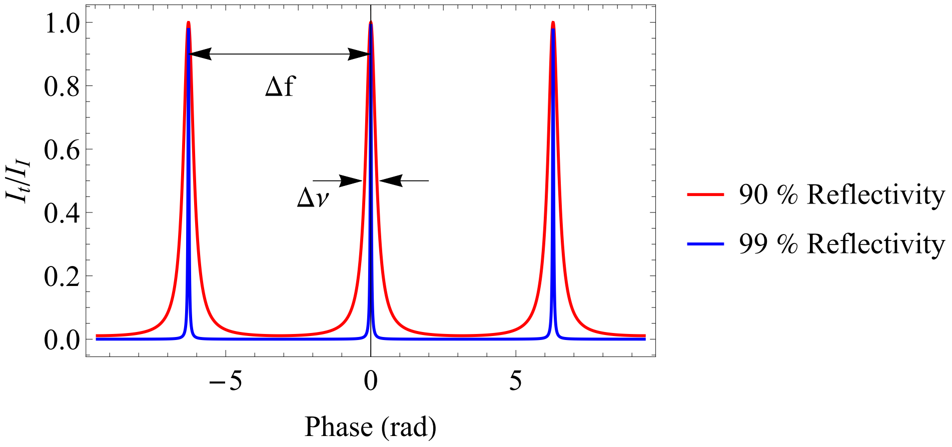

Figure 7.5: Simulated cavity transmission as a function of the phase of the incident light. The red line shows the transmission at 90 % reflectivity and the blue line shows the transmission at 99 % reflectivity. Δf denotes the free spectral range of the cavity as a function of the phase evolution. Each free spectral range occurs every 2π. $\Delta\nu$ shows the full half at maximum of the red line.

cavity, greater than 10000, is desirable for our purposes as it will provide the steepest slope for the error signal used in Pound-Drever-Hall locking.

7.3.2 Pound-Drever-Hall Theory

A laser beam with carrier frequency, ω_c, can be modulated to add sidebands to its spectrum. Usually the modulation is done by phase modulation with an electro-optical modulator (EOM). We can write the electric field describing the laser after the modulator as:

$$\begin{aligned} E &= E_0 e^{i(\omega_c t+\beta\sin(\omega_m t))} \\ &= E_0(J_0(\beta)e^{i\omega_c t} + J_1(\beta)e^{i(\omega_c+\omega_m)t} - J_1(\beta)e^{i(\omega_c-\omega_m)t}), \end{aligned} \tag{7.24}$$

where E_0 is the amplitude of the electric field, J_n is the nth order Bessel function, ω_c is the carrier frequency, ω_m is modulation frequency and β is the modulation depth determined by the driving voltage of the EOM [140]. Using the fact that the phase shift of a reflected beam is $\phi = 2\pi\frac{2L}{\lambda} = \frac{\omega}{\Delta\omega_{\text{fsr}}}$ we can rewrite Eq. 7.22 into the function:

$$F(\omega) = r\frac{e^{i\omega/\Delta\omega_{\mathrm{fsr}}} - 1}{1 - r^2 e^{i\omega/\Delta\omega_{\mathrm{fsr}}}}. \tag{7.25}$$

It then follows that the reflected beam from the cavity is:

$$\begin{aligned} E_r = E_0(F(\omega_c)J_0(\beta)e^{i\omega_c t} + F(\omega_c + \omega_m)J_1(\beta)e^{i(\omega_c+\omega_m)t} \\ - F(\omega_c - \omega_m)J_1(\beta)e^{i(\omega_c-\omega_m)t}), \end{aligned} \tag{7.26}$$

The photodiode detects the signal $P \propto |E_r|^2$. This results in the sum of two expressions, one multiplied by $\cos(\omega_m t)$ (in-phase component) and a second multiplied by $\sin(\omega_m t)$ (quadrature component) in addition to terms oscillating at $2\omega_m$. We can use a mixer to multiply the photodiode signal by a local oscillator to demodulate the in-phase component and use a low pass filter to remove any remaining oscillating terms. The resulting error signal is:

$$S = -2\sqrt{P_c P_m}(F(\omega_c)F^*(\omega_c + \omega_m) - F^*(\omega_c)F(\omega_c + \omega_m)), \tag{7.27}$$

where $F^*(\omega)$ denotes the complex conjugate of $F(\omega)$, P_c is the power driven into the carrier and P_m is the power driven into the sideband. The signal provides steep slopes which makes it suitable for narrow laser linewidth locking. The error signal may be provided by the imaginary part of Eq. 7.27, a simulation of which is shown in Fig. 7.6 for finesses of 2200 and 15000. This makes it clear the importance of the role of finesse in the error signal generation.

7.4 The Cavity

The cavity we have used for locking is an ultra-low expansion high finesse cavity manufactured by Stable Laser Systems. Figure 7.7 shows an image of the cavity in its open vacuum chamber. It is a hemispherical cavity. The cavity rests on a small polymer surface and is concentric with the vacuum chamber. The vacuum chamber itself has two viewports for optical access and aids in the temperature stabilisation of the cavity. An ion pump maintains

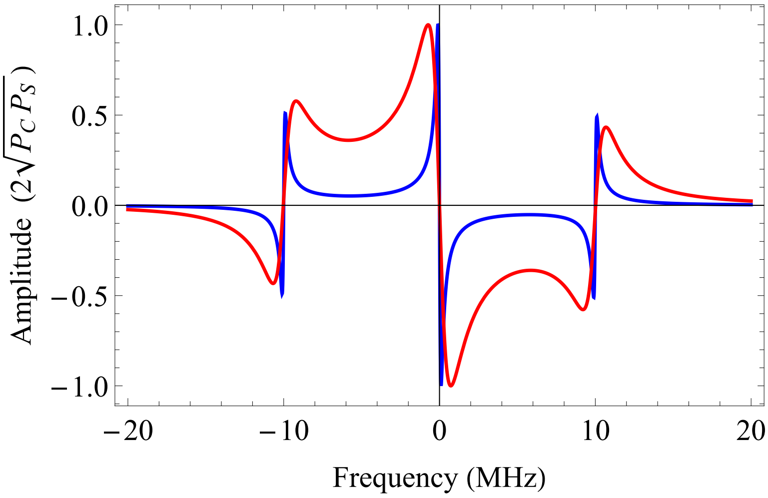

Figure 7.6: Simulation of the imaginary component of Eq. 7.27. The red line shows the simulation at a finesse of 2200 and the blue line shows the simulated signal at a finesse of 15000. The modulation frequeny is 10 MHz.

the vacuum at a pressure of 1.8×10^{-7} mbar. The cavity is 50 mm in diameter and 100 mm in length. It has a specified free spectral range of 1.5 GHz. One of the cavity mirrors is curved with a radius of curvature of 500 mm and the other side is flat. The zero crossing temperature, the temperature at which the cavity's thermal expansion is minimised, is 30.1°C.

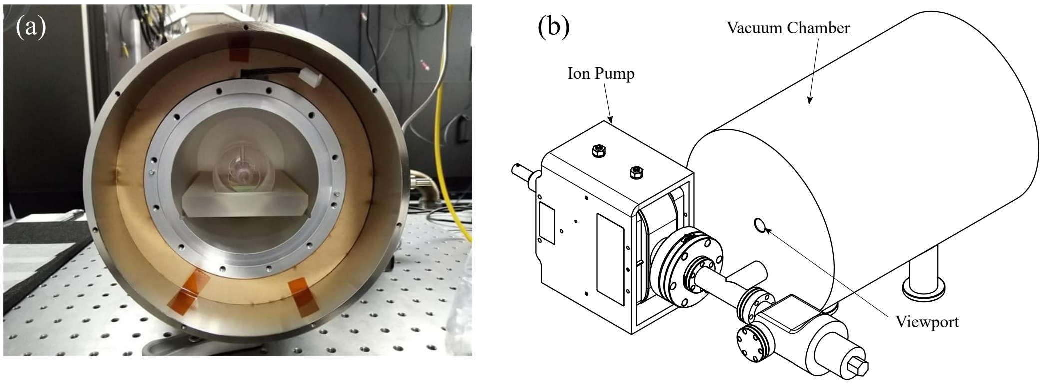

Figure 7.7: (a) Photograph of cavity mounted inside open vacuum chamber. (b) Diagram of the cavity vacuum chamber.

The reflectivity of the dielectric coating on the mirrors is shown in Fig. 7.8 as a function of wavelength. The cavity's reflective coating is specifically optimised for the critical wavelengths for STIRAP but the coating coincidentally extends to the wavelengths needed for Cs Rydberg applications. The transmittance and reflectivity of the coatings are critical in determining the

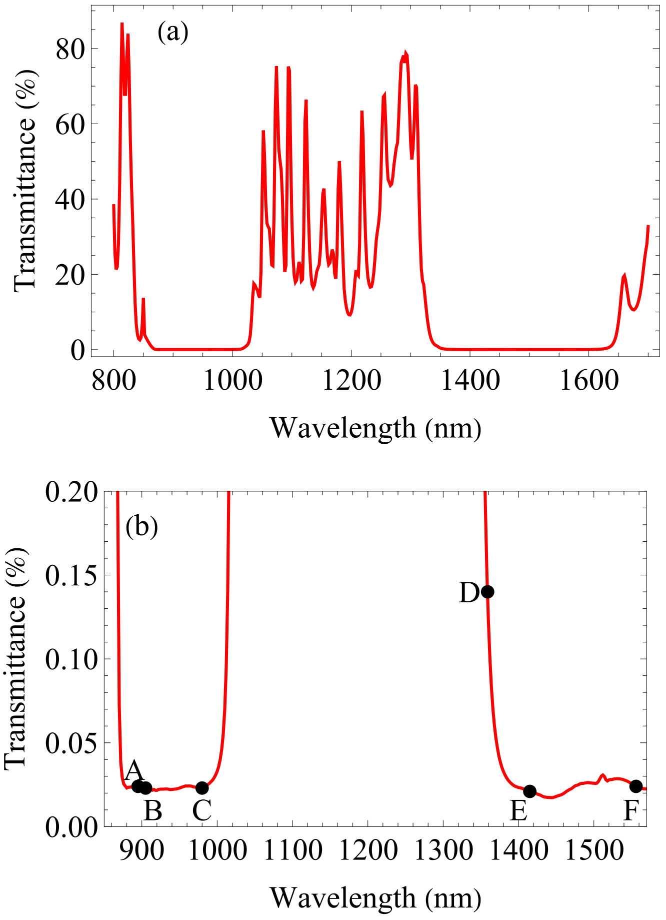

Figure 7.8: Specified transmittance curve of the cavity. (a) Transmittance curve from 790 nm to 1650 nm. (b) Transmittance curve between 850 nm and 1550 nm. Six key wavelengths of interest are labelled: A at 895 nm, B at 915 nm, C at 977 nm, D at 1359 nm, E at 1415 nm and F at 1557 nm.

finesse of the cavity and are related by:

$$\mathcal{F} \approx \frac{\pi\sqrt{r}}{1-r}, \tag{7.28}$$

where r is the refelctivity which we assume is related to the transmittance, t by $1-t$. Table 7.1 shows the estimated finesse based on the transmittance curve provided by the manufacturer. For STIRAP applications our lasers require a linewidth on the order of less than a kHz [26, 141]. As such, finesses on the order of 10000 or greater are required at these wavelengths. We have a high finesse for exciting the D_1 transition of Cs but the $6P_{1/2} \rightarrow 7S_{1/2}$ transition has a lower finesse due the wavelength being on the edge of the low transmittance region. However, for Rydberg excitations the Rydberg states are separated by an order of hundreds of kHz so linewidths on the order tens of kilohertz should be sufficient.

Point on Fig. 7.8	Wavelength	Transmittance	Reflectivity	Finesse
A	895 nm	0.024 %	99.976 %	13088
B	915 nm	0.023 %	99.977 %	13657
C	977 nm	0.023 %	99.977 %	13675
D	1359 nm	0.14 %	99.86 %	2242
E	1415 nm	0.021 %	99.979 %	14958
F	1557 nm	0.024 %	99.976 %	13088

Table 7.1: Table detailing calculated cavity characteristics at the key wavelengths of interest. Based on the transmittance curve provided by the manufacturer. Also shown are the values for RbCs STIRAP as well (C and F).

7.5 Laser Stabilisation

7.5.1 Schematic

A schematic for the laser setup used for stabilisation and controlling the pulses of light is shown in Fig. 7.9. The lasers used are Toptica DL Pros. The pump laser diode covers the wavelengths 1350 nm to 1425 nm. The Stokes laser diode covers the wavelengths 880 nm to 950 nm making both lasers suitable for use in coupling the first two energy levels of the Cs Rydberg system and performing STIRAP at the predicted wavelength for KCs molecules.

Light for the cavity is sampled with glass wedges. This light is then coupled into a fibre EOM. The EOMs are EOspace models PM-0S5-10-PFA-PFA-900 for the Stokes laser and PM-0S5-10-PFA-PFA-1420 for the pump laser. Both EOMs are mounted and housed within an aluminium asing along with the fibre coils to maintain the polarisation of the laser and stability of the EOM. The power of the pump and Stokes lasers at the output of their EOMs are 855 µW and 448 µW respectively. However, feedback to the pump laser from

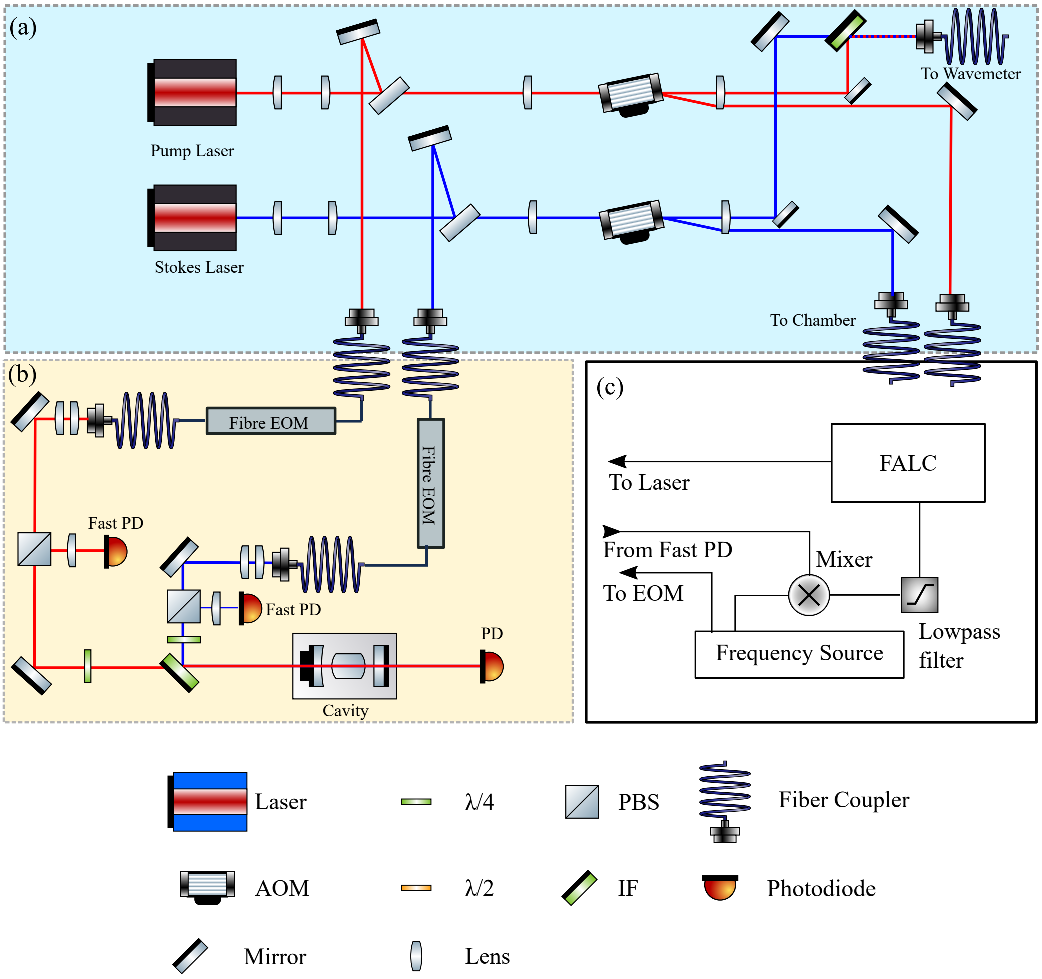

Figure 7.9: A schematic of the setup for locking the STIRAP/Rydberg lasers and passing them onto the main chamber. (a) The main setup. For both lasers we use a glass blank to sample the beam for the locking. This sample is coupled into the EOM. The remainder of the light is passed through an AOM which will be modulated to deliver the STIRAP pulse. The zeroth order of the AOM is passed through to the wavemeter for diagnostics. (b) The cavity setup: both lasers leave the EOM fibre and pass through a lens cage system specifically optimised to produce the correct waist size on the plane mirror of the cavity. Both lasers are overlapped on a dichroic before entering the cavity. Fast photodiodes are used to record the reflected cavity signal. A third photodiode is used to view the transmission but this is not used to for locking. (c) The electrical setup for one beam. The frequency source is used to drive the EOM. It also sends a signal to a mixer which is used as a reference. The mixer multiplies the reference and the output of the photodiode which is the passed through a low pass filter for demodulation and finally onto a Toptica FALC which contains the PID electronics for laser locking. The output is sent to the laser for feedback. An identical setup is used for both lasers.

the cavity was visible on the signal so we have reduced the pump power into the cavity to 170 µW until an optical isolator can be sourced. A pair of fast photodiodes are used to detect the reflected signal from the cavity. These are Thorlabs model PDA05CF2.

7.5.2 Lens Cage System

To mode-match the laser to the TEM_{00} mode we need the appropriate beam waist at the plane mirror. This is determined predominantly by the radius of curvature of the curved mirror. The beam can be mode matched to the cavity by setting the radius curvature of the beam at the curved mirror equal to the radius of curvature of the mirror. From Eq. 7.13 we can use $R(L) = R_{\mathrm{M}}$ where R_M is the radius of curvature of the mirror. With Eq. 7.14 we can thus determine the needed beam waist to be:

$$w_0 = \frac{\sqrt[4]{4LR_{\mathrm{M}} - L^2}}{\sqrt{k}}. \tag{7.29}$$

This results in a waist value of 239 µm for the 895nm beam and 294 µm for the 1359 nm beam. The output collimator of the EOM fibre feeds directly into a cage system consisting of the collimator itself and a pair of lenses. To ensure that we choose an appropriate pair lenses for the cavity: python code, developed by Daniel Ruttley and adapted for our cavity system, was used. The associated calculations are shown in Fig. 7.10. Extra constraints such as the space available were also factored into this. For the 895 nm we found the best lenses to match were $f_1 = 100$mm and $f_2 = -100$mm with a Thorlabs collimator F240APC-850. For the 1359nm beam we find that $f_1 = 100$mm and $f_2 = -75$ combined with F220APC - 1310 collimator is best.

The lens pair in the cage were separated at the distance needed to achieve the desired beam waist. The final positions deviated slightly from the values calculated in Fig. 7.10. For the 895nm we obtained a waist of 240(2) µm at 400(10) mm form the second lens. For the 1359 nm we obtained a waist of 288(5) µm at a distance of 810(10) mm from the 2nd lens.

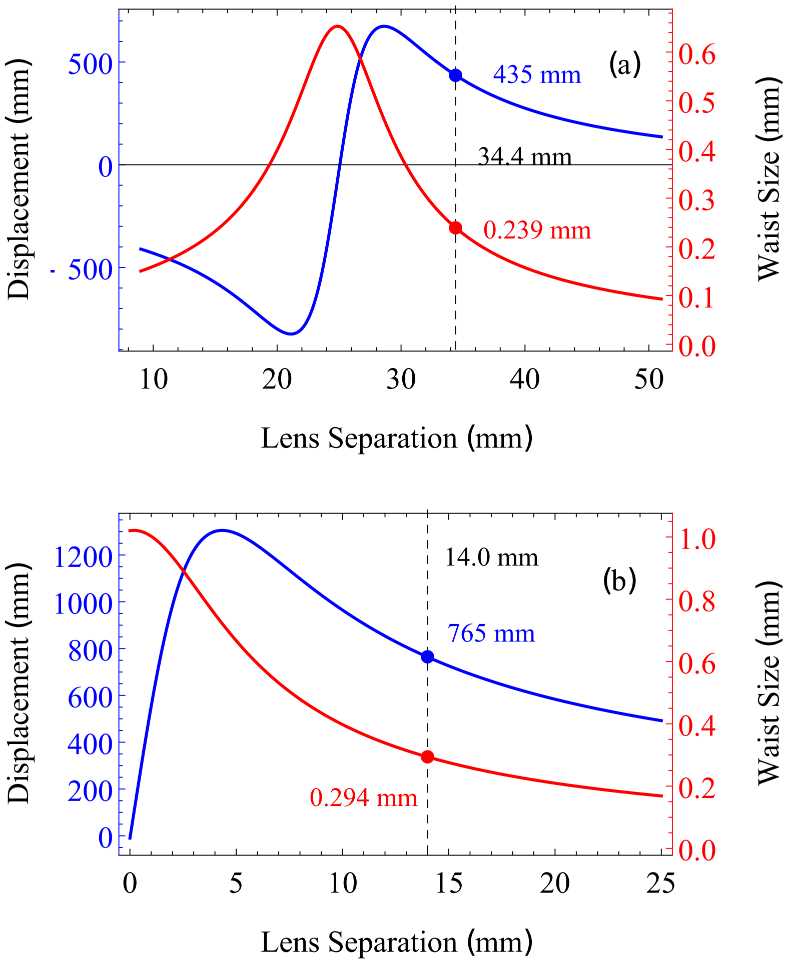

Figure 7.10: Lens pairing calculations for coupling into the cavity. The blue curve, associated with the left axis, shows the distance between the 2nd lens and the beam waist as function of the lens pair separation. The red curve shows the beam waist as a function of the lens separation. The black number and dashed line shows the lens separation value needed to obtain the correct waist. (a) For wavelength 895 nm and lens pairs 100 mm and −100 mm (b) For wavelength 1359 nm and lens pairs 100 mm and −75 mm.

7.5.3 Cavity Spectrum

The cage system is positioned and the pair of mirrors after are aligned to the cavity to obtain the TEM_{00} mode. Figure 7.11 shows the transmission spectrum of the cavity as a function of the ECDL's piezo voltage. Given the finesse of the cavity and the laser scan speed, the data acquisition rate limits the time spent on each peak during a laser scan so the amplitudes of the peaks will appear quite 'jittery' at this time.

We note that in the case the lasers are well aligned only a few equally spaced peaks are present. This is the TEM$_{00}$ mode. the laser is less well aligned, the strength of the TEM$_{00}$ drops and additional modes appear. These are the modes with $p \neq 0$ and $m \neq 0$ and are the modes that we wish to eliminate as far as possible.

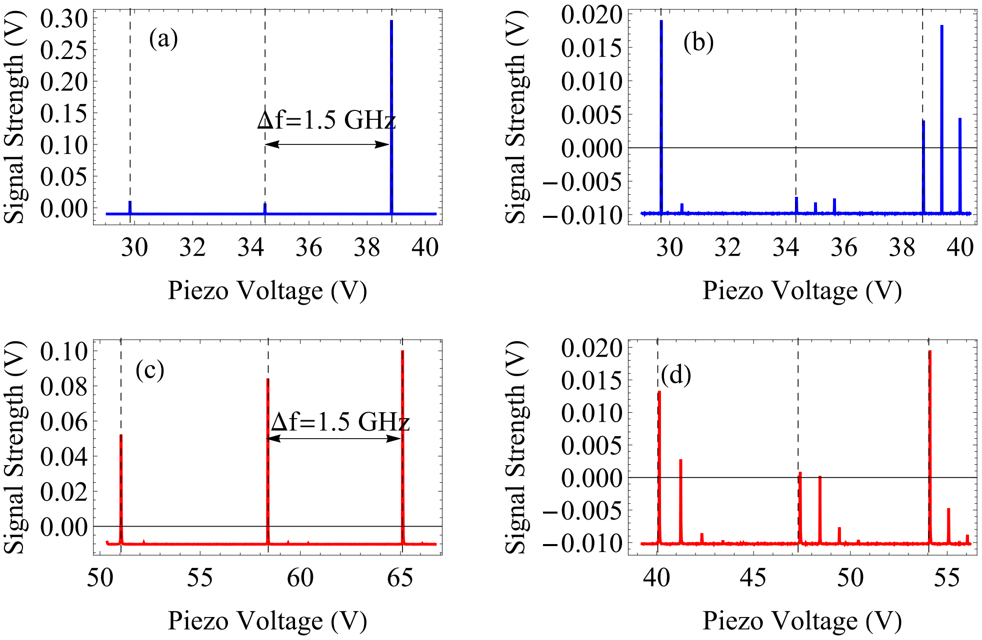

Figure 7.11: Measured cavity transmission spectrum as a function of the ECDL piezo voltage for (a) 895 nm well aligned, (b) 895 nm poorly aligned, (c) 1359 nm well aligned and (d) 1359 nm poorly aligned. The dashed lines show the positions of the cavity peaks assoiated with the TEM$_{00}$ mode. A free spectral range is also indicated on the well aligned figures.

With the cavity well aligned the peaks are spaced by approximately 1.5 GHz but the precise value is characterised later in the chapter when the lock is optimised. The precise value of the free spectral range depends on how deep the laser beam penetrates the reflective coating which will also be wavelength dependent.

7.5.4 EOM Characterisation

We note that from Eq. 7.27 that the power in the carrier and sidebands are respectively:

$$P_c \propto J_0(\alpha)^2, \tag{7.30}$$

and

$$P_m \propto J_1(\alpha)^2, \tag{7.31}$$

where α is the modulation index of the EOM. Therefore the error signal:

$$S \propto J_0(\alpha)J_1(\alpha). \tag{7.32}$$

As we increase the driving power into the EOM more laser power is split from the carrier into the sidebands. However, it is possible to overdrive the EOM. This would result in power being lost to higher order sidebands which will weaken the error signal. The optimal driving voltage is the voltage such that $J_0(\alpha)J_1(\alpha)$ is maximum. This corresponds to a modulation index of $\alpha = 1.082$.

We measure the sideband strength as a function of EOM driving voltage using the cavity transmission signal. From this we can characterise the sideband to carrier height ratios:

$$\text{Ratio(V)} = \frac{J_1(\beta V)^2}{J_0(\beta V)^2}, \tag{7.33}$$

where β is a linear conversion factor from driving voltage to modulation index. We can then extract the apprioriate voltage to drive the EOM for the optimal signal.

Wavelength	**895 nm**	**1359 nm**
β	0.267(2) V^{-1}	0.165(5) V^{-1}
Optimal Driving Voltage (V)	4.05(3) V	6.5(2) V

Table 7.2: Parameters extracted from EOM chacterisation. β is a conversion of driving voltage to modulation index. Optimal driving voltage where $J_1(\alpha)J_0(\alpha)$ is maximum.

Figure 7.12(a) shows an example of a measured transmission signal from the cavity with the EOM active. The central peak is the carrier and the two smaller peaks to either side are the sidebands. We fit three Lorentzians to

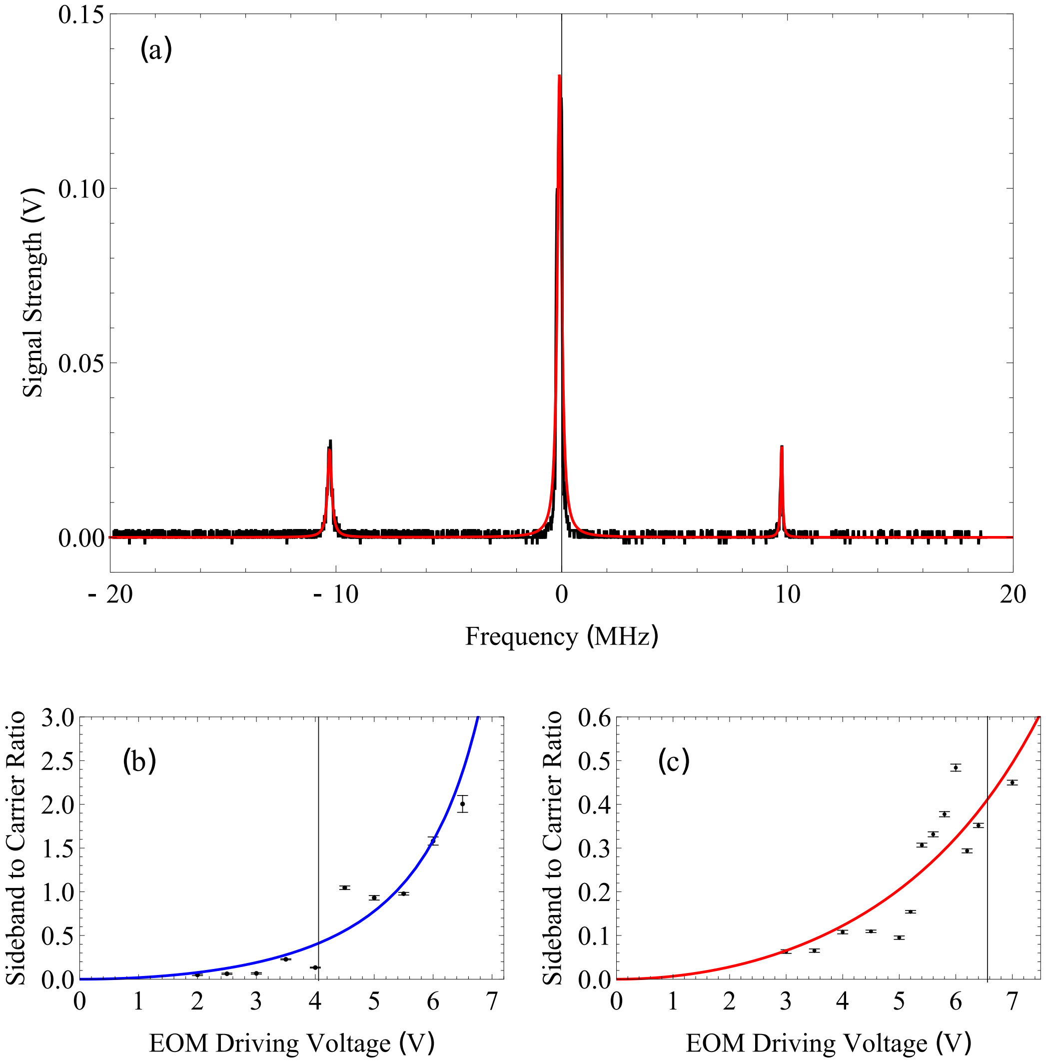

Figure 7.12: (a) Example transmission signal for 895 nm at a driving signal of 10 MHz at a driving voltage of 4 V. The black trace shows the data and red curve shows the fitted Lorentzian functions (red). (b) Sideband ratio vs EOM driving voltage for 895 nm and fitted ratio function. Black vertical lines the shows the voltage needed for the optimal locking condition $\alpha = 1.084$. (c) Sideband ratio vs EOM driving voltage for 1359 nm.

this data to extract the peak heights, and obtain the ratio. The sideband height is taken as the average height of the two sidebands.

Figure 7.12(b) and (c) shows the measured ratios as a function of driving voltage and the fit of Eq. 7.33. From these fits we obtain the parameters shown in table 7.2. The data are quite noisy since the high finesse of the cavity so the oscilloscope doesn't always sample the peak accurately.

7.5.5 Error Signal and Locking

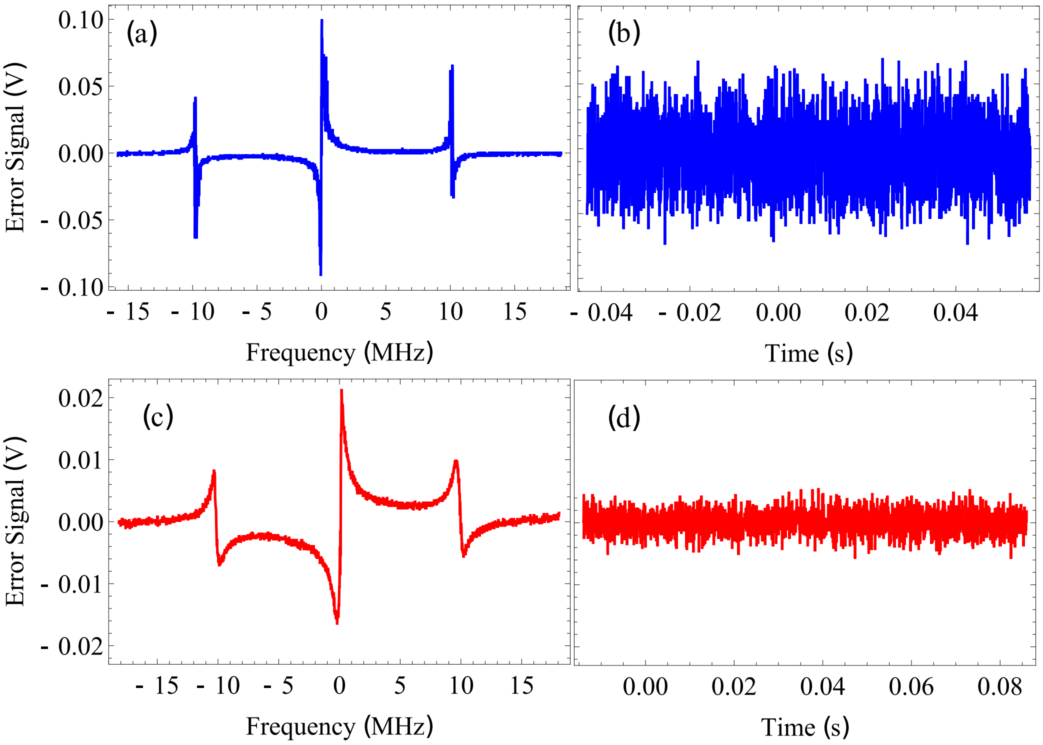

Figure 7.13: Measured error signal trace for (a) 895 nm and (b) 1359 nm. Error signal when laser is locked for (c) 895 nm and 1359 nm (d).

Figure 7.13 (a) shows the error signal trace for the 895 nm laser at the optimal sideband carrier ratio and phase. The laser can be locked to the slope in the centre.

The locking is done by simply turning on the Toptica FALC and then switching the laser scan off. When the lock is applied Fig. 7.13(b) shows the error signal of the laser in time. There are PID parameters on the FALC which are used to reduce the amplitude of residual noise shown in Fig. 7.13(b) as much as possible.

Normally the quality of the laser stability is measured using a self-heterodyne measurement. This measurement is done by beating the laser signal against itself. The beam is split and one beam is delayed by sending it through an optical fibre, However, this would require a fibre of length greater than 100 km since this is the coherence wavelength associated with 1 kHz. Alternatively a single short fibre can be looped with an amplifier. We have neither an amplifier nor a long fibre. We can roughly estimate the linewidth of the laser using Fig. 7.13(b). By extracting the gradient of the central slope in Fig. 7.13(a) we obtain a voltage to frequency conversion factor for our scope trace. Then we divide the standard deviation of the data in Fig. 7.13(b) by this factor. The slope in Fig. 7.13(a) is 2.5(4) V MHz^{-1} and the standard deviation in 7.13(b) is 0.00273 V. So an estimate on the linewidth is 10(2) kHz. The same analysis in figures 7.13(c) and (d) gives an estimated linewidth of 11.5(1.1) kHz for the 1359 nm laser. We should note that the broadening exhibited by the 1359 nm laser is to be expected due to the lower finesse of the cavity at this wavelength. These linewidths should be sufficiently small to allow for Rydberg excitations.

7.5.6 Cavity Characterisation

We can more accurately measure certain characteristics of the cavity now that we have locked the lasers. In addition to the sidebands needed for PDH locking, we can also drive an additional pair sidebands on a much larger modulation depth and over the order of GHz to move the lock signal over the free spectral range of the cavity. These sidebands are driven by a Windfreak Synth HD and are combined with the PDH sidebands. A Windfreak Synth HD is a microwave source capable of producing up to 15 GHz with 20 dBm of power. It can also use GPS as a reference against which its frequencies are generated.

To characterise the cavity we activate the Windfreak. Doing so splits the transmission signal into a static carrier and two sidebands separated from the carrier by a frequency f_{mod}. This is demonstrated in Fig. 7.14(a). The laser can be locked to the central carrier or to the sidebands meaning we can adjust the laser frequency, as oppose to being restricted to arbitrary cavity peaks.

In this measurement we first lock the laser to the carrier. The additional pair of sidebands will be incident on the cavity but will be reflected. When $f_{\mathrm{mod}} \approx \Delta f$ the sidebands will intercept the next pair of frequency modes of the cavity and will thus be transmitted. We can measure the total transmission of the cavity here whilst varying f_{mod} and the result will be a Lorentzian lineshape which we can subsequently use to accurately characterise the cavity

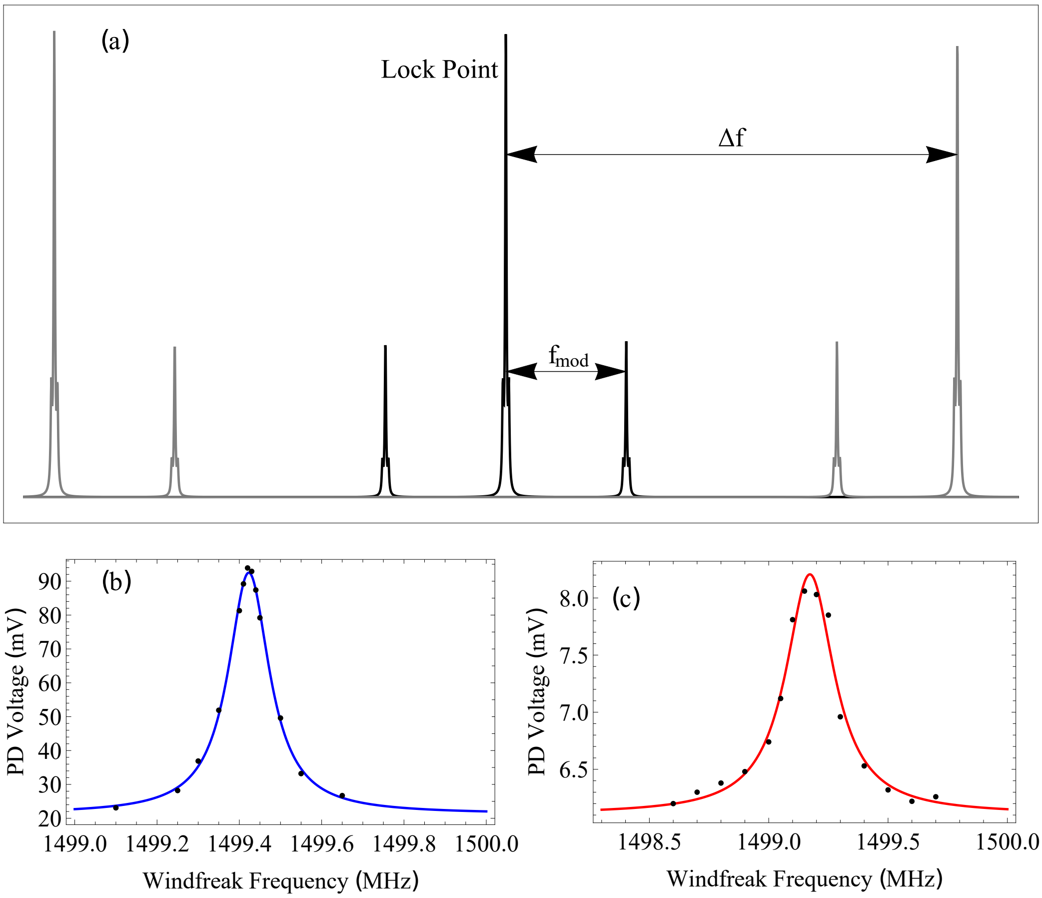

Figure 7.14: (a)Model cavity transmission spectrum with the Windfreak microwave source driver active. Transmission strength as a function of EOM Windfreak driving frequency. (b) 895 nm laser and (c) 1359 nm. Black points are data points and curves are Lorentzians fitted to the data.

for the used wavelengths. The fact that the laser is locked is critical to this measurement. The frequency stabilisation means it will have a significantly lower linewidth than the cavity peaks meaning that the laser's frequency profile can be effectively treated as a delta function in frequency space. If we were to simply scan the laser across these peaks then we would instead measure the convolution of the cavity and the laser's linewidths.

The data gathered are fitted to a Lorentzian of the form:

$$\mathrm{Signal}(f) = \frac{A}{(f - \Delta f)^2 + \left(\frac{\Gamma}{2}\right)^2} + B, \tag{7.34}$$

where A is the amplitude, B is the background and Γ is the full width half maximum of the Lorentzian. Figure 7.14(b) and (c) shows the results obtained for the 895 nm and 1359 nm respectively. Table 7.3 shows the obtained parameters.

	895 nm	**1359 nm**
A	0.27(2) mV	0.032(6) mV
Γ	112(5) kHz	250(20) kHz
Δf	1499.420(1) MHz	1499.170(5) MHz
B	21.1(1.1) mV	6.10(6) mV

Table 7.3: Results of the characterisation of the cavity for the two wavelengths.

We interpret the Lorentzian centre, Δf, as the free spectral range of the cavity. These are not quite equal for different wavelengths. This can be owed to the fact the depth of penetration into the reflective coating for each wavelength will be slightly different resulting in different values for L. Indeed using Eq. 7.9 we find the 'true' lengths of the cavity to be: $L_{895\text{ nm}} = 100.03868(7)$ mm and $L_{1359\text{ nm}} = 100.0553(3)$ mm.

Since the linewidth of the laser is significantly less than the linewidth of the cavity then the values of Γ obtained are a good estimate of the linewidth of the cavity. It is possible to obtain the finesses of the cavity and compare them against the manufacturer specified values in table 7.1. The finesse is related to the linewidth by:

$$\mathcal{F} = \frac{\Delta f}{\Gamma}. \tag{7.35}$$

This gives us finesses of $\mathcal{F}_{895\text{ nm}} = 12000(500)$ and $\mathcal{F}_{1359\text{ nm}} = 6000(500)$. The finesse appears to be better than the manufacturer's specifications for 1359 nm but slightly worse for 895 nm. For comparison the specified finesses, based on the reflectivity, are 13088 and 2242 for 895 nm and 1359 nm respectively. It is also worth noting that 1359 nm lies on the edge of the coating for which the finesse can be difficult to predict.

7.6 Cs Spectroscopy

This final section of the chapter will present a study of two-photon processes in a Cs cell. We study the spectrum and present evidence that the lasers are capable of driving the transition: $6S_{1/2} \rightarrow 6P_{1/2} \rightarrow 7S_{1/2}$ which in the future we can use to access Rydberg states.

7.6.1 Schematic

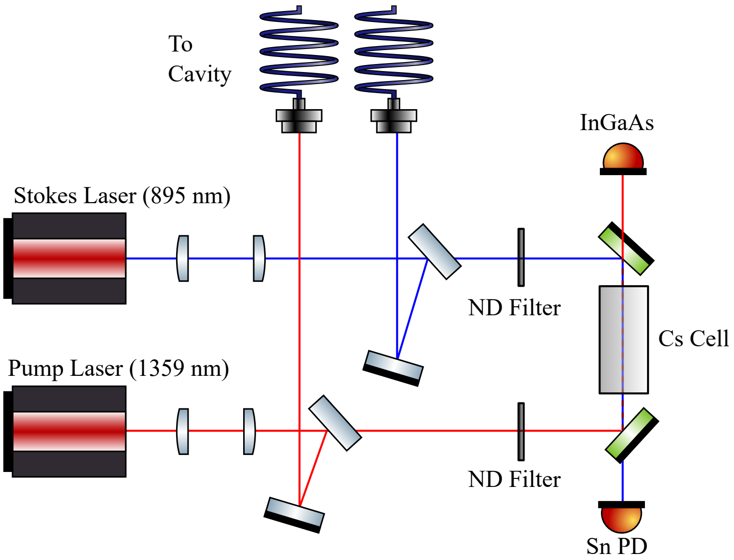

Figure 7.15: Laser layout for taking two-photon spectroscopy measurements. The pickoff to the cavity is still in place. The two AOMs for pulse intensity control have been temporarily replaced with Cs cell. The two beams are overlapped in the Cs cell, propagating in opposite directions. Each beam is detected and the trace data acquired by a photodiode. ND filters are in place to control the intensity of the beams.

Figure 7.15 shows a temporary laser setup for acquiring the room temperature spectroscopy data of Cs. A sample from each beam is still sent to the cavity for locking. The AOMs that would otherwise have been used for pulse control in the main experiment have been replaced with a Cs cell. The two beams are overlapped with a pair of dichroics. A 6 cm Cs cell is placed on the region of overlap. The 895 nm has a radius of 0.90(6) mm and the 1359 nm beam has a radius of 0.82(3) mm at the centre of the cell. It should be noted since the beam shapes have not bean ‘cleaned’ with a fibre at this stage the beams are not necessarily Gaussian.

Variable ND filters have been placed in the path of each beam to vary the power to the cell. A pair of photodiodes are used to detect the absorption signal from the cell for each beam.

7.6.2 Single Photon Spectroscopy

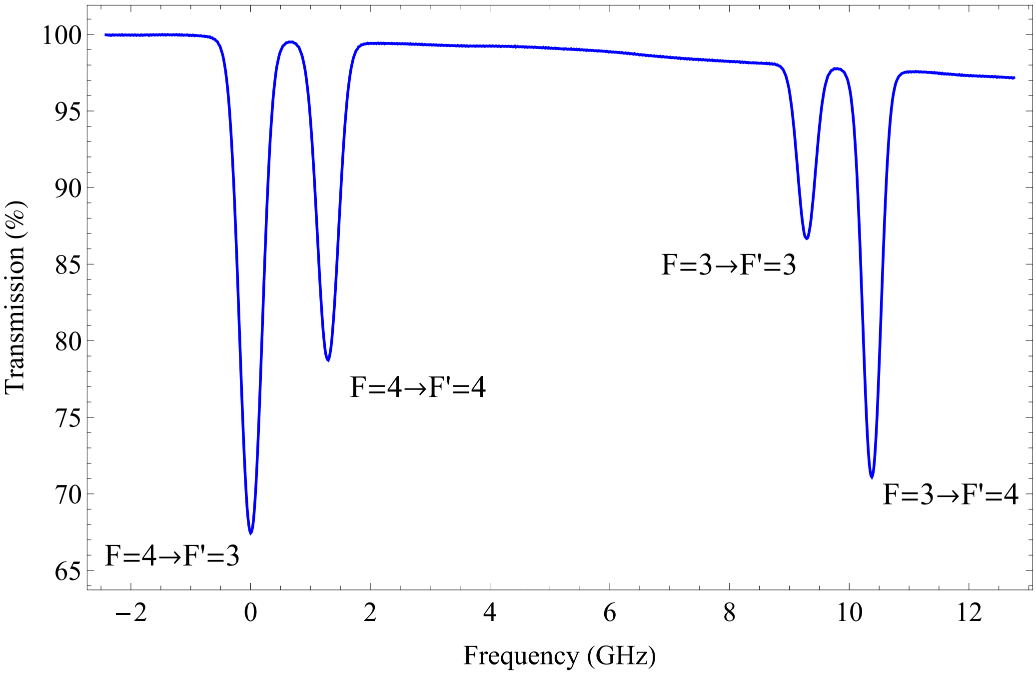

Figure 7.16: Absorption spectrum trace for the D_1 lines of Cs. Symbols next to features label the associated hyperfine transition. x-axis shows the detuning from the $F = 4 \rightarrow F' = 3$ (lowest energy) transition. y-axis shows the transmission from the photodiode.

Figure 7.16 shows the D_1 Doppler absorption spectrum for Cs. There are four identifiable features corresponding to the four hyperfine transitions between the $6S_{1/2}$ and $6P_{1/2}$ states, shown in Fig. 7.3. The transitions are separated by an amount which is greater than the width of the Doppler broadening, 200 MHz, so we do not need sub-Doppler spectroscopy to resolve the individual hyperfine transitions. This measurement was taken with a probe power of 1.5 mW.

With our cavity system it is possible to introduce a novel yet simple method of measuring the absorption spectrum that can be used to offer a precise measurement of Boltzmann's constant. Rather than measure the Doppler profile by scanning a laser we can instead offset lock from the laser using

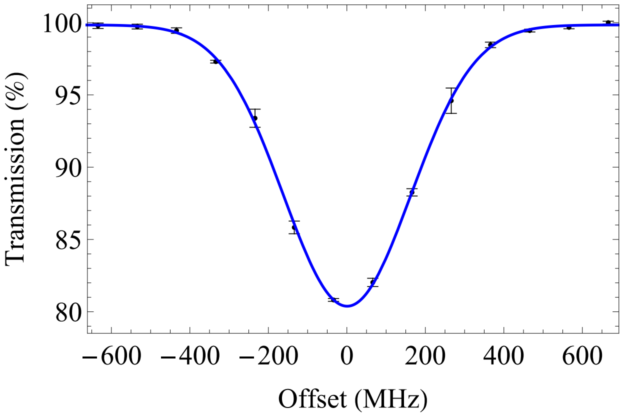

Figure 7.17: Data from offset locking measure of $F = 4 \rightarrow F' = 3$ transition of Cs. Data points show the transmission strength read when the laser is locked the offset frequency. 0 MHz is on resonance with the transition (not the EOM driving frequency). The blue curve shows a fitted Gaussian. The measurement was carried out with a power of 80 µW.

the cavity and measure the transmitted light through the cell. We can then vary the sideband frequency, re-lock the laser and repeat the measurement at regular offset intervals to scan across the profile. This has the added advantage of removing the time or piezo voltage calibration required for the frequency axis which is now provided directly by the frequency soure driving the EOM.

Figure 7.17 shows the data taken from this measurement. The black points show the data points which are measured in intervals of 100 MHz and a laser with a power of 80 µW. A Guassian with the equation:

$$\text{Signal}(f) = B + Ae^{-\frac{(f-f_0)^2}{\sigma^2}}, \tag{7.36}$$

is fitted to the data. In this equation A is the relative strength of the absorption, B is the background, f is the offset frequency, f_0 is the resonance frequency and σ is the standard deviation. Table 7.4 shows the best fit parameters.

It is well known that the lineshape of a transition where natural broadening is the dominant mechanism is Lorentzian [142]:

$$\Phi(\delta) = \frac{1}{2\pi}\frac{\Gamma}{\delta^2 + \frac{\Gamma^2}{4}}, \tag{7.37}$$

Parameter	Value
A	-1.176 (9) V
B	6.037(5) V
σ	162.0(1.6) MHz^{-1}
f_0	0.7(1.3) MHz

Table 7.4: Table showing the best fit parameters for the data in Fig. 7.17 in Eq. 7.36

where Γ is the natural linewidth and $\delta = 2\pi(f - f_0)$ is the detuning from resonance. In an ideal gas, the velocity distribution of atoms is given by the Maxwell-Boltzmann distribution:

$$f_D(v) = \frac{1}{\sqrt{\pi} v_p} e^{-\frac{v^2}{v_p^2}}, \tag{7.38}$$

where v_p is the speed at a given temperature T:

$$v_p = \sqrt{\frac{2Tk_\mathrm{B}}{m}}, \tag{7.39}$$

and k_B is the Boltzmann constant and m is the mass of the atom. When accounting for Doppler broadening the resulting lineshape of the transition must be the convolution of the natural broadened lineshape and the Doppler broadening:

$$\Phi_D(\delta) = \int f_D(v)\Phi(\delta - kv)dv, \tag{7.40}$$

where k is the wavevector of the incident light. In the limit where the Doppler broadening is much larger than the natural linewidth, the natural broadening can be approximated by a delta function, meaning:

$$\Phi_D(\delta) = \frac{1}{\sqrt{\pi} k v_p} e^{-\frac{\delta^2}{v_p^2}} = \sqrt{\frac{mc^2}{2\pi k_\mathrm{B} T f_0}} e^{-\frac{m(f-f_0)^2\lambda^2}{2k_\mathrm{B}T}}. \tag{7.41}$$

This is proportional to the Gaussian term we have fitted in Eq. 7.36. The standard deviation of the Gaussian must be:

$$\sigma = \sqrt{\frac{k_{\mathrm{B}} T}{m\lambda}}. \tag{7.42}$$

7.6.3 Boltzmann Constant Measurement

Given the fitted value of $\sigma = 162.0(1.6)$ MHz, the mass of the Cs atom to be $m = 2.21 \times 10^{-25}$ kg and assume an ambient room temperature of $T = 20$ °C we obtain an estimate of Boltzmann's constant of $k_{\mathrm{B}} = 1.58(3) \times 10^{-23}$ m^{2}kg s$^{-1}K^{-1}$. This is 14 % greater than the accepted value: $k_{\mathrm{B}} = 1.38 \times 10^{-23}$ m^{2}kg s$^{-1}K^{-1}$.

The difference may be to a few reasons. This was a very rudimentary setup. Most critically the cell was not temperature stabilised and was assumed to be at room temperature. The intensity of the laser was about 1/3 the value of the saturation intensity which may conflict with our delta function approximation in Eq. 7.40. Sensitivity to the Earth's magnetic fields and local fields in the laboratory as well as optical pumping effects in addition to further unknown effects may have contributed to this difference. However, this was never intended to be an accurate measurement for Boltzmann constant, rather a proposal to lay the ground work for such an accurate measurement. Previous optical techniques which utilise the Doppler broadening to determine the Boltzmann constant has successfully been performed on molecular species and a sample of the work can be found in references [143–145].

7.6.4 Two-Photon Spectroscopy

We now turn our attention to the excited state transition. We largely focused on an inverted ladder system, shown in Fig. 7.18, since we found the effects of a two-photon excitation are much more obvious when the probe laser is on the lower transition. A quantitative understanding of the theory in this subsection is beyond the scope of the thesis but can otherwise be found in references [146–149].

In an inverted ladder system one may naively expect an electromagnetically induced transparency (EIT) signal. When the wavelength of the probe laser is lower than the coupling wavelength the EIT is suppressed due to the Dop-

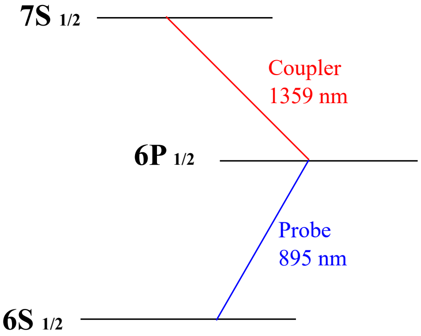

Figure 7.18: Inverted ladder system. The probe laser which will be used to acquire the data drives the $6S_{1/2} \rightarrow 6P_{1/2}$ transition and the coupling laser is locked on resonance with the $6P_{1/2} \rightarrow 7S_{1/2}$.

pler averaging [149]. Instead, we observe both absorptive and transparency features on the probe trace that arise as a result of the optical pumping of the atomic population between the various states of the system.

Figure 7.19 shows the measured absorption spectrum from the $F = 4$ ground state. A spectrum is measured for each case where the coupling laser is resonant with the excited state transition, giving us four possible transitions. The power for the coupling laser and probe laser are 2.6 mW and 70 µW respectively. In each trace, the second photon feature is obvious. Namely, in the all but the $F' = 4 \rightarrow F'' = 4$ transition we see a finer absorptive feature distort the Doppler broadened single photon signal. In the $F' = 3 \rightarrow F'' = 3$ transition there exists a transparency.

The effects of the relative intensities on the absorption spectrum are studied. There are eight possible combinations of transitions. In this subsection we will only give one exemplar transition as proof of concept our system performs two-photon excitation.

Figure 7.20 shows the measured traces for the transition $F = 4 \rightarrow F' = 3 \rightarrow F'' = 3$. Several traces are recorded for different coupling laser intensities and two different data sets have been taken for probe intensities of 5.3 mW/cm^2 and 110 mW/cm^2. Studying Fig. 7.20(b) we see that increasing the coupling intensity causes the transmission feature to become weaker and eventually transform into an absorptive feature.

In the low coupling intensity regime the transparency is owed to double resonance optical pumping (DROP) [148]. That is to say the double resonance

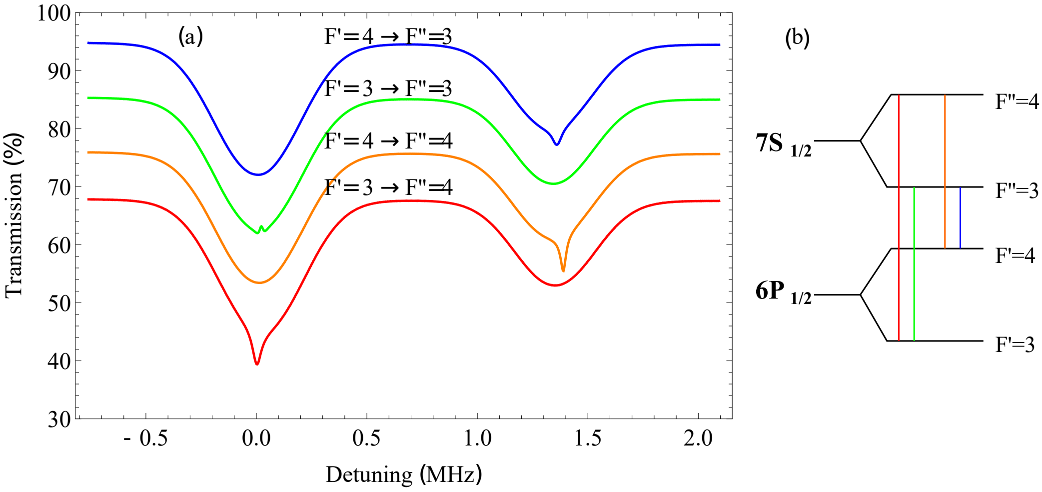

Figure 7.19: (a) Probe transmission in presence of coupling laser. The traces originate from ground state $F = 4$. Each trace corresponds to a different transition which is indicated next to the trace on the right. An artificial vertical shift is added to each trace to make them easier to distinguish. (b) Hyperfine diagram with transitions represented by coloured lines. Line colours correspond to the trace in (a). The grey lines represent the probe beam.

optically pumps the other $6S_{1/2}$ ground state which raises the saturation thereby inducing a slight transparency.

7.7 Summary

In this chapter a summary of Pound-Drever-Hall theory has been given. We have locked a pair of lasers to a cavity which will be used both for STIRAP to create rovibrational ground state KCs molecules and as part of a three photon excitation of Cs to Rydberg states. Further to this we have applied the locked lasers to characterise our cavity. At the end of the chapter we have provided a brief study on the spectroscopy of Cs. The spectroscopy study was useful in demonstrating the effectiveness of our setup for generating the first two photons needed for Rydberg excitation. We will later apply an additional laser at 779nm to provide the third photon needed to access Rydberg states.

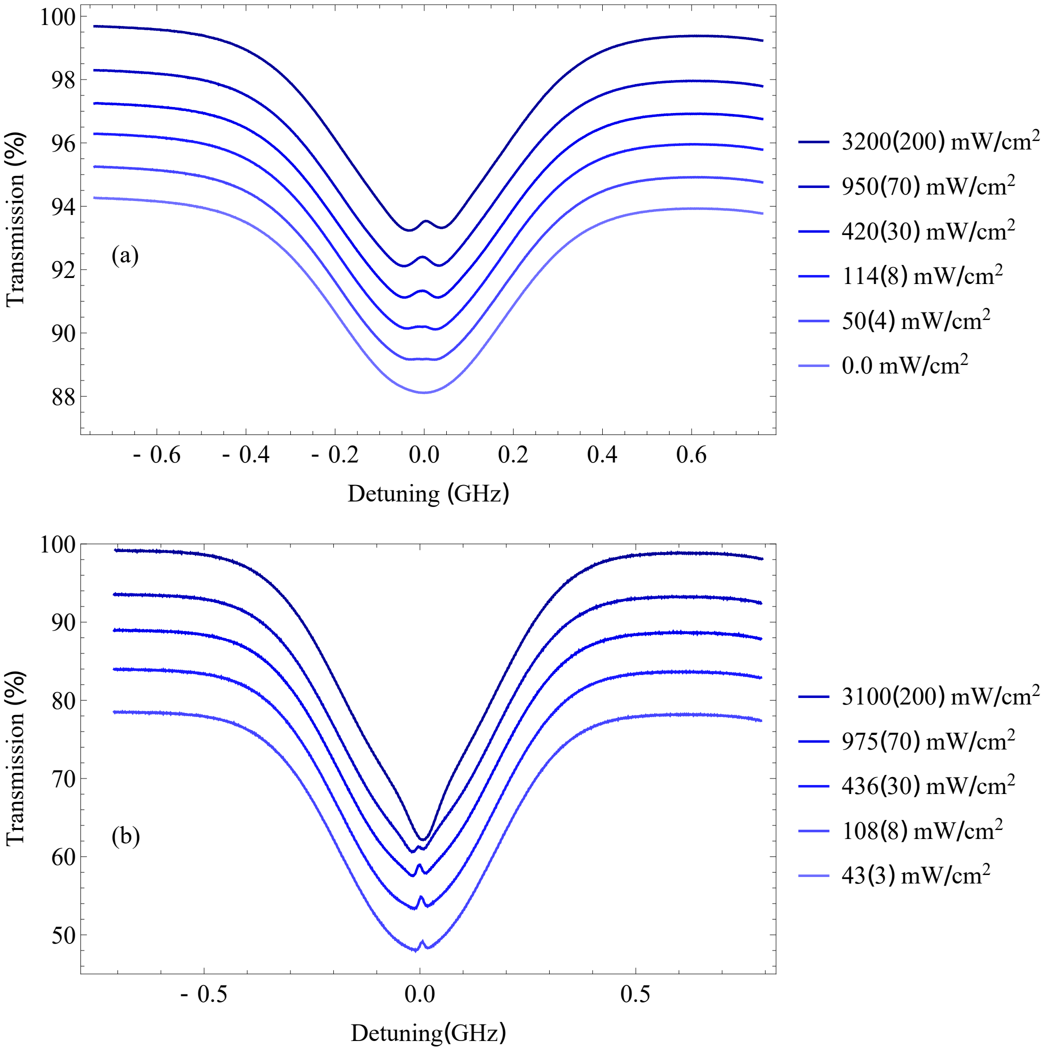

Figure 7.20: Two-photon spectroscopy on the $F = 4 \rightarrow F' = 3 \rightarrow F'' = 3$ transition. The coupling is locked on resonance. Each trace corresponds to a different coupling intensity. An artificial vertical offset has been added to each trace. (a) Probe laser at an intensity of 5.3 mW/cm^2 and (b) probe laser at an intensity of 110 mW/cm^2

Chapter 8

Conclusion and Outlook

8.1 Thesis Summary

This thesis has outlined the initial progress towards an apparatus for producing ground state RbCs and KCs molecules in an optical lattice.

In chapter 2 the theory behind interacting molecules in a lattice is summarised. We outlined the physics regarding the interactions between molecules in neighbouring lattice sites. These calculations were based on an XXZ model and from this we derived the conditions necessary on electric fields needed to tune the interactions whilst maintaining spin interactions across the sites.

Our newly constructed vacuum chamber is described in chapter 3. The vacuum chamber is split into four distinct parts. The Cs 2D-MOT, the Rb/K 2D-MOT, and the main chamber were described in detail and the science cell in summary.

Chapter 4 details spectroscopy experiments on the D_1 lines of K. We compare modulation transfer spectroscopy signals predicted from the theory with signals obtained from experiment. The calculations for the prediction were done by H.R Noh (Chonnam National University). We found that there existed good agreement between the theory and experiment for the lin $||$ lin and $\sigma^+\sigma^-$ polarisation configurations but comparatively poor agreement in the case of $\sigma^+\sigma^+$.

The optimisation of the initial stages of the K laser cooling process in our vacuum apparatus are outlined in chapter 5. We are able to obtain a sample of 10^8 ^{41}K atoms at a temperature of 42 µK.

Chapter 6 describes the operation of the MOTs for all species and results regarding a three species MOT are also shown. Chapter 7 summarises a new laser setup which can be used for both STIRAP of KCs and exciting Cs Rydberg atoms.

We have already performed some studies of Rb and Cs in the main chamber and these are expected to be covered in other theses. In particular we have used Kapitza-Dirac scattering to measure the tune-out wavelength of Cs [62] and we have also transported atomic samples of both Rb and Cs from the main chamber to the science cell using a moving standing wave, a technique similar to that described in [77].

Currently, we are nearly at the stage that we are able to image Cs atoms in a lattice. At the time of writing of this thesis we do not yet have a working mechanism for layer selection but when this installed we should be able to have sufficient resolution to image Cs in a lattice. In addition to loading ground state molecules into an optical lattice we anticipate that we will eventually be able to image the molecular behaviour with a high numerical objective.

8.2 Outlook

Having constructed the apparatus we discuss here what we hope to achieve with it. Ultimately there are two paths open to us at present which can be done in parallel: RbCs and KCs.

RbCs molecules have been studied extensively one of our older experiments and we are keen to extend these studies to optical lattices in a quantum gas microscope. A major obstacle to overcome will be to load Rb and Cs atoms into a lattice and associate them into a mixture. Although this has been done before [31], associating them and loading them efficiently into a lattice with a dense enough sample to be able to carry out quantum simulation experiments still remains open to debate. We are exploring the idea of a moving dimple trap [150]. At the science cell: Cs and Rb will captured in separate dimples in the superfluid state. The laser producing the Rb dimple will be reflected into the science cell from a mirror with a piezo actuator which will allow us to finely tune the position of the Rb sample. The optical lattice potential can be tuned to put Cs in the Mott insulator state with approximately one atom per site. The Rb dimple may then be moved so that the Rb superfluid overlaps with the Cs Mott insulator. Finally, the lattice potential can be tuned to put Rb in the Mott insulator state producing a sample with one Rb and one Cs atom per lattice site which can then be associated into molecules. Work has recently been carried out at Innsbruck in which a protocol has been developed with efficiently associating molecules in an optical lattice [151].

When molecules have been achieved we can perform quantum simulation studies with the lattice. As mentioned in chapter two we wish to recreate an environment which can be modelled by an XXZ Hamiltonian since this Hamiltonian shares many parallels with Hamiltonians which govern the behaviour of electrons in solid materials [59, 152]. Suitable quantum simulation experiments could involve observation of well understood phenomena such as the Hanbury Brown-Twiss effect in a lattice [56] or the varying the spin exchange coupling values with an electric field allowing us to study the effects on the spin correlation throughout and spin transport throughout the lattice [59, 153]. It should be noted that assigning pseudospins to the molecule's rotational states as a method of quantum simulation has proven quite challenging thus far. This is due to the anisotropic nature of the differential light shifts of the rotational states induced by the optical dipole trap. This causes the transition frequency between the two rotational states to shift throughout the trap. Work on our previous generation experiment seeks to overcome this issue by using a rotationally magic trap. That is, a trap whose wavelength is such that the polarizability of the two rotational states are the same, cancelling the resulting light shift [154, 155].

There is still much science to be discovered on the KCs side as well. At present Feshbach resonances between ^{39}K and ^{133}Cs have been characterised and further resonances predicted for the other stable isotopes of K [42, 112]. Suitable parameters for STIRAP to the rovibrational ground state have also been predicted [132]. In our experiment K and Cs can be cooled simultaneously but the K is still too hot to mix in a dipole trap with Cs and search for resonances. We hope to resolve this issue by way of a magnetic trap. We can mix our three species together and use Rb as a sympathetic coolant for both species in the trap. This would entail trapping all three species in a magnetic trap. Due to nature of the trappable states of K and Cs, it is not yet clear if this will succeed. Failing a magnetic trap other options are available such as DRSC and gray molasses for K. If KCs ground state molecules can be formed then we can perform the same experiments in our lattice as with RbCs. The advantages to KCs are the larger intrinsic dipole moment 1.92 D, as oppose to 1.26 D for RbCs, giving way to stronger interactions and the presence of a stable fermionic isotope, ^{40}K, which can allow us to study fermionic molecules in addition to bosonic molecules.

8.3 Concluding Remarks

This thesis has detailed the groundwork undertaken to establish what will hopefully become a leading in experiment in the field of ultracold molecules. With many other groups around the world working towards their own experiments this is an extremely fast paced field with research being produced at exciting yet frightening rate. We hope this experiment will ultimately allow us to realise many aspects of quantum simulation, something that has been long anticipated. Not only can we further probe the fundamentals of atom-atom and molecule-molecule interactions in cold and quantum gasses but hopefully the knowledge gained can produce benefits across other fields of physics such as condensed matter and fundamental physics.

Bibliography

[1] T. Hänsch and A. Schawlow, Optics Communications **13**, 68 (1975).

[2] P. D. Lett, R. N. Watts, C. I. Westbrook, W. D. Phillips, P. L. Gould, and H. J. Metcalf, Phys. Rev. Lett. **61**, 169 (1988).

[3] J. Dalibard and C. Cohen-Tannoudji, J. Opt. Soc. Am. B **6**, 2023 (1989).

[4] D. E. Pritchard, E. L. Raab, V. Bagnato, C. E. Wieman, and R. N. Watts, Phys. Rev. Lett. **57**, 310 (1986).

[5] A. L. Migdall, J. V. Prodan, W. D. Phillips, T. H. Bergeman, and H. J. Metcalf, Phys. Rev. Lett. **54**, 2596 (1985).

[6] S. Chu, J. E. Bjorkholm, A. Ashkin, and A. Cable, Phys. Rev. Lett. **57**, 314 (1986).

[7] M. H. Anderson, J. R. Ensher, M. R. Matthews, C. E. Wieman, and E. A. Cornell, Science **269**, 198 (1995).

[8] K. B. Davis, M. O. Mewes, M. R. Andrews, N. J. van Druten, D. S. Durfee, D. M. Kurn, and W. Ketterle, Phys. Rev. Lett. **75**, 3969 (1995).

[9] B. DeMarco and D. S. Jin, Science **285**, 1703 (1999).

[10] J. F. Sherson, C. Weitenberg, M. Endres, M. Cheneau, I. Bloch, and S. Kuhr, Nature **467**, 68 (2010).

[11] D. Jaksch, C. Bruder, J. I. Cirac, C. W. Gardiner, and P. Zoller, Phys. Rev. Lett. **81**, 3108 (1998).

[12] M. Greiner, O. Mandel, T. Esslinger, T. W. Hänsch, and I. Bloch, Nature **415**, 39 (2002).

[13] W. S. Bakr, J. I. Gillen, A. Peng, S. Fölling, and M. Greiner, Nature **462**, 74 (2009).

[14] K.-K. Ni, S. Ospelkaus, M. H. G. de Miranda, A. Pe'er, B. Neyenhuis, J. J. Zirbel, S. Kotochigova, P. S. Julienne, D. S. Jin, and J. Ye, Science **322**, 231 (2008).

[15] I. Bloch, J. Dalibard, and S. Nascimbène, Nature Physics **8**, 267 (2012).

[16] S. Kuhr, National Science Review **3**, 170 (2016).

[17] A. V. Gorshkov, S. R. Manmana, G. Chen, E. Demler, M. D. Lukin, and A. M. Rey, Phys. Rev. A **84**, 033619 (2011).

[18] T. Esslinger, Annual Review of Condensed Matter Physics **1**, 129 (2010).

[19] L. Tarruell and L. Sanchez-Palencia, Comptes Rendus Physique **19**, 365 (2018), quantum simulation / Simulation quantique.

[20] K. I. Petsas, A. B. Coates, and G. Grynberg, Phys. Rev. A **50**, 5173 (1994).

[21] J. Stuhler, A. Griesmaier, T. Koch, M. Fattori, T. Pfau, S. Giovanazzi, P. Pedri, and L. Santos, Phys. Rev. Lett. **95**, 150406 (2005).

[22] T. Lahaye, T. Koch, B. Fröhlich, M. Fattori, J. Metz, A. Griesmaier, S. Giovanazzi, and T. Pfau, Nature **448**, 672 (2007).

[23] M. Lu, N. Q. Burdick, S. H. Youn, and B. L. Lev, Phys. Rev. Lett. **107**, 190401 (2011).

[24] M. Sohmen, M. J. Mark, M. Greiner, and F. Ferlaino, arXiv preprint arXiv:2306.05404 (2023).

[25] H. Weimer, M. Müller, I. Lesanovsky, P. Zoller, and H. P. Büchler, Nature Physics **6**, 382 (2010).

[26] M. P. Koppinger, *Creation of ultracold RbCs molecule*, Ph.D. thesis, Durham University (2014).

[27] V. Zhelyazkova, A. Cournol, T. E. Wall, A. Matsushima, J. J. Hudson, E. A. Hinds, M. R. Tarbutt, and B. E. Sauer, Phys. Rev. A **89**, 053416 (2014).

[28] E. Shuman, J. Barry, and D. DeMille, Nature **467**, 820 (2010).

[29] S. Ding, Y. Wu, I. A. Finneran, J. J. Burau, and J. Ye, Phys. Rev. X **10**, 021049 (2020).

[30] K. Pilch, A. D. Lange, A. Prantner, G. Kerner, F. Ferlaino, H.-C. Nägerl, and R. Grimm, Phys. Rev. A **79**, 042718 (2009).

[31] T. Takekoshi, L. Reichsöllner, A. Schindewolf, J. M. Hutson, C. R. Le Sueur, O. Dulieu, F. Ferlaino, R. Grimm, and H.-C. Nägerl, Phys. Rev. Lett. **113**, 205301 (2014).

[32] P. K. Molony, P. D. Gregory, Z. Ji, B. Lu, M. P. Köppinger, C. R. Le Sueur, C. L. Blackley, J. M. Hutson, and S. L. Cornish, Phys. Rev. Lett. **113**, 255301 (2014).

[33] W. B. Cairncross, J. T. Zhang, L. R. B. Picard, Y. Yu, K. Wang, and K.-K. Ni, Phys. Rev. Lett. **126**, 123402 (2021).

[34] M. Guo, B. Zhu, B. Lu, X. Ye, F. Wang, R. Vexiau, N. Bouloufa-Maafa, G. Quéméner, O. Dulieu, and D. Wang, Phys. Rev. Lett. **116**, 205303 (2016).

[35] J. W. Park, S. A. Will, and M. W. Zwierlein, Phys. Rev. Lett. **114**, 205302 (2015).

[36] J. Deiglmayr, A. Grochola, M. Repp, K. Mörtlbauer, C. Glück, J. Lange, O. Dulieu, R. Wester, and M. Weidemüller, Phys. Rev. Lett. **101**, 133004 (2008).

[37] P. D. Gregory, J. Aldegunde, J. M. Hutson, and S. L. Cornish, Phys. Rev. A **94**, 041403 (2016).

[38] A. D. Lercher, T. Takekoshi, M. Debatin, B. Schuster, R. Rameshan, F. Ferlaino, R. Grimm, and H.-C. Nägerl, The European Physical Journal D **65**, 3 (2011).

[39] T. Takekoshi, M. Debatin, R. Rameshan, F. Ferlaino, R. Grimm, H.-C. Nägerl, C. R. Le Sueur, J. M. Hutson, P. S. Julienne, S. Kotochigova, and E. Tiemann, Phys. Rev. A **85**, 032506 (2012).

[40] M. Aymar and O. Dulieu, The Journal of Chemical Physics **122**, 204302 (2005).

[41] J. Deiglmayr, M. Aymar, R. Wester, M. Weidemüller, and O. Dulieu, The Journal of Chemical Physics **129**, 064309 (2008).

[42] H. J. Patel, C. L. Blackley, S. L. Cornish, and J. M. Hutson, Phys. Rev. A **90**, 032716 (2014).

[43] R. Grimm, M. Weidemüller, and Y. B. Ovchinnikov (Academic Press, 2000) pp. 95–170.

[44] I. Bloch, Nature Physics **1**, 23 (2005).

[45] V. A. Kashurnikov, N. V. Prokof'ev, and B. V. Svistunov, Phys. Rev. A **66**, 031601 (2002).

[46] W. S. Bakr, A. Peng, M. E. Tai, R. Ma, J. Simon, J. I. Gillen, S. Fölling, L. Pollet, and M. Greiner, Science **329**, 547 (2010).

[47] I. Bloch and M. Greiner, Nature Reviews Physics **4**, 739 (2022).

[48] M. Miranda, R. Inoue, Y. Okuyama, A. Nakamoto, and M. Kozuma, Phys. Rev. A **91**, 063414 (2015).

[49] R. Yamamoto, J. Kobayashi, T. Kuno, K. Kato, and Y. Takahashi, New Journal of Physics **18**, 023016 (2016).

[50] M. F. Parsons, F. Huber, A. Mazurenko, C. S. Chiu, W. Setiawan, K. Wooley-Brown, S. Blatt, and M. Greiner, Phys. Rev. Lett. **114**, 213002 (2015).

[51] A. Omran, M. Boll, T. A. Hilker, K. Kleinlein, G. Salomon, I. Bloch, and C. Gross, Phys. Rev. Lett. **115**, 263001 (2015).

[52] K. Kwon, K. Kim, J. Hur, S. Huh, and J.-y. Choi, Phys. Rev. A **105**, 033323 (2022).

[53] E. Haller, J. Hudson, A. Kelly, D. A. Cotta, B. Peaudecerf, G. D. Bruce, and S. Kuhr, Nature Physics **11**, 738 (2015).

[54] L. W. Cheuk, M. A. Nichols, M. Okan, T. Gersdorf, V. V. Ramasesh, W. S. Bakr, T. Lompe, and M. W. Zwierlein, Phys. Rev. Lett. **114**, 193001 (2015).

[55] A. Impertro, J. F. Wienand, S. Häfele, H. von Raven, S. Hubele, T. Klostermann, C. R. Cabrera, I. Bloch, and M. Aidelsburger, "An unsupervised deep learning algorithm for single-site reconstruction in quantum gas microscopes," (2022).

[56] J. S. Rosenberg, L. Christakis, E. Guardado-Sanchez, Z. Z. Yan, and W. S. Bakr, Nature Physics **18**, 1062 (2022).

[57] T. Volz, N. Syassen, D. M. Bauer, E. Hansis, S. Dürr, and G. Rempe, Nature Physics **2**, 692 (2006).

[58] J. G. Danzl, M. J. Mark, E. Haller, M. Gustavsson, R. Hart, J. Aldegunde, J. M. Hutson, and H.-C. Nägerl, Nature Physics (2010).

[59] J. P. Covey, L. D. Marco, Ó. L. Acevedo, A. M. Rey, and J. Ye, New Journal of Physics **20**, 043031 (2018).

[60] A. D. Innes, P. Majumder, H. R. Noh, and S. L. Cornish, arXiv preprint arXiv:2310.11327 (2023).

[61] A. J. Matthies, J. M. Mortlock, L. A. McArd, A. P. Raghuram, A. D. Innes, P. D. Gregory, S. L. Bromley, and S. L. Cornish, arXiv preprint arXiv:2307.13382 (2023).

[62] A. Ratkata, P. D. Gregory, A. D. Innes, A. J. Matthies, L. A. McArd, J. M. Mortlock, M. S. Safronova, S. L. Bromley, and S. L. Cornish, Phys. Rev. A **104**, 052813 (2021).

[63] H. Fahs, A. R. Allouche, M. Korek, and M. Aubert-Frécon, Journal of Physics B: Atomic, Molecular and Optical Physics **35**, 1501 (2002).

[64] J. A. Blackmore, L. Caldwell, P. D. Gregory, E. M. Bridge, R. Sawant, J. Aldegunde, J. Mur-Petit, D. Jaksch, J. M. Hutson, B. E. Sauer, M. R. Tarbutt, and S. L. Cornish, Quantum Science and Technology **4**, 014010 (2018).

[65] B. Bransden, C. Joachain, and T. Plivier, *Physics of Atoms and Molecules*, Pearson Education (Prentice Hall, 2003).

[66] M. L. Wall, K. R. A. Hazzard, and A. M. Rey, "Quantum magnetism with ultracold molecules," in *From Atomic to Mesoscale*, Chap. Chapter 1, pp. 3–37.

[67] A. V. Gorshkov, S. R. Manmana, G. Chen, J. Ye, E. Demler, M. D. Lukin, and A. M. Rey, Phys. Rev. Lett. **107**, 115301 (2011).

[68] M. W. Gempel, T. Hartmann, T. A. Schulze, K. K. Voges, A. Zenesini, and S. Ospelkaus, New Journal of Physics **18**, 045017 (2016).

[69] S. A. Moses, *A quantum gas of polar molecules in an optical lattice*, Ph.D. thesis, University of Colorado, Boulder (2016).

[70] J. P. Covey, *Enhanced optical and electric manipulation of a quantum gas of KRb molecules*, Ph.D. thesis, University of Colorado (2017).

[71] P. J. Dagdigian and L. Wharton, The Journal of Chemical Physics **57**, 1487 (1972).

[72] S. A. Will, J. W. Park, Z. Z. Yan, H. Loh, and M. W. Zwierlein, Phys. Rev. Lett. **116**, 225306 (2016).

[73] M. Guo, X. Ye, J. He, G. Quéméner, and D. Wang, Phys. Rev. A **97**, 020501 (2018).

[74] K.-K. Ni, *A Quantum Gas of Polar Molecules*, Ph.D. thesis, University of Colorado (2010).

[75] S. Ospelkaus, K.-K. Ni, G. Quéméner, B. Neyenhuis, D. Wang, M. H. G. de Miranda, J. L. Bohn, J. Ye, and D. S. Jin, Phys. Rev. Lett. **104**, 030402 (2010).

[76] G. Unnikrishnan, *Cooling, Transport and Mixing of Ultracold K and Cs*, Ph.D. thesis, University of Innsbruck (2022).

[77] S. Schmid, G. Thalhammer, K. Winkler, F. Lang, and J. H. Denschlag, New Journal of Physics **8**, 159 (2006).

[78] S. Händel, *Experiments on ultracold quantum gases of ^{85}Rb and ^{87}Rb*, Ph.D. thesis, Durham University (2011).

[79] M. Gröbner, P. Weinmann, E. Kirilov, H.-C. Nägerl, P. S. Julienne, C. R. Le Sueur, and J. M. Hutson, Phys. Rev. A **95**, 022715 (2017).

[80] A. Burchianti, C. D'Errico, S. Rosi, A. Simoni, M. Modugno, C. Fort, and F. Minardi, Phys. Rev. A **98**, 063616 (2018).

[81] D. Schrader, S. Kuhr, W. Alt, M. Müller, V. Gomer, and D. Meschede, Applied Physics B **73**, 819 (2001).

[82] S. Haroche and F. Hartmann, Phys. Rev. A **6**, 1280 (1972).

[83] D. W. Preston, American Journal of Physics **64**, 1432 (1996).

[84] G. D. Rovera, G. Santarelli, and A. Clairon, Review of Scientific Instruments **65**, 1502 (1994).

[85] G. C. Bjorklund, Opt. Lett. **5**, 15 (1980).

[86] J. Mandon, G. Guelachvili, and N. Picqué, Opt. Lett. **32**, 2206 (2007).

[87] K. L. Corwin, Z.-T. Lu, C. F. Hand, R. J. Epstein, and C. E. Wieman, Appl. Opt. **37**, 3295 (1998).

[88] A. Millett-Sikking, I. G. Hughes, P. Tierney, and S. L. Cornish, Journal of Physics B: Atomic, Molecular and Optical Physics **40**, 187 (2006).

[89] D. J. McCarron, I. G. Hughes, P. Tierney, and S. L. Cornish, Review of Scientific Instruments **78**, 093106 (2007).

[90] M. L. Harris, S. L. Cornish, A. Tripathi, and I. G. Hughes, Journal of Physics B: Atomic, Molecular and Optical Physics **41**, 085401 (2008).

[91] A. L. Marchant, S. Händel, T. P. Wiles, S. A. Hopkins, C. S. Adams, and S. L. Cornish, Opt. Lett. **36**, 64 (2011).

[92] W. Quan, Y. Li, R. Li, H. Shang, Z. Fang, J. Qin, and S. Wan, Appl. Opt. **55**, 2503 (2016).

[93] C. Wieman and T. W. Hänsch, Phys. Rev. Lett. **36**, 1170 (1976).

[94] Y. Torii, H. Tashiro, N. Ohtsubo, and T. Aoki, Phys. Rev. A **86**, 033805 (2012).

[95] Y. Yoshikawa, T. Umeki, T. Mukae, Y. Torii, and T. Kuga, Appl. Opt. **42**, 6645 (2003).

[96] J. H. Shirley, Opt. Lett. **7**, 537 (1982).

[97] D. J. McCarron, S. A. King, and S. L. Cornish, Measurement Science and Technology **19**, 105601 (2008).

[98] L. Mudarikwa, K. Pahwa, and J. Goldwin, Journal of Physics B: Atomic, Molecular and Optical Physics **45**, 065002 (2012).

[99] H.-R. Noh, S. E. Park, L. Z. Li, J.-D. Park, and C.-H. Cho, Opt. Express **19**, 23444 (2011).

[100] L. Zhe Li, S. Eon Park, H.-R. Noh, J.-D. Park, and C.-H. Cho, Journal of the Physical Society of Japan **80**, 074301 (2011).

[101] T. Preuschoff, M. Schlosser, and G. Birkl, Opt. Express **26**, 24010 (2018).

[102] N. Ito, Review of Scientific Instruments **71**, 2655 (2000).

[103] B. Cheng, Z.-Y. Wang, B. Wu, A.-P. Xu, Q.-Y. Wang, Y.-F. Xu, and Q. Lin, Chinese Physics B **23**, 104222 (2014).

[104] D. Sun, C. Zhou, L. Zhou, J. Wang, and M. Zhan, Opt. Express **24**, 10649 (2016).

[105] J.-B. Long, S.-J. Yang, S. Chen, and J.-W. Pan, Opt. Express **26**, 27773 (2018).

[106] C.-F. Wu, X.-S. Yan, L.-X. Wei, P. Ma, J.-H. Tu, J.-W. Zhang, and L.-J. Wang, Chinese Physics B **27**, 114203 (2018).

[107] V. Negnevitsky and L. D. Turner, Opt. Express **21**, 3103 (2013).

[108] M. Mihm, K. Lampmann, A. Wenzlawski, and P. Windpassinger, Review of Scientific Instruments **89**, 096101 (2018).

[109] M. Landini, S. Roy, L. Carcagní, D. Trypogeorgos, M. Fattori, M. Inguscio, and G. Modugno, Phys. Rev. A **84**, 043432 (2011).

[110] H.-Z. Chen, X.-C. Yao, Y.-P. Wu, X.-P. Liu, X.-Q. Wang, Y.-X. Wang, Y.-A. Chen, and J.-W. Pan, Phys. Rev. A **94**, 033408 (2016).

[111] G. Salomon, L. Fouché, P. Wang, A. Aspect, P. Bouyer, and T. Bourdel, Euro. Phys. Lett **104**, 63002 (2013).

[112] M. Gröbner, P. Weinmann, E. Kirilov, and H.-C. Nägerl, Phys. Rev. A **95**, 033412 (2017).

[113] B. Wu, Y. Zhou, K. Weng, D. Zhu, Z. Fu, B. Cheng, X. Wang, and Q. Lin, J. Opt. Soc. Am. B **35**, 2705 (2018).

[114] T. G. Tiecke, *Feshbach resonances in ultracold mixtures of the fermionic quantum gases* ^{6}*Li and* ^{40}*K*, Ph.D. thesis, University of Amsterdam (2009).

[115] R. K. Raj, D. Bloch, J. J. Snyder, G. Camy, and M. Ducloy, Phys. Rev. Lett. **44**, 1251 (1980).

[116] S. E. Park and H.-R. Noh, Opt. Express **21**, 14066 (2013).

[117] S. Lee, J. Kang, S. Kim, J. Jeong, G. Moon, and H.-R. Noh, Opt. Express **29**, 34770 (2021).

[118] Fort, C., Bambini, A., Cacciapuoti, L., Cataliotti, F. S., Prevedelli, M., Tino, G. M., and Inguscio, M., Eur. Phys. J. D **3**, 113 (1998).

[119] T. Tiecke, "Properties of potassium," (2019).

[120] M. Landini, *A tunable Bose-Einstein condensat for quantum interferometry*, Ph.D. thesis, University of Trento (2012).

[121] R. S. Williamson-III, *Magneto-optical trapping of potassium isotopes*, Ph.D. thesis, University of Wisconsin, Madison (1997).

[122] K. Lindquist, M. Stephens, and C. Wieman, Phys. Rev. A **46**, 4082 (1992).

[123] D. A. Smith, S. Aigner, S. Hofferberth, M. Gring, M. Andersson, S. Wildermuth, P. Krüger, S. Schneider, T. Schumm, and J. Schmiedmayer, Opt. Express **19**, 8471 (2011).

[124] M. Taglieber, A.-C. Voigt, F. Henkel, S. Fray, T. W. Hänsch, and K. Dieckmann, Phys. Rev. A **73**, 011402 (2006).

[125] J. Arlt, P. Bance, S. Hopkins, J. Martin, S. Webster, A. Wilson, K. Zetie, and C. J. Foot, Journal of Physics B: Atomic, Molecular and Optical Physics **31**, L321 (1998).

[126] U. Gaubatz, P. Rudecki, M. Becker, S. Schiemann, M. Külz, and K. Bergmann, Chemical Physics Letters **149**, 463 (1988).

[127] J. R. Kuklinski, U. Gaubatz, F. T. Hioe, and K. Bergmann, Phys. Rev. A **40**, 6741 (1989).

[128] U. Gaubatz, P. Rudecki, S. Schiemann, and K. Bergmann, The Journal of Chemical Physics **92**, 5363 (1990).

[129] P. K. Molony, P. D. Gregory, Z. Ji, B. Lu, M. P. Köppinger, C. R. Le Sueur, C. L. Blackley, J. M. Hutson, and S. L. Cornish, Phys. Rev. Lett. **113**, 255301 (2014).

[130] B. Shore, *The Theory of Coherent Atomic Excitation* (Wiley, 1990).

[131] B. Shore, *Manipulating Quantum Structures Using Laser Pulses* (Cambridge University, 2011).

[132] D. Borsalino, R. Vexiau, M. Aymar, E. Luc-Koenig, O. Dulieu, and N. Bouloufa-Maafa, Journal of Physics B: Atomic, Molecular and Optical Physics **49**, 055301 (2016).

[133] L. P. Yatsenko, V. I. Romanenko, B. W. Shore, and K. Bergmann, Phys. Rev. A **65**, 043409 (2002).

[134] K. Aikawa, D. Akamatsu, J. Kobayashi, M. Ueda, T. Kishimoto, and S. Inouye, New Journal of Physics **11**, 055035 (2009).

[135] T. F. Gallagher, Reports on Progress in Physics **51**, 143 (1988).

[136] S. de Léséleuc, D. Barredo, V. Lienhard, A. Browaeys, and T. Lahaye, Phys. Rev. A **97**, 053803 (2018).

[137] E. Kuznetsova, S. T. Rittenhouse, H. R. Sadeghpour, and S. F. Yelin, Phys. Chem. Chem. Phys. **13**, 17115 (2011).

[138] A. Guttridge, D. K. Ruttley, A. C. Baldock, R. González-Férez, H. R. Sadeghpour, C. S. Adams, and S. L. Cornish, Phys. Rev. Lett. **131**, 013401 (2023).

[139] G. Brooker, *Modern Classical Optics (Oxford Master Series in Atomic, Optical and Laser Physics)* (Oxford University Press, USA, 2003).

[140] E. D. Black, American Journal of Physics **69**, 79 (2001).

[141] P. K. Molony, *Creation of ultracold polar ground-state RbCs molecules*, Ph.D. thesis, Durham University (2016).

[142] C. Foot, *Atomic Physics* (Oxford University Press, 2004).

[143] C. Daussy, M. Guinet, A. Amy-Klein, K. Djerroud, Y. Hermier, S. Briaudeau, C. J. Bordé, and C. Chardonnet, Phys. Rev. Lett. **98**, 250801 (2007).

[144] G. Casa, A. Castrillo, G. Galzerano, R. Wehr, A. Merlone, D. Di Serafino, P. Laporta, and L. Gianfrani, Phys. Rev. Lett. **100**, 200801 (2008).

[145] K. M. T. Yamada, A. Onae, F. L. Hong, H. Inaba, H. Matsumoto, Y. Nakajima, F. Ito, and T. Shimizu, Journal of Molecular Spectroscopy **249**, 95 (2008).

[146] D. A. Smith and I. G. Hughes, American Journal of Physics **72**, 631 (2004).

[147] B. E. Sherlock and I. G. Hughes, American Journal of Physics **77**, 111 (2009).

[148] H. S. Moon, W. K. Lee, L. Lee, and J. B. Kim, Applied Physics Letters **85**, 3965 (2004).

[149] C. Carr, *Cooperative Non-Equilibrium Dynamics in a Thermal Rydberg Ensemble*, Ph.D. thesis (2013).

[150] L. Reichsöllner, A. Schindewolf, T. Takekoshi, R. Grimm, and H.-C. Nägerl, Phys. Rev. Lett. **118**, 073201 (2017).

[151] A. Das, P. D. Gregory, T. Takekoshi, L. Fernley, M. Landini, J. M. Hutson, S. L. Cornish, and H.-C. Nägerl, arXiv preprint arXiv:2303.16144 (2023).

[152] F. Schäfer, T. Fukuhara, S. Sugawa, Y. Takasu, and Y. Takahashi, Nature Reviews Physics **2**, 411 (2020).

[153] L. Christakis, J. S. Rosenberg, R. Raj, S. Chi, A. Morningstar, D. A. Huse, Z. Z. Yan, and W. S. Bakr, Nature **614**, 64 (2023).

[154] P. D. Gregory, L. M. Fernley, A. L. Tao, S. L. Bromely, J. Stepp, Z. Zhang, S. Kotochigova, K. R. A. Hazzard, and S. L. Cornish, arXiv preprint arXiv:2306.02991 (2023).

[155] S. S. Kondov, C.-H. Lee, K. H. Leung, C. Liedl, I. Majewska, R. Moszynski, and T. Zelevinsky, Nature Physics **15**, 1118 (2019).